



PRECISE SAR MEASUREMENTS IN THE NEAR-FIELD  
OF RF ANTENNA SYSTEMS

by

Bandar M. Hakim

Dissertation submitted to the Faculty of the Graduate School of the  
University of Maryland, College Park in partial fulfillment  
of the requirements for the degree of  
Doctor of Philosophy  
2006

Advisory Committee:

Professor Christopher C. Davis, Chair  
Doctor Brian B. Beard  
Professor Kawthar Zaki  
Professor Issak Mayergoyz  
Professor Robert W. Gammon

©Copyright by  
Bandar M. Hakim  
2006

## Dedication

To the Love of My Life My Wife, and My sweet daughter.

To my Mother, Father, and three Sisters. And to rest of my Family.

## Acknowledgments

I owe my gratitude to all the people who have made this thesis possible and because of whom my graduate experience has been one that I will cherish forever.

I owe a great debt of gratitude to my advisor, Professor Christopher C. Davis. I would like to thank him for his help, support, and guidance throughout the research. I'd like to thank him for giving me an invaluable opportunity to work on challenging and extremely interesting projects.

I am also grateful to my mentor, Doctor Brian B. Beard at the Food and Drug Administration, Center for Devices and Radiological Health. I would like to thank him for his help, encouragement and advice.

Thanks go to the rest of my Ph.D. committee, Professor Issak Mayergoyz, Professor Kawthar Zaki, and Professor Robert W. Gammon for their invaluable time reviewing the thesis.

I would like to acknowledge the help and support of Doctor Howard I. Bassen, at the Food and Drug Administration, Center for Devices and Radiological Health, Professor Quirino Balzano, at the department of Electrical and Computer Engineering and Professor Jian-Guo Liu, at the department of Mathematics.

I would also like to thank Mr. Bruce R. Fleharty and Mr. Randolph L. Bidinger at the Food and Drug Administration, Center for Devices and Radiological Health, for their help in building some of the components used in this research.

I'm forever grateful to my family - my wife, mother, father, and sisters for their ongoing support and guidance.

# Contents

Dedication . . . . .	ii
Acknowledgments . . . . .	iii
<b>List of Tables</b>	<b>vii</b>
<b>List of Figures</b>	<b>ix</b>
<b>List of Abbreviations</b>	<b>x</b>
<b>List of Symbols</b>	<b>xi</b>
<b>1 Introduction</b>	<b>1</b>
1.1 Synopsis . . . . .	2
1.2 Brief Overview of Thesis . . . . .	3
<b>2 Background Information</b>	<b>4</b>
2.1 Tissue Heating and Regulations . . . . .	5
2.2 RF Dosimetry . . . . .	6
2.2.1 E-Field Probes . . . . .	7
2.2.2 Tissue-Equivalent Liquids . . . . .	9
2.3 FDTD Simulation . . . . .	11
<b>3 Experimental Design and Approach</b>	<b>16</b>
3.1 Experimental Setup . . . . .	19
3.2 Calibration Procedure . . . . .	21
3.2.1 Power Reflectance . . . . .	22
3.2.2 Fundamental Mode . . . . .	23
3.2.3 Boundary Effects . . . . .	24
3.2.4 Uncertainty Analysis . . . . .	25
<b>4 Calibration Measurements</b>	<b>29</b>
4.1 Dielectric Property Measurements . . . . .	29
4.1.1 Attenuation factor . . . . .	30
4.1.2 Power Reflectance . . . . .	31
4.2 Calibration Factor Measurements . . . . .	32
4.3 Net Power Measurements . . . . .	33
4.4 Calibration Procedure Overview . . . . .	33
<b>5 Results and Analysis</b>	<b>35</b>

5.1	Validation . . . . .	35
5.2	Results . . . . .	36
5.2.1	Dielectric Properties Measurement . . . . .	36
5.2.2	Calibration Factors Measurement . . . . .	37
5.3	Uncertainty Analysis . . . . .	38
5.3.1	Dielectric Properties Uncertainties . . . . .	39
5.3.2	Calibration Factors Uncertainties . . . . .	41
<b>6</b>	<b>Cell Phone Compliance Testing using SAM Phantom</b>	<b>51</b>
6.1	Introduction . . . . .	51
6.2	Test Procedure . . . . .	52
6.3	Results . . . . .	55
<b>7</b>	<b>Conclusion</b>	<b>58</b>
7.1	Chapter Highlights . . . . .	58
7.2	Summary . . . . .	59
<b>A</b>	<b>Components and Setup</b>	<b>60</b>
<b>B</b>	<b>Waveguide Fundamental Mode Equation in Lossy Media</b>	<b>68</b>
<b>C</b>	<b>Waveguide Power Reflectance</b>	<b>71</b>
<b>D</b>	<b>CalPer: LabVIEW Program</b>	<b>74</b>
D.1	Initilize/Home scanner . . . . .	74
D.2	Read Iso-Scan File . . . . .	74
D.3	Read Z-Scan File . . . . .	75
D.4	Calibrate Probe Holder . . . . .	75
D.5	Waveguide Iso Scan . . . . .	76
D.6	Manual Move . . . . .	77
D.7	Find Bottom . . . . .	78
D.8	Waveguide Z Scan . . . . .	78
<b>E</b>	<b>Program Listing</b>	<b>82</b>
E.1	wgz.m . . . . .	82
E.2	wgiso.m . . . . .	87
E.3	vcorrect.m . . . . .	93
E.4	pcorrect.m . . . . .	93
E.5	eprobe.m . . . . .	95
E.6	etheory.m . . . . .	96
E.7	factors.m . . . . .	97
E.8	gn.m . . . . .	98
E.9	funz.m . . . . .	99
E.10	funesr.m . . . . .	100
E.11	funesi.m . . . . .	101
E.12	reflect.m . . . . .	102
E.13	alpha.m . . . . .	105
E.14	stdee.m . . . . .	106
E.15	changeee.m . . . . .	107

E.16 calunc.m . . . . .	109
E.17 ref.m . . . . .	111
E.18 volsamfun.m . . . . .	114
E.19 calstd.m . . . . .	119
E.20 calunc.m . . . . .	121
E.21 calibrate.m . . . . .	123
E.22 calse.m . . . . .	124
E.23 Measured Coupler Loss . . . . .	126
E.24 Measured Cable Loss . . . . .	126

<b>Bibliography</b>	<b>128</b>
---------------------	------------

# List of Tables

2.1	SAR test standards for Occupational exposure . . . . .	6
2.2	SAR test standards for General Public exposure . . . . .	6
2.3	Target dielectric values for tissue-equivalent liquids at specific frequencies . . . . .	10
2.4	Typical tissue-equivalent recipes given in weight percentages . . . . .	11
3.1	Uncertainty as a Function of Confidence Level for Normally Distributed Errors	25
5.1	Waveguide specifications at 900MHz and 1800MHz . . . . .	35
5.2	Saline Dielectric Properties measured at 900MHz . . . . .	36
5.3	Saline Dielectric Properties measured at 1800MHz . . . . .	36
5.4	Tissue-Equivalent Liquid Dielectric Properties measured at 900MHz . . . . .	37
5.5	Tissue-Equivalent Liquid Dielectric Properties measured at 1800MHz . . . . .	37
5.6	Calibration Factors measured at 900MHz $\epsilon' = 40.26$ $\epsilon'' = 20.88$ $z = 22.7mm$	38
5.7	Calibration Factors measured at 1800MHz $\epsilon' = 39.17$ $\epsilon'' = 14.69$ $z = 22.7mm$	39
6.1	Total experiments for compliance testing . . . . .	52
6.2	Measured 1g and 10g averages for cell-phone compliance tests . . . . .	55

# List of Figures

2.1	Typical E-field probe orthogonal dipole construction . . . . .	8
2.2	E-field probe protective cover . . . . .	9
2.3	Yee Unitg Cell for FDTD mesh . . . . .	13
2.4	Time Marching for FDTD calculation . . . . .	13
2.5	Flow chart for FDTD Simulation Steps . . . . .	15
3.1	Flat Phantom used for system test and validation . . . . .	17
3.2	Specific Anthropomorphic Mannequin Phantom (SAM) used for compliance test . . . . .	17
3.3	Calibration System Setup for calculating dielectric parameters and calibration factors . . . . .	20
3.4	Power reflectance $\Gamma_1$ at air-acrylic interface . . . . .	22
3.5	Boundary Effect near Dielectric slab and Tissue-Equivalent liquid Boundary	24
3.6	Errors in the measurement of a variable $X$ . . . . .	27
3.7	Propagation of errors into experimental results . . . . .	28
4.1	E-field probe scan along Waveguide z-axis . . . . .	30
4.2	E-field probe isotopic scan about its axis inside the Waveguide . . . . .	32
4.3	Net power calculation from forward and reverse power measurements . . . . .	33
5.1	Normalized $ E ^2$ attenuation inside 1800MHz waveguide $\epsilon' = 39.86$ $\epsilon'' = 13.59$	38
5.2	Power Reflectance at the air-acrylic boundary for 900MHz waveguide $\epsilon' = 40.62$ $\epsilon'' = 19.00$ . . . . .	39
5.3	Probe isotropy measured at 1800MHz ( $\epsilon' = 39.17$ $\epsilon'' = 14.69$ $z = 22.7mm$ ) .	40
5.4	Change in complex permittivity due to change in power reflectance $ \Gamma ^2$ ( $\epsilon' = 40.62$ $\epsilon'' = 19.00$ ) . . . . .	42
5.5	Change in complex permittivity due to change in frequency $f$ ( $\epsilon' = 40.62$ $\epsilon'' = 19.00$ ) . . . . .	43
5.6	Change in complex permittivity due to change in waveguide dimension $a$ ( $\epsilon' = 40.62$ $\epsilon'' = 19.00$ ) . . . . .	44
5.7	Change in complex permittivity due to change in attenuation factor $\alpha$ ( $\epsilon' = 40.62$ $\epsilon'' = 19.00$ ) . . . . .	45
5.8	Change in complex permittivity due to change in slab permittivity ( $\epsilon' = 40.62$ $\epsilon'' = 19.00$ ) . . . . .	46
5.9	Change in calibration factors due to change in real permittivity $\epsilon'$ ( $\epsilon' = 40.00$ $\epsilon'' = 13.98$ $z = 15mm$ ) . . . . .	47
5.10	Change in calibration factors due to change in imaginary permittivity $\epsilon''$ ( $\epsilon' = 40.00$ $\epsilon'' = 13.98$ $z = 15mm$ ) . . . . .	48

5.11	Change in calibration factors due to change in angular frequency $w$ ( $\epsilon' = 40.00$ $\epsilon'' = 13.98$ $z = 15mm$ ) . . . . .	49
5.12	Change in calibration factors due to change in waveguide dimension $a$ ( $\epsilon' = 40.00$ $\epsilon'' = 13.98$ $z = 15mm$ ) . . . . .	50
6.1	Cell-phone cheek position . . . . .	52
6.2	Cell-phone tilt position . . . . .	53
6.3	Cell-phone compliance testing using the SAM phantom . . . . .	54
6.4	Motorola phone at 900MHz in the right cheek position . . . . .	56
6.5	Nokia phone at 1800MHz in the left tilt position . . . . .	57
A.1	E-Field probe SPEAG 1422 . . . . .	61
A.2	Flat Phantom for system validation . . . . .	62
A.3	Left and Right SAM Phantoms for compliance testing . . . . .	63
A.4	900MHz waveguide (left) 1800MHz waveguide (right) . . . . .	64
A.5	Waveguide Z-Scan setup . . . . .	65
A.6	Waveguide Iso-Scan . . . . .	66
A.7	Compliance testing setup . . . . .	67
B.1	Rectangular Waveguide . . . . .	68
C.1	Power reflectance for Two Layers inside a Waveguide . . . . .	71
D.1	Main Menu Window . . . . .	75
D.2	File dialog window . . . . .	76
D.3	Iso-Scan Results Window . . . . .	76
D.4	Z-Scan Results Window . . . . .	77
D.5	Probe Holder Calibration . . . . .	77
D.6	Probe Holder with contact in Sensor 1 . . . . .	78
D.7	Iso-Scan Parameter Window . . . . .	78
D.8	Iso-Scan Window . . . . .	79
D.9	Manual Move Window . . . . .	80
D.10	Find Bottom Window . . . . .	80
D.11	Z-Scan Parameter Window . . . . .	80
D.12	Status Window . . . . .	81
D.13	Elapsed Time Window . . . . .	81
E.1	Forward (For), Reverse (Rev), and Insertion (Ins) Coupler Loss versus Frequency . . . . .	126
E.2	Cable Insertion Loss versus Frequency . . . . .	127

# List of Abbreviations

dB	Decibel ( $= 10 \log_{10}(\textit{ratio})$ )	
EM	Electro Magnetic	
FDTD	Finite Difference Time Domain	
Hz	Hertz	$\frac{1}{s}$
IEEE	The Institute of Electrical and Electronic Engineers	
RF	Radio Frequency	
rms	root mean squared	
SAR	Specific Absorption Rate	W/Kg
VNA	Vector Network Analyser	

# List of Symbols

C	specific heat
D	electric displacement
E	electric field
f	frequency
$\alpha$	attenuation factor
$\delta$	skin depth
$\Delta$	difference
$\epsilon'$	real permittivity
$\epsilon''$	imaginary permittivity
$\mu$	magnetic permeability
$\lambda$	wavelength
$\pi$	pi ( $\sim 3.141592654$ )
$\sigma$	electrical conductivity
$\omega$	angular frequency
W	Watts

# Chapter 1

## Introduction

For many years there has been concern on the part of the general public about the possible health effects of exposure to radio frequency (RF) radiation. High levels of RF field are known to cause a variety of physical effects on the human body. Although a relatively small group of radio users and technicians has been exposed by virtue of their occupations for many decades, with the dramatic increase in public use particularly of mobile telephones and other wireless devices, it has become necessary to ensure that these products do not expose their users to potentially harmful levels of field.

At the frequencies of operation of most of these devices, the known health effects center around tissue heating. A measure of this heating effect is known as Specific Absorption Rate (SAR). As part of worldwide efforts to legislate on consumer health and safety aspects, many authorities now require products that are placed on the market to meet limits on SAR. Measurement of SAR is therefore becoming a fast-growing requirement for companies that make such products.

An SAR measurement system should not only meet current International standards but should provide flexibility and support new standards as they evolve. To achieve compliance the SAR measurement system must have an overall measurement uncertainty below 30% for a 95% confidence level. Uncertainty reflects the accuracy of a measured result as compared

to the true one. Overall measurement uncertainty is determined by calibration, simulation, and combining the individual uncertainties of all system elements. The objective of this research is to design a waveguide calibration system for miniature E-field probe calibrations and dielectric properties measurements that reduces the overall measurement uncertainty of the SAR measurement system.

## 1.1 Synopsis

Wireless devices must meet specific safety radiation limits, and in order to assess the health affects of such devices, standard procedures are used in which standard phantoms, tissue-equivalent liquids, and miniature electric-field probes are used. The phantom is irradiated by the wireless device under test with strict geometric conditions and spatial SAR measurements are made. The accuracy of such measurements depend on the precision in measuring the dielectric properties of the tissue-equivalent liquids and the associated calibrations of the electric-field probes.

This thesis describes work on the theoretical modelling and experimental measurement of the complex permittivity of tissue-equivalent liquids, and associated calibration of miniature electric-field probes. The measurement method is based on measurements of the field attenuation factor and power reflection coefficient of a tissue-equivalent sample. A novel method for determining the dielectric properties and probe calibration factors is described and validated.

Accurate dielectric measurements on lossy media are few and far between. And for SAR compliance testing, dielectric measurements are generally made with open ended coaxial probes, which are of uncertain accuracy. The technique for measuring dielectric properties and associated calibration factors using e-field probes and waveguides, which is described in this thesis, is highly accurate and provides a standard for future measurements.

The University of Maryland plays a leading role in the International Intercomparison of SAR measurements made on anthropomorphic phantoms [1]. In this work many international laboratories made measurements with cell phones using a Specific Anthropomorphic Mannequin phantom (SAM).

The work presented in this thesis is the first complete and accurate assessment of probe calibration, simulant fluid characterization, and actual cell phone SARs made for verifying the validity of specified verification protocols for cell phone certification. These measurements have been carried out independently of any manufacturer of phantoms, cell phones, dielectric measurement probes, or manufacturer supplied probe calibration factors.

## 1.2 Brief Overview of Thesis

An overview of the remainder of the thesis is given in this section. Chapter 2 reviews background information on the standards, limits, and testing procedures for quantifying SAR. In order to measure exposure limits, the dielectric properties of the tissue-equivalent liquid used and the calibration factors for the probe used must be precisely calculated.

In chapter 3, the experimental design and approach for the calibration system is presented. A novel waveguide system is presented for both dielectric measurements and calculating the associated e-field probe calibration factors.

Chapter 4 gives the procedures used for calculating the dielectric properties, using field attenuation and power reflectance, and measuring the e-field probe calibration factors, using probe isotropy data.

System validation using standard saline solutions at different concentrations and are presented in chapter 5. Dielectric properties and calibration factors are calculated for tissue-equivalent liquids at 900MHz and 1800MHz. Complete assessments of system uncertainties are also presented in chapter 5.

Chapter 6 presents cell phone compliance testing, as part of an international intercomparison of SAR measurements, made on a SAM phantom at 900MHz and 1800MHz.

## Chapter 2

# Background Information

Concern about human exposure to RF fields is not new; indeed it has been the driving force behind standards that ensure safe levels of RF exposure. Even though RF signals used for wireless communications belong to the non-ionizing class of radiation, excessive exposure to these RF energy fields can create undesired heating effects; under certain conditions, overheating surpasses the thermoregulation process of the affected organs, producing chronic health effects. For absorption of energy, electromagnetic fields can be divided into four frequency ranges:

1. Frequencies from about 100KHz to less than about 20MHz, at which absorption in the trunk of the body decreases rapidly with decreasing frequency, and significant absorption may occur in the neck and legs.
2. Frequencies in the range from about 20MHz to 300MHz, at which relatively high absorption can occur in the whole body, and even higher absorption values if partial body (e.g., head) resonances are considered.
3. Frequencies in the range from about 300 MHz to several GHz, at which significant local, nonuniform absorption occurs.
4. Frequencies above about 10GHz, at which energy absorption occurs primarily at the body surface.

## 2.1 Tissue Heating and Regulations

Experimental evidence indicates a body temperature increase of less than  $1^{\circ}\text{C}$  for a 30 minute exposure to an electromagnetic field producing a whole body SAR of 4 W/kg. More intense exposure can cause harmful levels of tissue heating. Hence the occupational exposure restriction is set at 0.4 W/kg (with a safety factor of 10). General public exposure restriction is set to 0.08 W/kg (with an additional safety factor of 5) [2].

Restrictions on exposure are based on established health effects and are termed basic restrictions. Depending on frequency, the physical quantities used to specify the basic restrictions on exposure to electromagnetic fields are current density, SAR, and power density. Protection against adverse health effects requires that these basic restrictions are not exceeded.

Reference levels of exposure are provided for comparison with measured values of physical quantities (electric or magnetic field strength); compliance with all reference levels given in guidelines will ensure compliance with basic restrictions. If measured values are higher than reference levels, it does not necessarily follow that the basic restrictions have been exceeded, but a more detailed analysis is necessary to assess compliance with the basic restrictions.

Two limits are used: a lower value for exposure averaged over the whole body, and a higher value which is applicable to local exposure to parts of the body (e.g. the head). This partial body SAR is averaged over a volume of tissue defined as a tissue volume in the shape of a cube. The US requirements differ from the European requirements in their demand for a lower spatial average limit and that this limit be averaged over a smaller volume (1g of tissue as opposed to 10g). They also require a longer time over which the SAR is to be averaged; but since it is assumed that a user of a portable device will be exposed to the maximum power available from the device for the duration of the specified averaging time, in effect the requirement for time averaging of the output during SAR measurement does not apply. The whole-body SAR limit is assumed not to be exceeded if it can be shown (usually the case) that it is not exceeded over the measurement volume actually used, for portable devices which expose only a small part of the body. Guidelines for occupational and general public expositors are shown in Table 2.1 and Table 2.2.

Table 2.1: SAR test standards for Occupational exposure

	USA	Australia	Europe	Japan	New Zealand
Whole Body	0.4 W/kg	0.4 W/kg	0.4 W/kg	0.4 W/kg	0.4 W/kg
Spatial Peak	8 W/kg	10 W/kg	10 W/kg	8 W/kg	10 W/kg
Averaging Time	6 min	6 min	6 min	6 min	6 min
Averaging Shape	1g	10g	10g	10g	10g
Shape	Cube	Cube	Cube	Cube	Cube

Table 2.2: SAR test standards for General Public exposure

	USA	Australia	Europe	Japan	New Zealand
Whole Body	0.08 W/kg	0.08 W/kg	0.08 W/kg	0.04 W/kg	0.08 W/kg
Spatial Peak	1.6 W/kg	2 W/kg	2 W/kg	2 W/kg	2 W/kg
Averaging Time	30 min	6 min	6 min	6 min	6 min
Averaging Shape	1g	10g	10g	10g	10g
Shape	Cube	Cube	Cube	Cube	Cube

## 2.2 RF Dosimetry

RF Dosimetry is the process that quantifies the magnitude and distribution of the RF energy absorbed by an object when it's exposed to RF fields. The parameter measured in RF Dosimetry is the Specific Absorption Rate. In the health context SAR is the rate at which radio frequency energy is dissipated in human tissues due to the exposure to antenna radiation. SAR is expressed in W/kg. The SAR value is related not only to the incident electromagnetic (EM) waves but also the electrical and geometric characteristics of the exposed tissue. SAR is strongly related to the incident electric field strength  $E$  as well as to the dielectric properties of the tissue, Equation (2.1)

$$SAR = \frac{\sigma |E|^2}{\rho} \quad (2.1)$$

where  $\sigma$  is the tissue conductivity (S/m),  $\rho$  is the density of the averaging mass (kg/m<sup>3</sup>), and  $|E|$  is the Root Mean Square (RMS) Hermitian magnitude (V/m) value of the local

electric field, Equation (2.2)

$$|E| = \sqrt{|E_x|^2 + |E_y|^2 + |E_z|^2} \quad (2.2)$$

where  $E_x$ ,  $E_y$ , and  $E_z$  are the RMS values of the  $x$ ,  $y$ , and  $z$  components of the electric field.

SAR measurements based on the effects of the E-field are not absolutely accurate because interactions of the magnetic field  $H$  are not taken into account [3]. Maximum levels of SAR are published in the ICNIRP international safety guidelines [2] and IEEE Standard C95.3 [4].

Experimental SAR measurements can also be implemented using techniques that do not require EM measurements [4, 5]. Calorimetry, Thermometry and Thermography are techniques based on the measurement of the heat produced by intrinsic interactions between the EM fields and the biological tissue structure. SAR can be related to the increase in temperature at a point by Equation (2.3)

$$SAR = \left. \frac{C\Delta T}{\Delta t} \right|_{t=0} \quad (2.3)$$

where  $\Delta T$  is the change in temperature ( $^{\circ}C$ ),  $\Delta t$  is the duration of exposure (s), and  $C$  is the specific heat capacity ( $J/kg^{\circ}C$ )

Calorimetry addresses Whole-Body SAR while Thermography and Thermometry address SAR distributions (Local SAR).

### 2.2.1 E-Field Probes

SAR measurements are routinely done with miniature electric field (E-field) probes. In the near field of a wireless handset, the EM field distributions may have sharp spatial variations in both magnitude and polarization. Thus, the ideal field probe for measuring SAR must be much smaller than the wavelength in a tissue-equivalent liquid, be isotropic,

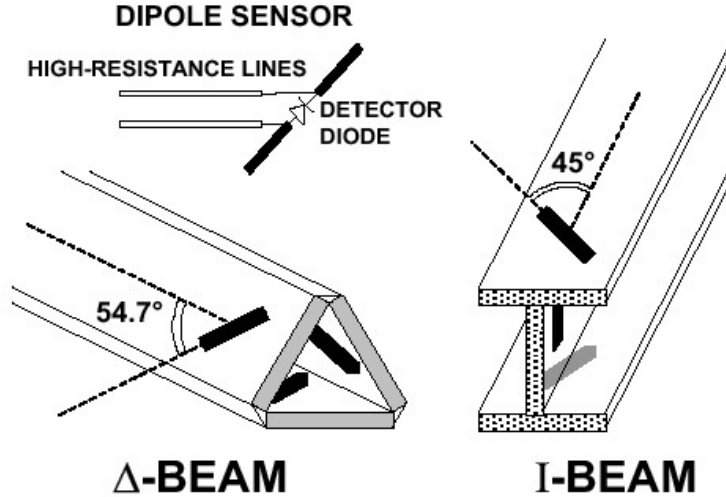


Figure 2.1: Typical E-field probe orthogonal dipole construction

exhibit a linear response to the square of the incident electric field strength, and should be transparent (nonperturbing) to the measured field [6]. E-field probes consist of a set of three mutually orthogonal center-fed short dipole antennas [7]. Each sensor of the probe consists of the following components: an electrically short dipole antenna, a diode detector at the dipole feed-point, a dielectric mechanical support, and a highly resistive, RF-transparent, differential transmission line (feed-line) to extract the signal detected by the diode while maintaining the RF-transparency of the line, Figure 2.1, (Figure A.1 Appendix A).

A dielectric cover (typically a cylindrical low-loss plastic sleeve) encloses the probe for chemical and mechanical protection, Figure 2.2.

For small RF signals, an ideal detector diode operates in the square-law region providing a rectified output voltage that is proportional to the RMS of the corresponding E-field component. The probe itself consists of three such sensors and has three output ports, each one providing a DC voltage resulting from the filtering performed by the resistive feed-line, which acts as a distributed RC low-pass filter of the rectified sensor outputs, Equation (2.5)

$$|E| = \sqrt{|E_1|^2 + |E_2|^2 + |E_3|^2} \quad (2.4)$$

$$|E| = \sqrt{\frac{V_1}{k_1} + \frac{V_2}{k_2} + \frac{V_3}{k_3}} \quad (2.5)$$

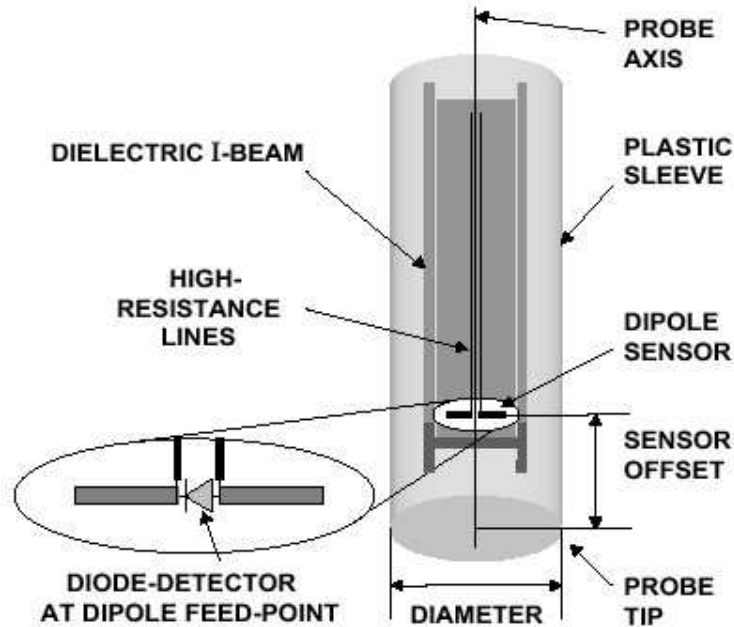


Figure 2.2: E-field probe protective cover

where  $E_i$ ,  $V_i$  and  $k_i$  are the corresponding Electric field strength, voltage, and sensitivity (calibration factor) of dipole  $i$ , ( $i = 1, 2, 3$ ). In the square-law region  $|E_i|^2 = \frac{V_i}{k_i}$ .

The sensitivity of the probe output to the calibration factors is necessary to determine the probe-related calibration and measurement uncertainty. Deviations between the measurement and calibration configurations and conditions will increase the measurement uncertainty. Calibration should be preceded by a complete characterization of the probe independently of the measurement system, in order to evaluate the probe response to the above factors. It will also be necessary to calibrate the probe in different tissue-equivalent liquids. It is necessary for each calibration to indicate the range of parameters (permittivity, conductivity, frequency, temperature) for which the assessed probe uncertainty is valid.

### 2.2.2 Tissue-Equivalent Liquids

Tissue-equivalent liquids are used to simulate human tissues in phantom filled SAR measurement experiments and in waveguides to calibrate E-field probes. The dielectric parameters

required are the complex relative permittivity of the tissue-equivalent liquid at specific test frequencies and temperatures, Equation (2.7).

$$\epsilon_r = \epsilon' - j\epsilon'' \quad (2.6)$$

$$\epsilon_r = \epsilon' - j\frac{\sigma}{\omega\epsilon_0} \quad (2.7)$$

where  $\epsilon_r$  is the liquid relative permittivity,  $\epsilon'$  and  $\epsilon''$  are the real and imaginary parts of the complex permittivity,  $\epsilon_o$  is the free space permittivity,  $\sigma$  is the liquid conductivity, and  $\omega = 2\pi f$  is the radian frequency, where  $f$  is the frequency of operation.

Because these properties are frequency-dependent, a different liquid must be formulated for each test frequency band. The standards give specific requirements for the permittivity and conductivity at each cell-phone frequency band, Table 2.3 [8, 9]. Since recipes for ingredients do not produce exactly correct values, partly because of inaccuracies in mixing and partly because of variations in the properties of each ingredient, the actual values (rather than the standard specification) must be measured and specified in tests. Table 2.4 shows typical tissue-equivalent recipes at 900 MHz and 1800 MHz.

Table 2.3: Target dielectric values for tissue-equivalent liquids at specific frequencies

Frequency (MHz)	Relative Permittivity $\epsilon'$	Conductivity $\sigma$ (S/m)
300	45.3	0.87
450	45.3	0.87
835	41.5	0.90
900	41.5	0.97
1450	40.5	1.20
1800	40.0	1.40
1900	40.0	1.40
2000	40.0	1.40
2450	39.2	1.80
3000	38.5	2.40

The response of the probe's sensors depend on the dielectric parameters of the surrounding media and the signal frequency. The probe must therefore be calibrated in media having dielectric properties that are equivalent to the mixtures that will be used for the tissue-equivalent liquids at the operational frequencies of the wireless devices being tested. Uncertainties due to liquid dielectric measurements affect the accuracy of the probe calibration

Table 2.4: Typical tissue-equivalent recipes given in weight percentages

	900MHz	1800MHz
Bactericide	0.10%	
Diethylene Glycol Butyl Ether (DGBE)		47.00%
Hydroxyethyl Cellulose (HEC)	1.00%	
NaCl	1.48%	0.36%
Sucrose	56.50%	
Water	40.92%	52.64%

factors, and in turn, the system overall uncertainty [10]. Therefore, probe calibration must be assessed in different tissue-equivalent liquids exhibiting different dielectric properties.

## 2.3 FDTD Simulation

SAR prediction in the human body is normally done using the Finite Difference Time Domain (FDTD) technique [11, 12, 13]. The FDTD method is the most successful and most promising numerical method in this application [14]. The FDTD method is used for SAR assessments and validation in standard phantoms [15]. This method adapts very well to complex tissue models and offers great flexibility in modeling the inhomogeneous structures of anatomical tissues and organs [16]. The FDTD method was originally developed by Kane S. Yee [17], in 1966, as a three dimensional solution of Maxwell’s curl equations. In principle, a volume of space containing any object or collection of objects is subjected to an electromagnetic disturbance, FDTD then solves for the fields throughout the volume as a function of time.

Numerical simulations using FDTD of complex anatomically correct human models and the simplified Specific Anthropomorphic Mannequin phantom (SAM) used for compliance testing have shown that the SAM phantom yields a conservative exposure estimate for all heads considered, and particularly that there was no trend for higher RF absorption in the smaller phantom heads. The observed variations within the different anatomical models were clearly related to individual anatomical characteristics of the head, such as tissue distribution or pinna thickness, but not head size.

The FDTD method replaces both spatial and time derivatives of Maxwell's equations with finite difference approximations. Maxwell's two coupled curl equations in the time domain are given by Equation (2.8) and Equation (2.9)

$$\nabla \times E = -\mu \frac{\partial H}{\partial t} - M \quad (2.8)$$

$$\nabla \times H = \epsilon \frac{\partial E}{\partial t} + J \quad (2.9)$$

where  $J$  and  $M$  are the electric current and magnetic current densities, respectively.

The components of the electric field  $E$  and the magnetic field  $H$  are specified in the Yee unit cell as shown in Figure 2.3. There is one  $E$ -field component located at each edge of the Yee unit cell and one  $H$ -field component located at the center of each cell face. The  $E$ -fields and  $H$ -fields are positioned a half-cell away. The advantages of this field arrangement are that center differences are realized in the calculation process of each field component and continuity of the tangential field component is automatically satisfied [18]. The  $x$ ,  $y$ , and  $z$  dimensions of the unit cell in Cartesian coordinates are  $\Delta x$ ,  $\Delta y$ , and  $\Delta z$ , respectively. The computational domain is thus obtained by stacking these unit cells into a large problem space. The  $E$  and  $H$  fields are separated by a half-cell both in space and time. The time marching is modeled as the multiplication of unit time step,  $\Delta t$ . The discretization in time is explained in Figure 2.4.

Applying the central difference approximations

$$\frac{\partial f}{\partial x} \approx \frac{f(x + \frac{\Delta x}{2}) - f(x - \frac{\Delta x}{2})}{\Delta x} \quad (2.10)$$

to Maxwells curl equations, the finite difference equations [19] are by Equation (2.11) and Equation (2.12)

$$\begin{aligned} E_x^{n+1}(i, j, k) = & \frac{2\epsilon - \sigma\Delta t}{2\epsilon + \sigma\Delta t} E_x^n(i, j, k) \\ & - \frac{2\Delta t}{(2\epsilon + \sigma\Delta t)\Delta z} [H_y^{n+1/2}(i, j, k) - H_y^{n+1/2}(i, j, k - 1)] \\ & + \frac{2\Delta t}{(2\epsilon + \sigma\Delta t)\Delta y} [H_z^{n+1/2}(i, j, k) - H_z^{n+1/2}(i, j - 1, k)] \end{aligned} \quad (2.11)$$

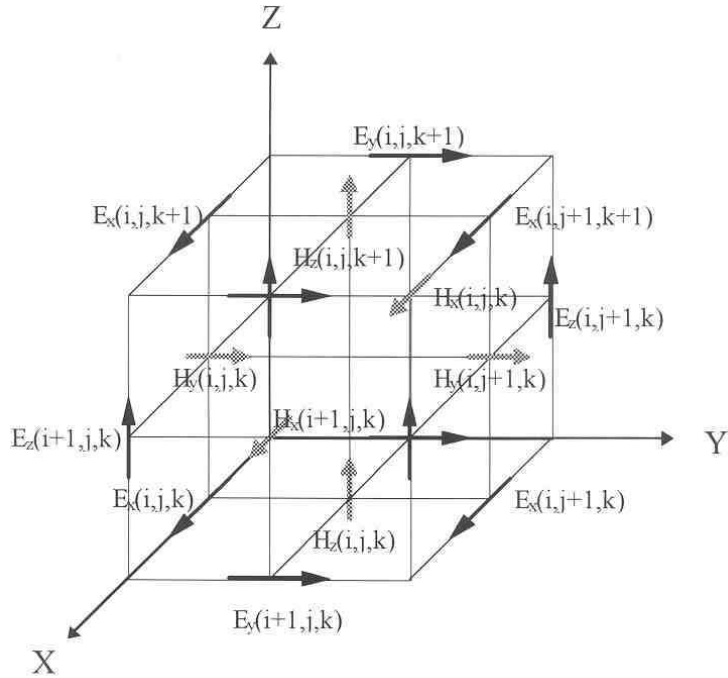


Figure 2.3: Yee Unit Cell for FDTD mesh

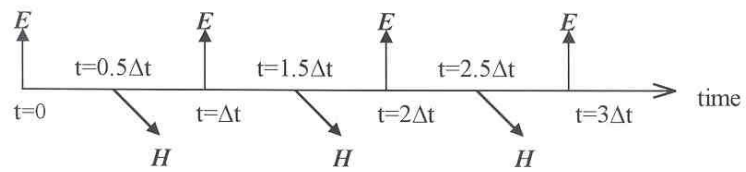


Figure 2.4: Time Marching for FDTD calculation

$$\begin{aligned}
H_x^{n+1/2}(i, j, k) &= \frac{2\mu - \sigma^* \Delta t}{2\mu + \sigma^* \Delta t} H_x^{n-1/2}(i, j, k) \\
&\quad - \frac{2\Delta t}{(2\mu + \sigma^* \Delta t) \Delta z} [E_y^n(i, j, k+1) - E_y^n(i, j, k)] \\
&\quad + \frac{2\Delta t}{(2\mu + \sigma^* \Delta t) \Delta y} [E_z^n(i, j+1, k) - E_z^n(i, j, k)]
\end{aligned} \tag{2.12}$$

where  $\sigma$  and  $\sigma^*$  are the electric and magnetic conductivities respectively.

The update equations for  $E_y$ ,  $E_z$ ,  $H_y$ , and  $H_z$ , field components can also be formulated in a similar manner. Figure 2.5 shows the main steps taken in an FDTD simulation. Initially, a model is made to represent the physical structure, including conductors, dielectrics, and boundaries. Next an applied pulse, normally either a sine wave or a Gaussian pulse, acts as the input stimulus at all the sources. Then at increments of time the E and H fields are calculated. After each increment the input electric field amplitude is calculated and the E and H fields are again recalculated.

The FDTD method is very easily implemented, gives an exact solution, and, because the fields are computed in the time domain, this method gives wide band results via a Fast Fourier Transform (FFT).

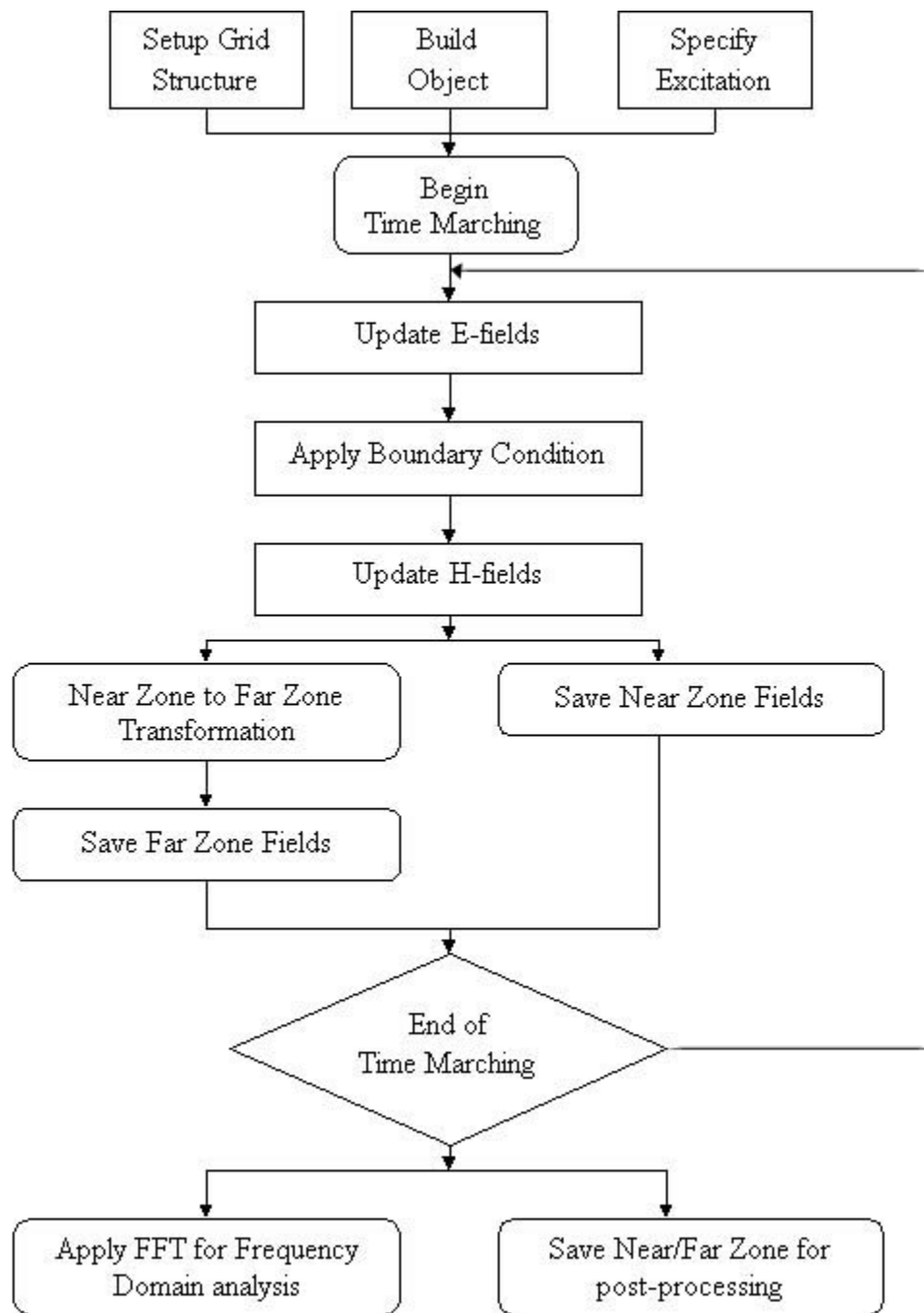


Figure 2.5: Flow chart for FDTD Simulation Steps

## Chapter 3

# Experimental Design and Approach

SAR compliance measurements are performed using small diameter E-field probes. The probe is moved inside a phantom by a high precision positioning system. Two- and three-dimensional scans are taken in the exposed area. A rectangular (planar) phantom is required for system test and validation [8], Figure 3.1 (Figure A.2 Appendix A). A standardized anthropomorphic phantom called the SAM (Specific Anthropomorphic Mannequin) is required for compliance testing [8], Figure 3.2 (Figure A.3 Appendix A). The Device Under Test (DUT) is held under the phantom by a non-conductive positioner designed for stability and repeatability. The phantoms are filled with a tissue-equivalent liquid whose formulation is specified [8] at various operating frequencies, Table 2.3. Preliminary scanning procedures find peak-SAR location. 3D scans collect measuring points to calculate 1g and/or 10g spatial volume average SAR. Maximum spot SAR is measured before and after the 3D scan to ensure a minimum DUT power drift.

Overall uncertainty is determined by identifying uncertainties in the instrumentation chain involved in the procedures associated with SAR evaluation. Elements that contribute to the overall uncertainty are:

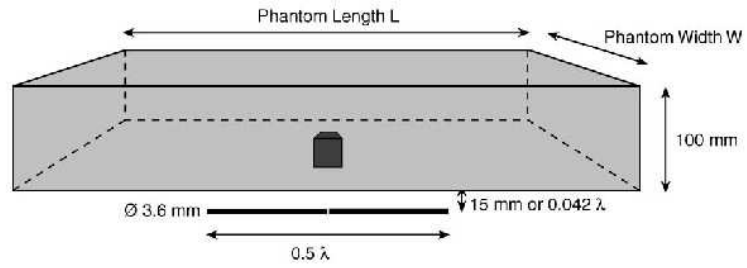


Figure 3.1: Flat Phantom used for system test and validation

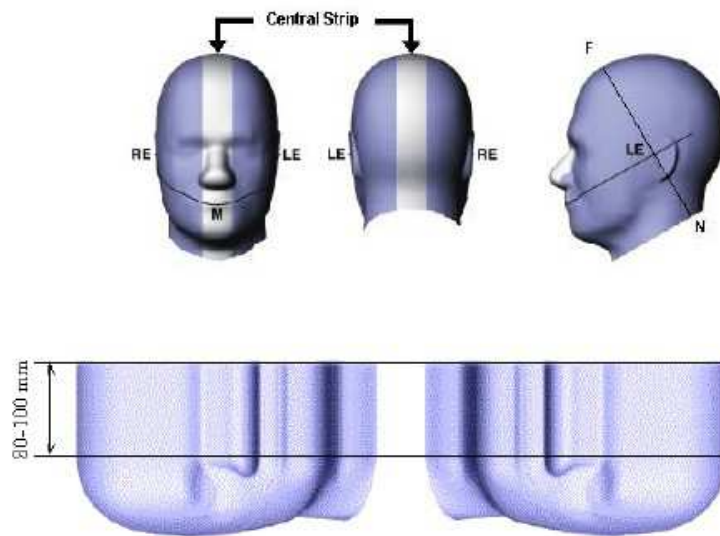


Figure 3.2: Specific Anthropomorphic Mannequin Phantom (SAM) used for compliance test

- E-field probes.
- SAM phantom.
- Tissue-equivalent liquid mixture.
- DUT positioning.
- E-field probe positioning system.
- System software and data processing.

The overall uncertainty assessment should be performed for all of the components involved in the SAR measurement technique under different standardized procedures. Many of the individual uncertainties are calculated from the tolerances of the instrumentation used. Other uncertainties must be determined empirically by analysis of variability after repeated measurements.

In order to perform the uncertainty measurement assessment, the following procedures must be addressed:

- E-field probe calibration and measurement of accuracy in a standardized exposure situation.
- Measurement of the dielectric properties of the particular tissue-equivalent at the required operating frequencies.
- Measurement of the thickness variations of the SAM phantom.
- Measurement of power drift to validate DUT holders and positioning system repeatability.
- The 1g and 10g SAR averaging algorithms.

The overall uncertainty of the SAR measurement system is determined by the methods outlined above and in accordance with the appropriate IEEE standard [8].

To calibrate an E-Field probe, or measure the dielectric properties of a tissue-equivalent liquid they are placed in a precisely known electric field, either calculated from the input power of the system, calculated from local electric field, or determined from the temperature rise of the medium. Waveguides can be utilized to generate an analytically known field inside tissue simulating liquids or air [20] (Figure A.4 Appendix A). The use of waveguides and other transmission lines for E-Field probe calibrations has some clear advantages over open field systems:

- No anechoic chamber shielding for radiated interferences is needed
- The system is compact
- The RF power needed is minimized

Calibration systems have been constructed for 900 and 1800 MHz. The design of these calibration systems are subject to detailed theoretical analysis and computer simulation. These systems will include software to coordinate the operation of the required laboratory instruments, gather the required data, and process the data into dielectric properties and calibration factors.

### **3.1 Experimental Setup**

Figure 3.3 shows the calibration system setup (Figure A.5 Appendix A). The central component of the calibration system is a vertically mounted rectangular waveguide. The upper part of the waveguide is separated from the lower part with a watertight dielectric slab.

The upper part of the waveguide is filled with a tissue-equivalent liquid. The depth of this tissue equivalent liquid is typically larger than three times the skin depth of the liquid which

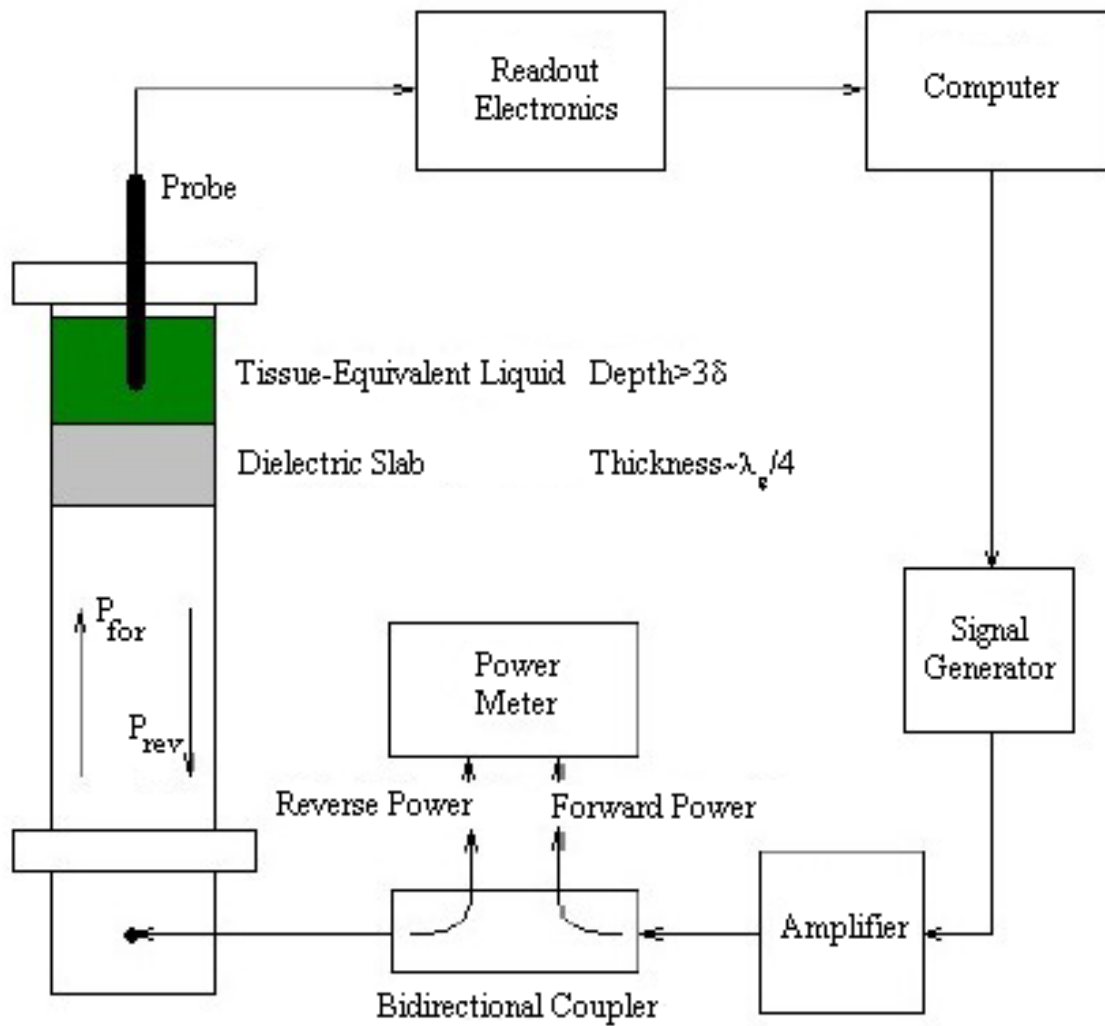


Figure 3.3: Calibration System Setup for calculating dielectric parameters and calibration factors

will decay the fields inside the liquid significantly and prevent reflections from interfering with the desired signals. The width of the dielectric slab is set to a quarter-wavelength to maximize power absorbed in the tissue-equivalent liquid.

The microwave power is fed through a coaxial cable to a waveguide post located in the lower part of the guide. The net power absorbed in the liquid is calculated using the forward and reflected power measurements inside the waveguide, Equation (3.1)

$$P_{net} = P_{for} - P_{rev} \quad (3.1)$$

## 3.2 Calibration Procedure

It is necessary to operate the E-field probe in the square-law region so that the sum of the DC voltage outputs from the three dipoles is proportional to the square of the internal electric field magnitude. For SAR measurements, it is therefore necessary that the E-field probe be checked for square-law region behavior, by varying the net power absorbed in the tissue-equivalent liquid, the output of the probe should increase linearly with the net power for each of the test locations.

Another important characteristic of the probe that affects the measurement accuracy is its isotropy. Since the orientation of the induced electric field is generally unknown, the E-field probe should be relatively isotropic in its response to the orientation of the E-field.

The calibration procedure has several steps. The algorithm of the calibration procedure is shown below:

**Square-Law Region** The probe output is measured at different input power levels to insure square-law region operation

**Probe Tip Position** To perform the isotropy scan the probe tip should not be close to media boundaries (less than one probe-tip diameter), or deep inside the liquid where the fields have decayed significantly (skin-depth)

**Dielectric Properties** A scan along the waveguide z-axis is performed. The probe voltage is then measured as a function of net power and position in the liquid. The dielectric properties are calculated using the field attenuation factor and power reflectance at the air-dielectric slab boundary

**Calibration Factors** The probe is rotated about its axis to acquire isotropic data. The probe voltage is then measured as a function of net forward power in the liquid. The calibration factors are calculated using linear least-square fits

**Uncertainty Analysis** Evaluating overall uncertainty associated with calibration procedures

### 3.2.1 Power Reflectance

Power reflectance is measured at the air-dielectric slab interface, Figure 3.4.

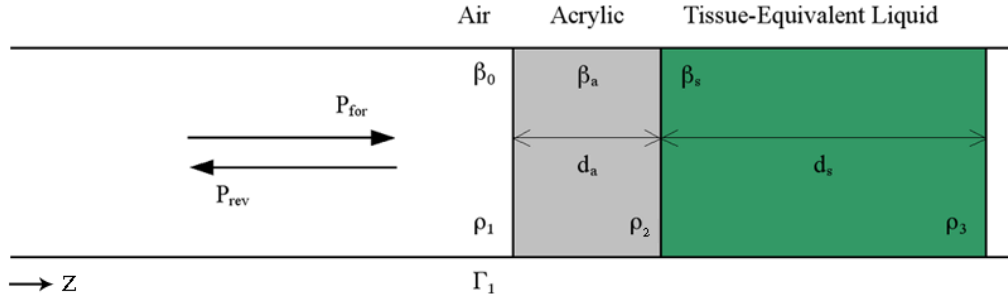


Figure 3.4: Power reflectance  $\Gamma_1$  at air-acrylic interface

The analytical formula for the power reflectance as a function of  $\epsilon'$  and  $\epsilon''$  at the air-dielectric slab interface is given by Equation (3.2). Refer to Appendix C for a detailed derivation.

$$|\Gamma_1|^2 = \left| \frac{\rho_1 + \rho_2 e^{-2\beta_a d_a} + \rho_1 \rho_2 \rho_3 e^{-2\beta_s d_s} + \rho_3 e^{-2\beta_a d_a} e^{-2\beta_s d_s}}{1 + \rho_1 \rho_2 e^{-2\beta_a d_a} + \rho_2 \rho_3 e^{-2\beta_s d_s} + \rho_1 \rho_3 e^{-2\beta_a d_a} e^{-2\beta_s d_s}} \right|^2 \quad (3.2)$$

where

$$\rho_1 = \frac{z_a - z_0}{z_a + z_0} \quad \rho_2 = \frac{z_s - z_a}{z_s + z_a} \quad \rho_3 = \frac{z_0 - z_s}{z_0 + z_s} \quad (3.3)$$

$$z_0 = \frac{j\omega\mu_0}{\beta_0} \quad z_a = \frac{j\omega\mu_0}{\beta_a} \quad z_s = \frac{j\omega\mu_0}{\beta_s} \quad (3.4)$$

$$\beta_0 = \sqrt{\left(\frac{\pi}{a}\right)^2 - \omega^2\mu_0\epsilon_0} \quad \beta_a = \sqrt{\left(\frac{\pi}{a}\right)^2 - \omega^2\mu_0\epsilon_a} \quad \beta_s = \sqrt{\left(\frac{\pi}{a}\right)^2 - \omega^2\mu_0\epsilon_s} \quad (3.5)$$

The  $\rho$ 's are the elementary reflection coefficients at each interface, the  $z$ 's are the media impedances, and the  $\beta$ 's are the propagation constants.

### 3.2.2 Fundamental Mode

Substituting the complex permittivity of the Tissue-Equivalent Liquid in the expression for the fundamental mode ( $TE_{10}$ ) inside the waveguide and using Taylor expansion, yields the following analytical formula for the electric field RMS magnitude inside the liquid as a function of position and the net power absorbed, Equation (3.6). Refer to Appendix B for a detailed derivation.

$$|E| = \sqrt{\frac{4P\omega\mu_0}{ab2\beta}} \sin\left(\frac{\pi}{a}x\right) e^{\frac{-z\omega\mu_0\sigma}{2\beta}} \quad (3.6)$$

$$\beta = \sqrt{\omega^2\mu_0\epsilon_0\epsilon' - \left(\frac{\pi}{a}\right)^2} \quad (3.7)$$

$$\sigma = \omega\epsilon_0\epsilon'' \quad (3.8)$$

where  $P$  is the net power absorbed in the liquid,  $\omega$  is the radian frequency,  $\mu_0$  is the free space permeability,  $\epsilon_0$  is the free space permittivity,  $\epsilon'$  is the liquid relative permittivity,  $a$  and  $b$  are the waveguide cross-sectional dimensions,  $\beta$  is the propagation constant,  $\sigma$  is the simulant conductivity,  $z$  is the position of the probe along the waveguide z-axis,  $x$  is the position of the probe along the waveguide x-axis.

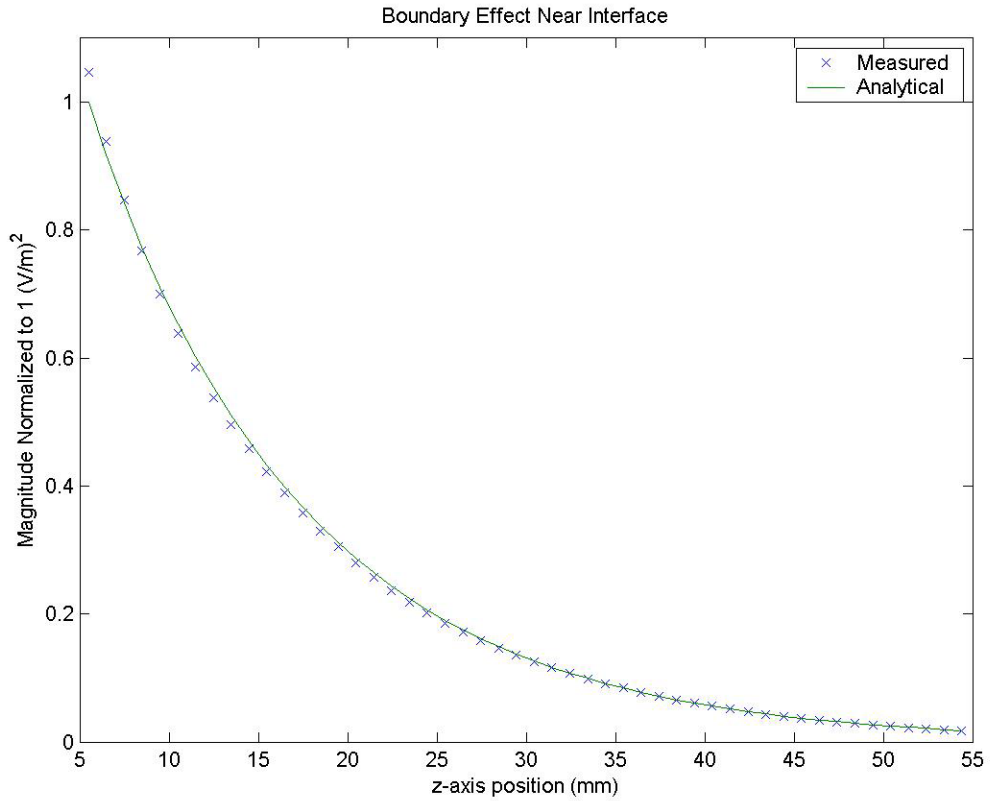


Figure 3.5: Boundary Effect near Dielectric slab and Tissue-Equivalent liquid Boundary

### 3.2.3 Boundary Effects

Electric field distortion due to coupling effects when the probe is in the closest vicinity of media boundary is referred to as a boundary effect and results in an overestimation of the actual field value [21]. The boundary effect can be reduced by advanced data evaluation if field polarization, probe orientation and distance from the boundary are known.

There is a tradeoff between increased distance to reduce the boundary effects and the resulting possible increase in extrapolation error, Figure 3.5.

Boundary effects are evaluated with the liquid-filled open waveguide setups used for probe calibration. Numerical compensation of the boundary effect is evaluated by comparing the probe output near the boundary with the analytical field.

### 3.2.4 Uncertainty Analysis

Uncertainty is the dispersion to be expected for a particular measurement. This knowledge is important when making decisions based on measurement data. Furthermore, it is a very important parameter for comparing measurement results, within a laboratory, between laboratories, and over time. Without an expression of uncertainty, it is impossible to judge whether two results are in compliance or not [22]. Uncertainty analysis is a method to quantify  $u_x$ , Equation (3.10)

$$x = \bar{x} \pm u_x \quad (3.9)$$

$$u_x = k\sigma_x \quad (3.10)$$

where  $x$  is the measured value,  $\bar{x}$  is the best estimate of the parameter (the sample average),  $\sigma_x$  is the standard deviation of the sample average, and  $k\sigma_x$  is the uncertainty interval.

Uncertainties for confidence levels ranging from 0.80 to 0.99, based on the normal distribution, are given in Table 3.1.

Table 3.1: Uncertainty as a Function of Confidence Level for Normally Distributed Errors

k	Uncertainty	Confidence Level
1.28	$1.28\sigma_x$	0.80
1.64	$1.64\sigma_x$	0.90
1.96	$1.96\sigma_x$	0.95
2.58	$2.58\sigma_x$	0.99

The assumption made above in the calculation of uncertainty is that the errors are normally distributed. For finite samples this is not strictly correct and uncertainties should actually be estimated using the t-distribution. The t-distribution is more spread out than the normal distribution and hence the uncertainties based on it are larger.

The combined standard uncertainty  $u_c$  is computed from the Root Sum Square (RSS) of the standard uncertainties of the individual components, Equation (3.11)

$$u_c = \sqrt{\sum_{i=1}^m c_i^2 u_i^2} \quad (3.11)$$

$$c_i = \frac{\partial f(x_1, \dots, x_m)}{\partial x_i} \frac{x_i}{f(x_i)} \quad (3.12)$$

where  $c_i$  is the sensitivity coefficient of each uncertainty component  $u_i$ , and  $m$  is the number of influence quantities.

Precision is the ability to produce the same value within given accuracy bounds when successive readings of a specific quantity are measured. Precision represents the maximum departure of all readings from the mean value of the readings.

All experimental uncertainty is due to either random errors or systematic errors. Random errors (precision error) are statistical fluctuations (in either direction) in the measured data due to the precision limitations of the measurement device. Precision errors usually result from the experimenter's inability to take the same measurement in exactly the same way to get exactly the same number. Systematic errors (bias errors), by contrast, are reproducible inaccuracies that are consistently in the same direction. Systematic errors are often due to a problem which persists throughout the entire experiment.

The precision errors,  $\varepsilon$ , are random errors and will have different values for each measurement. When repeated measurements are made for fixed test conditions, precision errors are observed as the scatter of the data. Precision errors are due to limitations on repeatability of the measurement system and to facility and environmental effects. Precision errors are estimated using statistical analysis, i.e., are assumed proportional to the standard deviation of a sample of  $N$  measurements of a variable,  $X$ . The uncertainty estimate of  $\varepsilon$  is called the precision limit,  $P$ . Precision errors can be reduced by averaging.

Bias errors,  $\beta$ , are difficult to detect and cannot be analyzed statistically, because all of the data is off in the same direction (either too high or too low). Spotting and correcting for bias errors takes a lot of care. Bias errors can be studied through intercomparisons, calibrations, and error propagation. The uncertainty estimate for  $\beta$  is called the bias limit,  $B$ .

Figure 3.6 shows the total error,  $\delta$ , which is composed of two components: bias error,  $\beta$ , and precision error,  $\varepsilon$ . The effects of such errors on multiple readings of a variable,  $X$ , are

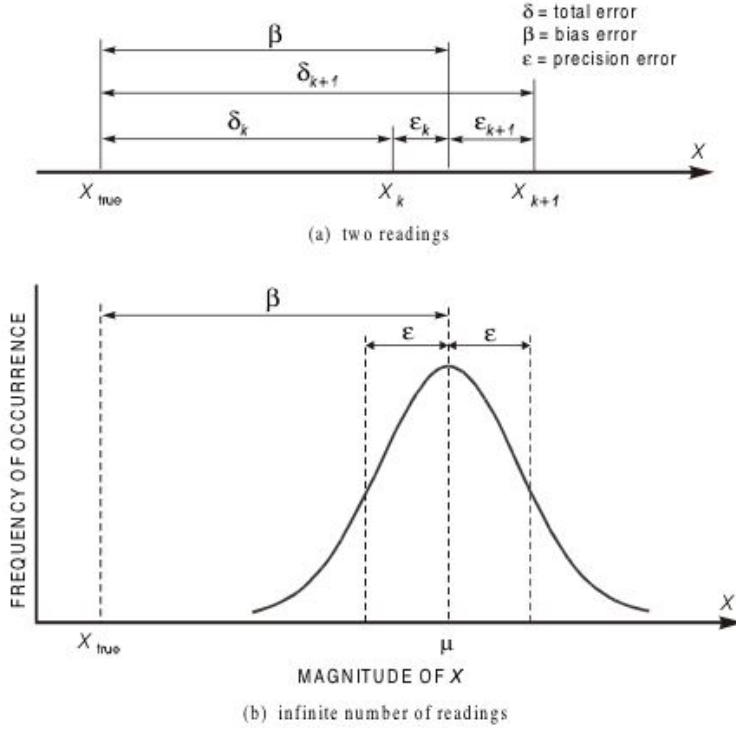


Figure 3.6: Errors in the measurement of a variable  $X$

also shown. If multiple measurements of some variable is taken, the bias error gives the difference between the mean (average) value of the readings,  $\mu$ , and the true value of that variable.

Measurement systems consist of the instrumentation, the procedures for data acquisition and reduction, and the operational environment. Measurements are made of individual variables,  $X_i$ , to obtain a result,  $r$ , which is calculated by combining the data for various individual variables through data reduction equations, Equation (3.13)

$$r = r(X_1, X_2, X_3, \dots, X_j) \tag{3.13}$$

Each of the measurement systems used to measure the value of an individual variable,  $X_i$ , is influenced by various elemental error sources. The effects of these elemental errors are manifested as bias errors (estimated by  $B_i$ ) and precision errors (estimated by  $P_i$ ) in the measured values of the variable,  $X_i$ . These errors in the measured values then propagate through the data reduction equation, thereby generating the bias,  $B_r$ , and precision,  $P_r$ ,

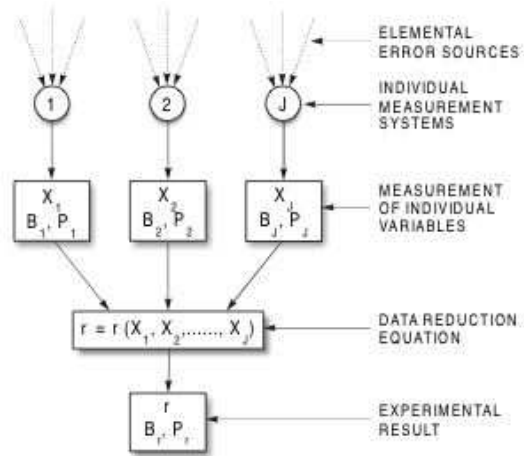


Figure 3.7: Propagation of errors into experimental results

errors in the experimental result,  $r$ . Figure 3.7 provides a block diagram showing elemental error sources, individual measurement systems, measurement of individual variables, data reduction equations, and experimental results.

## Chapter 4

# Calibration Measurements

The calibration process involves measuring the dielectric properties of a tissue-equivalent liquid in which an E-field probe is to be calibrated. The calculated dielectric parameters are then used in the theoretical formula, Equation (3.6), for the electric field inside the tissue-equivalent liquid used in probe calibration. Using a waveguide to calculate both the dielectric parameters and calibration factors has the advantage of eliminating a source of uncertainty involved when using a different experimental setup to calculate the dielectric properties.

### 4.1 Dielectric Property Measurements

E-field probes must be calibrated for different tissue-equivalent liquids they are used in, Equation (2.5). Therefore, it is difficult to measure the dielectric properties of a tissue-equivalent liquid without prior knowledge of the associated calibration factors for each orthogonal dipole. However, for the purpose of measuring the tissue-equivalent dielectric properties, the calibration factors can be consolidated into one calibration factor without loss of generality. The measured electric field, can be written as in Equation (4.1).

$$|E| = \sqrt{\frac{1}{K} (V_1 + V_2 + V_3)} = \sqrt{\frac{1}{K} (V_t)} \quad (4.1)$$

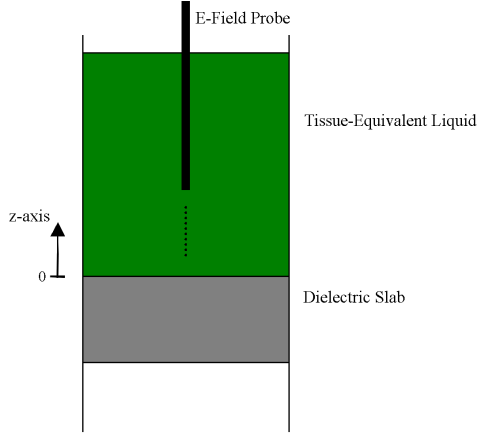


Figure 4.1: E-field probe scan along Waveguide z-axis

where  $V_t$  is the total measured voltage.

The real and imaginary permittivity of the tissue-equivalent liquid are calculated using the field attenuation factor inside the tissue-equivalent liquid and power reflectance at the air-dielectric slab interface.

#### 4.1.1 Attenuation factor

A scan along the waveguide z-axis is performed and the probe voltage is then measured as a function of net power and position in the liquid. Figure 4.1. The probe tip should not be close to media boundaries (less than one probe-tip diameter), to avoid field distortion due to coupling effects (boundary effect) [23, 24], or too far from dielectric slab boundary where the field has decayed significantly (skin-depth).

From the theoretical formula for the fundamental mode inside the waveguide, the electric field inside the tissue-equivalent liquid is given by Equation (4.2). The attenuation factor  $\alpha$ , is calculated using an exponential curve-fit, Equation (4.3)

$$\frac{V_t}{P_{net}} = Ae^{-z\alpha} \quad (4.2)$$

$$\alpha = \frac{\omega^2 \mu_0 \epsilon_0 \epsilon''}{\sqrt{\omega^2 \mu_0 \epsilon_0 \epsilon' - \left(\frac{\pi}{a}\right)^2}} \quad (4.3)$$

$$A = \frac{4\omega\mu_0}{ab2\beta} \sin\left(\frac{\pi}{a}x_0\right) e^{z_0\alpha} \quad (4.4)$$

where  $A$  is a constant,  $x_0$  is the location of the E-field probe along the x-axis,  $a$  and  $b$  are the cross-sectional dimensions of the waveguide, and  $z_0$  is the uncertainty in the E-field probe location along the z-axis ( $z \pm z_0$ ).

Since the fitting parameters are  $A$  and  $\alpha$ , and the uncertainties associated with probe position,  $x_0$  and  $z_0$ , are included in the magnitude  $A$ , the desired parameter  $\alpha$  is independent of positioning errors.

#### 4.1.2 Power Reflectance

Power reflectance at the air-dielectric slab interface, is calculated from the measured forward and reverse powers. The analytical formula for the power reflectance as a function of  $\epsilon'$  and  $\epsilon''$  at the air-dielectric slab interface is given by Equation (4.5)

$$10 \log_{10} \left( \frac{P_{rev}}{P_{for}} \right) = |\Gamma_1|^2 = \left| \frac{\rho_1 + \rho_2 e^{-2\beta_a d_a} + \rho_1 \rho_2 \rho_3 e^{-2\beta_s d_s} + \rho_3 e^{-2\beta_a d_a} e^{-2\beta_s d_s}}{1 + \rho_1 \rho_2 e^{-2\beta_a d_a} + \rho_2 \rho_3 e^{-2\beta_s d_s} + \rho_1 \rho_3 e^{-2\beta_a d_a} e^{-2\beta_s d_s}} \right|^2 \quad (4.5)$$

The real and imaginary parts of the permittivity,  $\epsilon'$  and  $\epsilon''$ , can be solved for numerically using Equation (4.3) and Equation (4.5). The conductivity,  $\sigma$  is calculated using Equation (4.6)

$$\sigma = \omega \epsilon_0 \epsilon'' \quad (4.6)$$

The steps required for calculating the dielectric parameters are:

- Position probe in waveguide center
- Measure E-field along the waveguide z-axis
- Calculate attenuation factor  $\alpha$  from exponential curve fit
- Calculate power reflectance  $|\Gamma|^2$  from power measurements
- Solve for real and imaginary permittivity  $\epsilon'$  and  $\epsilon''$  using measured  $\alpha$  and  $|\Gamma|^2$

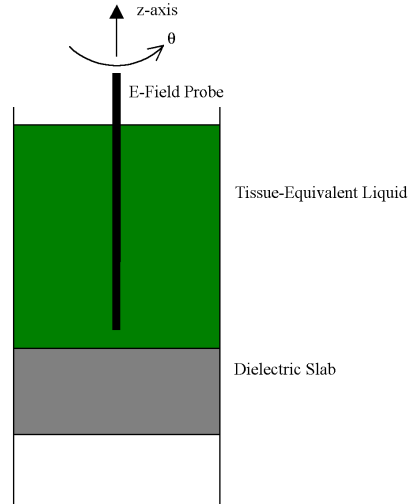


Figure 4.2: E-field probe isotropic scan about its axis inside the Waveguide

## 4.2 Calibration Factor Measurements

To calculate the calibration factors for each orthogonal dipole, the probe is rotated about its axis, Figure 4.2 (Figure A.6 Appendix A).

Using the data obtained from the probe isotropic scan, the calibration factors for each orthogonal dipole are obtained by fitting the measured data to the square magnitude of the total electric field inside the tissue-equivalent liquid, Equation (4.7). This method eliminates the need to calibrate each dipole individually.

$$\frac{1}{P_{net}} \left[ \frac{V_1}{k_1} + \frac{V_2}{k_2} + \frac{V_3}{k_3} \right] = \frac{4\omega\mu_0}{ab2\beta} \sin\left(\frac{\pi}{a}x_0\right) e^{z_0\alpha} \quad (4.7)$$

The steps required for calculating the calibration factors are:

- Measure dielectric properties using the steps outlined in the previous section
- Position probe in waveguide center
- Measure E-field by rotating the probe about its axis
- Calculate calibration factors  $k_1$ ,  $k_2$ , and  $k_3$  using linear curve fit

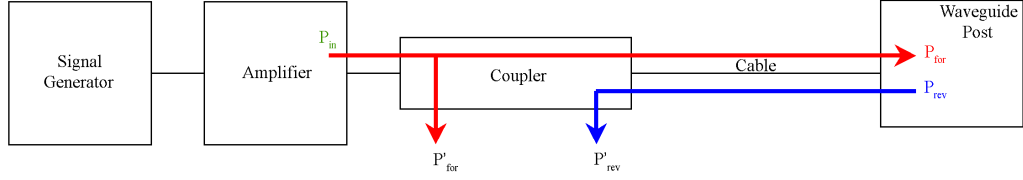


Figure 4.3: Net power calculation from forward and reverse power measurements

### 4.3 Net Power Measurements

Figure 4.3 shows the power flow to and from the waveguide. The input power from the signal generator is amplified and fed through a coupler to measure the foreword and reverse power.

To calculate the forward and reverse power inside the waveguide, the losses in the coupler and cable must be corrected for. Assuming that losses and coupling factors are measured in decibels (dB); the forward power must be corrected for forward coupler loss  $C_f$ , coupler insertion loss  $C_i$ , and cable loss  $L_b$ ; the reverse power must be corrected for reverse coupler loss  $C_r$ , and cable loss  $L_b$ , Equations (4.8-4.10)

$$P_{for} = P'_{for} - C_f + C_i + L_b \quad (4.8)$$

$$P_{rev} = P'_{rev} - C_r + L_b \quad (4.9)$$

$$P_{net} = P_{for} + P_{rev} \quad (4.10)$$

Conductor loss in the waveguide due to finite wall conductivity is ignored at 900MHz and 1800MHz. The conductor losses for an aluminum waveguide is in the order of a hundredth of a dB.

### 4.4 Calibration Procedure Overview

The calibration process is performed as follows:

1. Operate in the square-law region
2. Avoid placing probe near boundaries
3. Calculate dielectric properties
4. Calculate probe calibration factors

## Chapter 5

# Results and Analysis

The calibration system is tested using Saline, a standard salt and water solution, and used to measure the dielectric properties of tissue-equivalent liquids and calibrate an E-field probe at 900MHz and 1800MHz. The waveguides used are described in Table 5.1. For 900MHz the WR975 waveguide is used, and for 1800MHz the WR430 waveguide is used.

Table 5.1: Waveguide specifications at 900MHz and 1800MHz

	WR975 (900MHz)	WR430 (1800MHz)
Waveguide internal width $a$ in mm	247.650	109.220
Waveguide internal height $b$ in mm	123.825	54.610
Frequency range in GHz	0.75-1.12	1.70-2.60

### 5.1 Validation

A series of tests are performed to determine the complex permittivity of saline solutions. Table 5.2 shows the results for 900MHz and Table 5.3 shows the results for 1800MHz. These results were compared to measurements made with a HP 85070C Dielectric Probe Measurement System. Using the waveguide system, the measurement uncertainties are  $\pm 2\%$  and  $\pm 1\%$  for  $\epsilon'$  and  $\epsilon''$ , respectively. The HP probe measurement system states an uncertainty of  $\pm 5\%$  for both  $\epsilon'$  and  $\epsilon''$ .

Table 5.2: Saline Dielectric Properties measured at 900MHz

	Waveguide		HP Probe	
	$\epsilon'$	$\epsilon''$	$\epsilon'$	$\epsilon''$
0.3 Salinity	$78.7 \pm 2 \%$	$16.3 \pm 1 \%$	$77.0 \pm 5 \%$	$17.0 \pm 5 \%$
0.5 Salinity	$78.3 \pm 2 \%$	$24.3 \pm 1 \%$	$77.0 \pm 5 \%$	$24.0 \pm 5 \%$
0.7 Salinity	$76.5 \pm 2 \%$	$31.1 \pm 1 \%$	$77.0 \pm 5 \%$	$30.0 \pm 5 \%$

Table 5.3: Saline Dielectric Properties measured at 1800MHz

	Waveguide		HP Probe	
	$\epsilon'$	$\epsilon''$	$\epsilon'$	$\epsilon''$
0.3 Salinity	$77.4 \pm 2 \%$	$13.6 \pm 1 \%$	$78.0 \pm 5 \%$	$13.0 \pm 5 \%$
0.5 Salinity	$77.5 \pm 2 \%$	$15.9 \pm 1 \%$	$77.0 \pm 5 \%$	$17.0 \pm 5 \%$
0.7 Salinity	$76.9 \pm 2 \%$	$20.0 \pm 1 \%$	$76.0 \pm 5 \%$	$21.0 \pm 5 \%$

A saline solution at 0.5 salinity is 0.5% NaCl (salt) and 99.5% water. Another way of expressing concentration is called molarity. Molarity is the number of moles of solute dissolved in one liter of solution. Saline solutions of known molarity are often used for the calibration of dielectric measurement apparatus. This is particularly so when the "open-probe" technique is used. For many years equations given by Stogryn [25] have been widely used to calculate the dielectric properties of such saline solutions. Davis [26] discovered errors in Stogryn's equations when making measurements on saline solutions of high molarity, especially with regard to calculation of the imaginary part of their dielectric constant. The measured dielectric properties of saline solutions using the waveguide system, to the best of the authors knowledge, are the most accurate yet.

## 5.2 Results

Since the probe calibration factors depend on the tissue-equivalent liquid being used, the dielectric properties must be measured first.

### 5.2.1 Dielectric Properties Measurement

Tissue-equivalent liquids at 900MHz and 1800MHz are measured. To insure repeatability of the measurement system, repeated measurements are performed using the same tissue-

equivalent liquid at 900MHz Table 5.4. At 1800MHz different measurements were performed for different tissue-equivalent liquids Table 5.5. Again the results are compared with the HP 85070C Dielectric Probe Measurement System. Using the waveguide system, the measurement uncertainties are  $\pm 2\%$  and  $\pm 1\%$  for  $\epsilon'$  and  $\epsilon''$ , respectively. The HP probe measurement system states an uncertainty of  $\pm 5\%$  for both  $\epsilon'$  and  $\epsilon''$ .

Table 5.4: Tissue-Equivalent Liquid Dielectric Properties measured at 900MHz

	Waveguide		HP Probe	
	$\epsilon'$	$\epsilon''$	$\epsilon'$	$\epsilon''$
Measurement 1	$40.62 \pm 2 \%$	$19.00 \pm 1 \%$	$40.26 \pm 5 \%$	$19.88 \pm 5 \%$
Measurement 2	$40.57 \pm 2 \%$	$19.12 \pm 1 \%$	$40.26 \pm 5 \%$	$19.88 \pm 5 \%$
Measurement 3	$40.26 \pm 2 \%$	$19.09 \pm 1 \%$	$40.26 \pm 5 \%$	$19.88 \pm 5 \%$

Table 5.5: Tissue-Equivalent Liquid Dielectric Properties measured at 1800MHz

	Waveguide		HP Probe	
	$\epsilon'$	$\epsilon''$	$\epsilon'$	$\epsilon''$
Liquid 1	$39.86 \pm 2 \%$	$13.59 \pm 1 \%$	$39.88 \pm 5 \%$	$13.56 \pm 5 \%$
Liquid 2	$39.47 \pm 2 \%$	$13.56 \pm 1 \%$	$39.43 \pm 5 \%$	$13.66 \pm 5 \%$
Liquid 3	$40.95 \pm 2 \%$	$13.64 \pm 1 \%$	$40.54 \pm 5 \%$	$14.01 \pm 5 \%$

Sample traces of a normalized electric field magnitude-squared recorded at the center column of the waveguide at 1800MHz and power reflectance versus input power at 900MHz are shown in Figures 5.1-5.2

### 5.2.2 Calibration Factors Measurement

Calibration factors for each orthogonal dipole are obtained from isotropic scans. The results for calibration factors at 900MHz and 1800MHz are shown in Table 5.6 and Table 5.7. The calibration factors are measured at different power levels. Figure 5.3 shows field isotopicity at 1800MHz. Using the waveguide system, the measurement uncertainties is  $\pm 1\%$  for all the calibration factors.

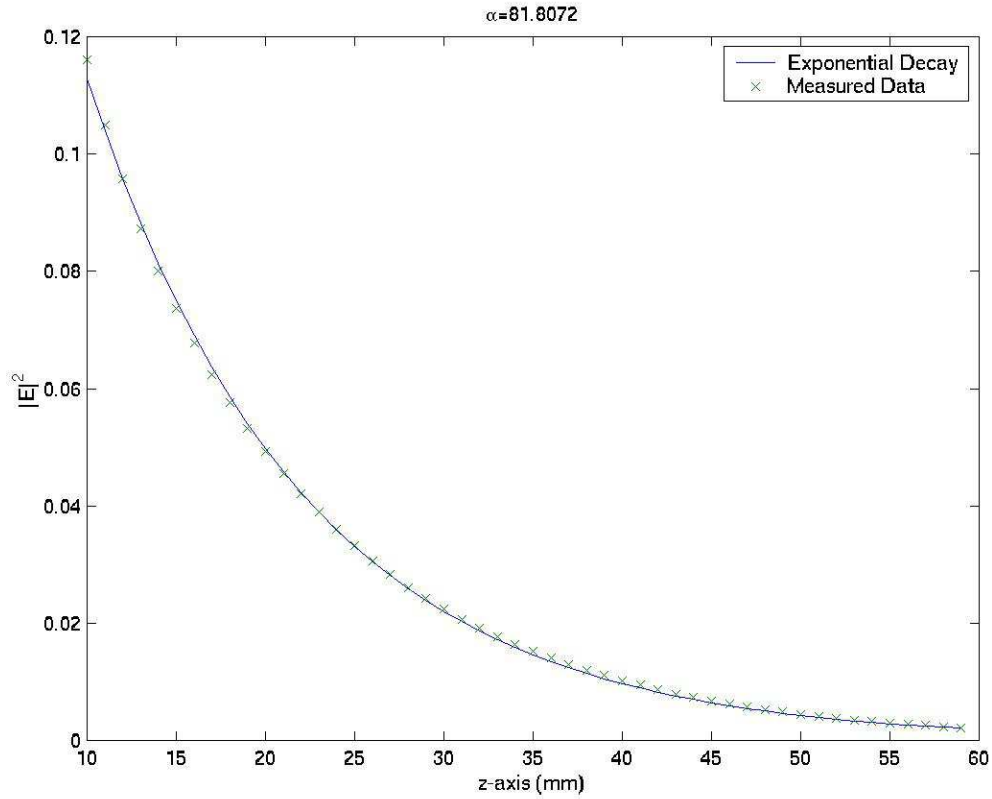


Figure 5.1: Normalized  $|E|^2$  attenuation inside 1800MHz waveguide  $\epsilon' = 39.86$   $\epsilon'' = 13.59$

### 5.3 Uncertainty Analysis

The reported uncertainties are calculated from the curve-fitting procedures and the tolerances of the instrumentation used. Since the dielectric properties are measured first, the uncertainties associated with the calibration factors also depend on the uncertainties obtained from the dielectric properties measurement.

Table 5.6: Calibration Factors measured at 900MHz  $\epsilon' = 40.26$   $\epsilon'' = 20.88$   $z = 22.7mm$

	31.90 mW	103.11 mW	327.70 mW
Dipole 1 ( $mV/(V/m)^2$ )	$8.90 \pm 1 \%$	$8.93 \pm 1 \%$	$8.77 \pm 1 \%$
Dipole 2 ( $mV/(V/m)^2$ )	$8.53 \pm 1 \%$	$8.59 \pm 1 \%$	$8.49 \pm 1 \%$
Dipole 3 ( $mV/(V/m)^2$ )	$9.32 \pm 1 \%$	$9.28 \pm 1 \%$	$9.11 \pm 1 \%$

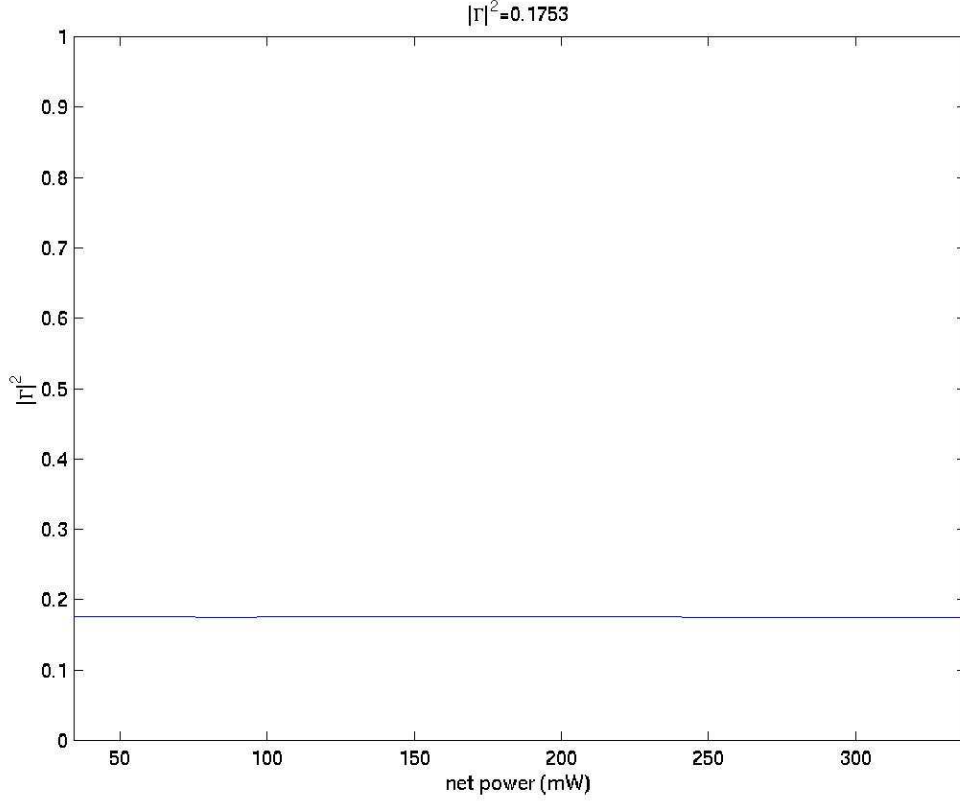


Figure 5.2: Power Reflectance at the air-acrylic boundary for 900MHz waveguide  $\epsilon' = 40.62$   
 $\epsilon'' = 19.00$

### 5.3.1 Dielectric Properties Uncertainties

The dielectric parameters  $\epsilon'$  and  $\epsilon''$  are solved-for using the expressions for the measured attenuation factor  $\alpha$  and power reflectance  $|\Gamma|^2$

$$\alpha = \frac{\omega^2 \mu_0 \epsilon_0 \epsilon''}{\sqrt{\omega^2 \mu_0 \epsilon_0 \epsilon' - \left(\frac{\pi}{a}\right)^2}} \quad (5.1)$$

$$|\Gamma_1|^2 = \left| \frac{\rho_1 + \rho_2 e^{-2\beta_a d_a} + \rho_1 \rho_2 \rho_3 e^{-2\beta_s d_s} + \rho_3 e^{-2\beta_a d_a} e^{-2\beta_s d_s}}{1 + \rho_1 \rho_2 e^{-2\beta_a d_a} + \rho_2 \rho_3 e^{-2\beta_s d_s} + \rho_1 \rho_3 e^{-2\beta_a d_a} e^{-2\beta_s d_s}} \right|^2 \quad (5.2)$$

Table 5.7: Calibration Factors measured at 1800MHz  $\epsilon' = 39.17$   $\epsilon'' = 14.69$   $z = 22.7mm$

	11.01 mW	35.31 mW	113.14 mW
Dipole 1 ( $mV/(V/m)^2$ )	$9.31 \pm 1 \%$	$9.25 \pm 1 \%$	$9.20 \pm 1 \%$
Dipole 2 ( $mV/(V/m)^2$ )	$9.10 \pm 1 \%$	$8.90 \pm 1 \%$	$8.92 \pm 1 \%$
Dipole 3 ( $mV/(V/m)^2$ )	$9.94 \pm 1 \%$	$9.63 \pm 1 \%$	$9.61 \pm 1 \%$

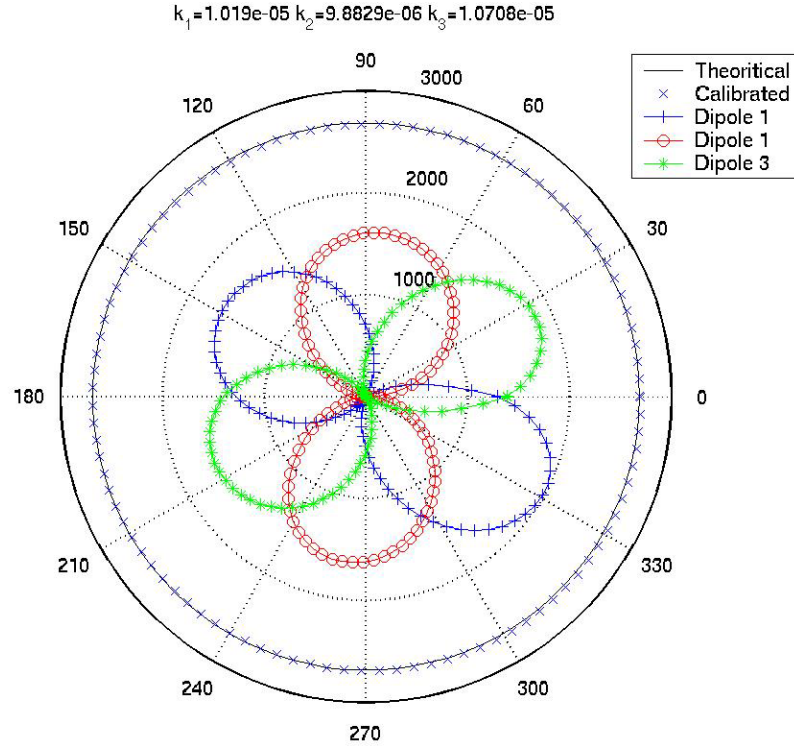


Figure 5.3: Probe isotropy measured at 1800MHz ( $\epsilon' = 39.17$   $\epsilon'' = 14.69$   $z = 22.7mm$ )

The uncertainties are calculated using Monte Carlo simulation. Random scatter are added from a Gaussian distribution with a mean of zero and a standard deviation calculated from variable uncertainties. The algorithm is as follows:

```

calculate attenuation factor  $\alpha$ 
calculate power reflectance  $|\Gamma|^2$ 
solve for dielectric parameters  $\epsilon'$  and  $\epsilon''$ 

for i = 1 to 1000
    add random scatter to operating frequency  $f$ 
    add random scatter to waveguide dimension  $a$ 
    add random scatter to power reflectance  $|\Gamma|^2$ 
    add random scatter to attenuation factor  $\alpha$ 

```

```

add random scatter to dielectric slab permittivity
solve for dielectric parameters  $\epsilon'$  and  $\epsilon''$ 
end

find confidence interval within 2.5 and 97.5 percentiles
for each parameter,  $\epsilon'$  and  $\epsilon''$ 

```

Using Monte Carlo simulation, the sensitivities at 900MHz in tissue-equivalent permittivity to power reflectance  $|\Gamma|^2$ , frequency  $f$ , waveguide dimension  $a$ , attenuation factor  $\alpha$ , and slab permittivity are calculated and are shown in Figures 5.4-5.8. The dielectric properties are sensitive to variations in dielectric slab permittivity. Therefore, accurate measurements of the dielectric slab used must be performed to insure the accuracy of the measured dielectric properties of tissue-equivalent liquids.

### 5.3.2 Calibration Factors Uncertainties

The calibration factors are obtained by fitting the measured data to the theoretical square magnitude of the total electric field inside the tissue-equivalent liquid

$$\frac{1}{P_{net}} \begin{bmatrix} V_{11} & V_{21} & V_{31} \\ \vdots & \vdots & \vdots \\ V_{1n} & V_{2n} & V_{3n} \end{bmatrix} \begin{bmatrix} \frac{1}{k_1} \\ \frac{1}{k_2} \\ \frac{1}{k_3} \end{bmatrix} = \begin{bmatrix} \frac{4\omega\mu_0}{ab2\beta} \sin\left(\frac{\pi}{a}x_0\right) e^{-z_{01}\alpha} \\ \vdots \\ \frac{4\omega\mu_0}{ab2\beta} \sin\left(\frac{\pi}{a}x_0\right) e^{-z_{0n}\alpha} \end{bmatrix} \quad (5.3)$$

The uncertainties are calculated using Monte Carlo simulation. Random scatter are added from a Gaussian distribution with a mean of zero and a standard deviation calculated from variable uncertainties. The algorithm is as follows:

```

set dielectric parameters  $\epsilon'$  and  $\epsilon''$ 
calculate calibration factors  $k_1$ ,  $k_2$ , and  $k_3$ 

```

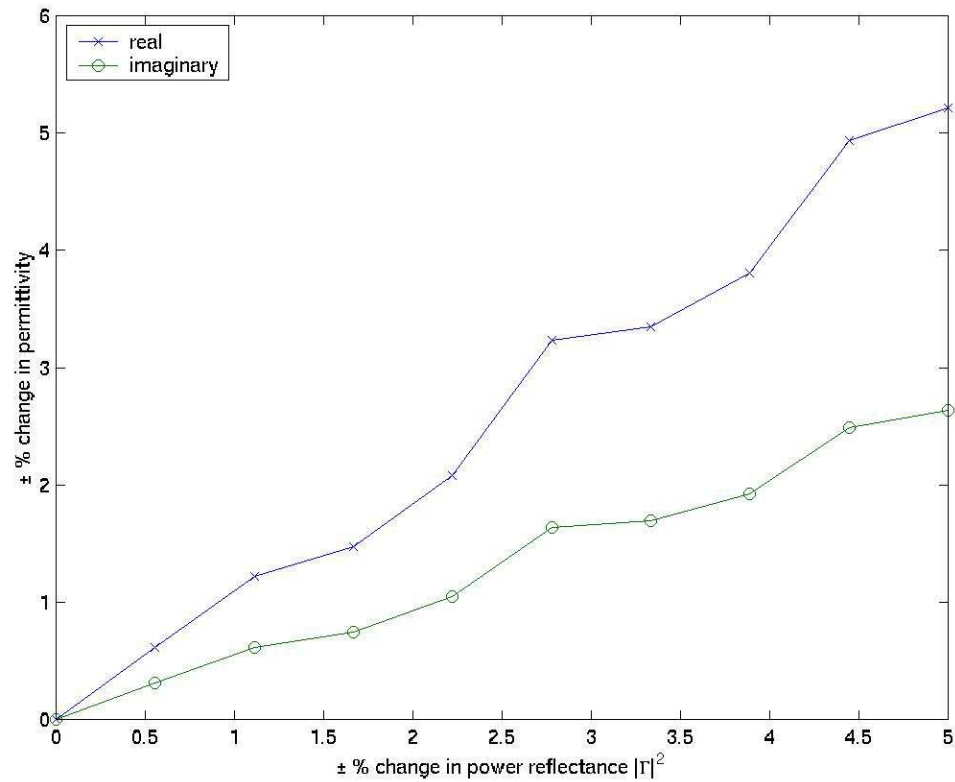


Figure 5.4: Change in complex permittivity due to change in power reflectance  $|\Gamma|^2$  ( $\epsilon' = 40.62$   $\epsilon'' = 19.00$ )

```

for i = 1 to 1000
    add random scatter to operating frequency  $f$ 
    add random scatter to waveguide dimension  $a$ 
    add random scatter to dielectric parameters  $\epsilon'$  and  $\epsilon''$ 
    calculate calibration factors  $k_1$ ,  $k_2$ , and  $k_3$ 
end

find confidence interval within 2.5 and 97.5 percentiles
for each parameter,  $k_1$ ,  $k_2$ , and  $k_3$ 

```

From Equation (5.3) the calibration factors  $k_1$ ,  $k_2$ , and  $k_3$  are inversely proportional to the

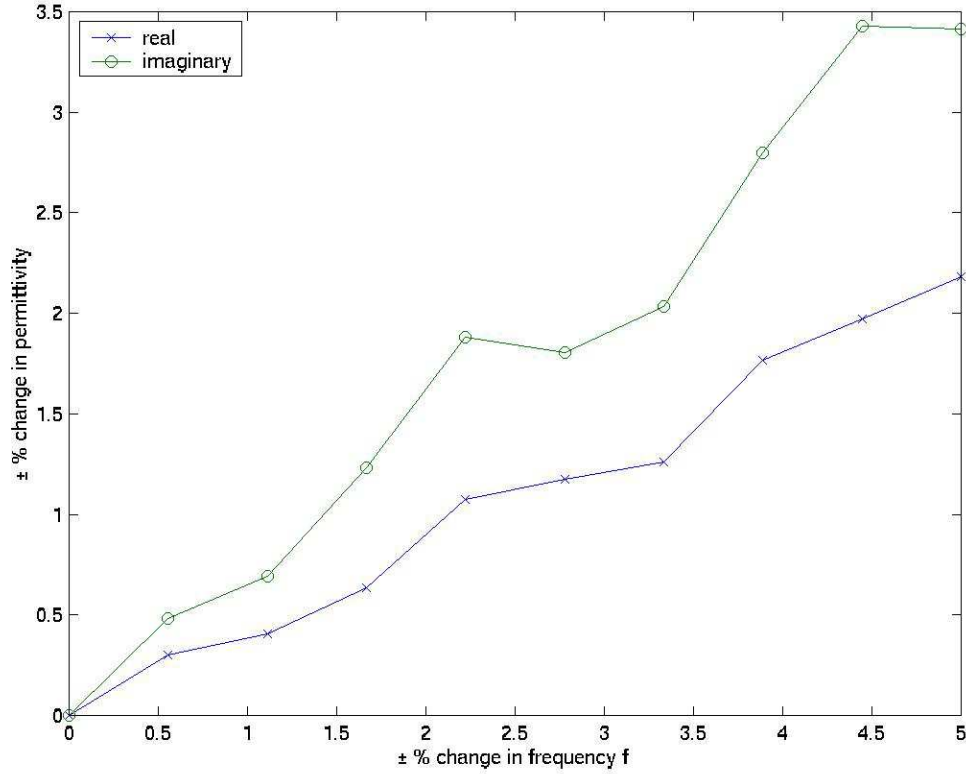


Figure 5.5: Change in complex permittivity due to change in frequency  $f$  ( $\epsilon' = 40.62$ ,  $\epsilon'' = 19.00$ )

electric field magnitude squared  $|E|^2$ . And since any changes in electric field magnitude will affect all calibration factors equally, Equation (4.1) can be used to calculate the uncertainties in the calibration factors

$$K = \frac{V_t}{|E|^2} \quad (5.4)$$

where  $V_t$  is the total measured voltage, and  $K$  is the consolidated calibration factor.

The uncertainty in  $K$  due to changes in the electric field magnitude squared  $|E|^2$  [22] is

$$\left(\frac{\Delta K}{K}\right)^2 = \left(UMF_{|E|^2} \frac{\Delta |E|^2}{|E|^2}\right)^2 \quad (5.5)$$

where the  $UMF_{|E|^2}$  is the uncertainty magnification factor related to  $|E|^2$  and is given by

$$UMF_{|E|^2} = \frac{\partial K}{\partial |E|^2} \frac{|E|^2}{K} = -1 \quad (5.6)$$

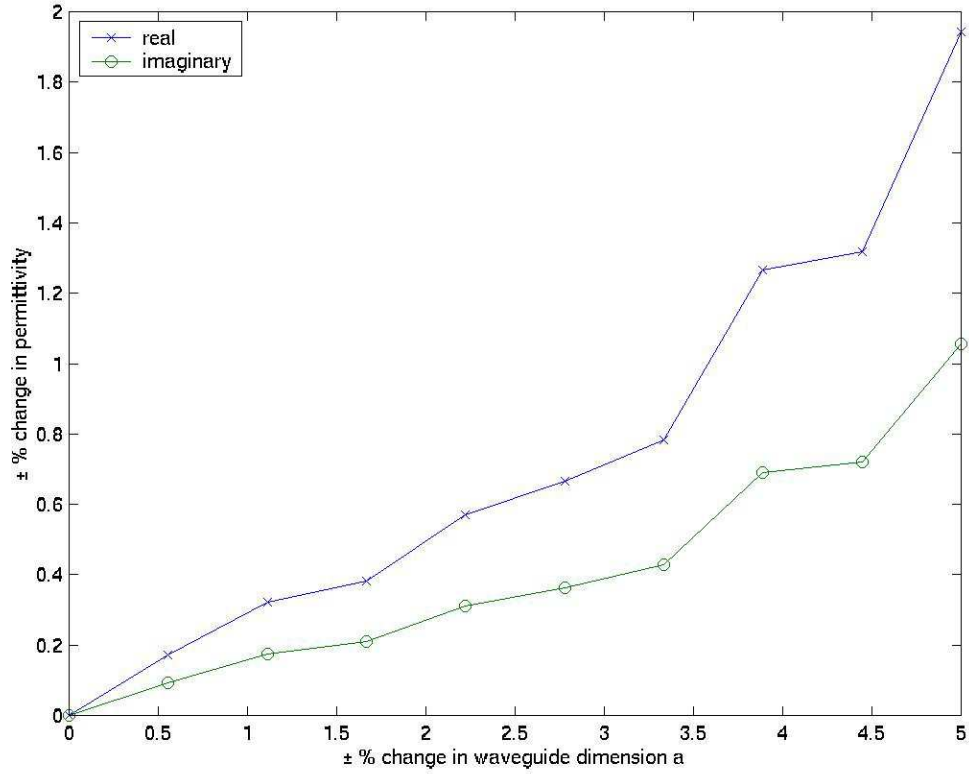


Figure 5.6: Change in complex permittivity due to change in waveguide dimension  $a$  ( $\epsilon' = 40.62$   $\epsilon'' = 19.00$ )

Therefore, the uncertainty in  $K$  is given by

$$\left(\frac{\Delta K}{K}\right)^2 = \left(-1 \frac{\Delta|E|^2}{|E|^2}\right)^2 \quad (5.7)$$

Electric field sensitivity,  $|E|^2$ , due to angular frequency  $w$ , waveguide dimension  $a$ , real permittivity  $\epsilon'$ , and imaginary permittivity  $\epsilon''$  is

$$\left(\frac{\Delta|E|^2}{|E|^2}\right)^2 = \left(UMF_w \frac{\Delta w}{w}\right)^2 + \left(UMF_a \frac{\Delta a}{a}\right)^2 + \left(UMF_{\epsilon'} \frac{\Delta \epsilon'}{\epsilon'}\right)^2 + \left(UMF_{\epsilon''} \frac{\Delta \epsilon''}{\epsilon''}\right)^2 \quad (5.8)$$

where the  $UMFs$  are the uncertainty magnification factors and are given by

$$UMF_w = \frac{\partial|E|^2}{\partial w} \frac{w}{|E|^2} \quad (5.9)$$

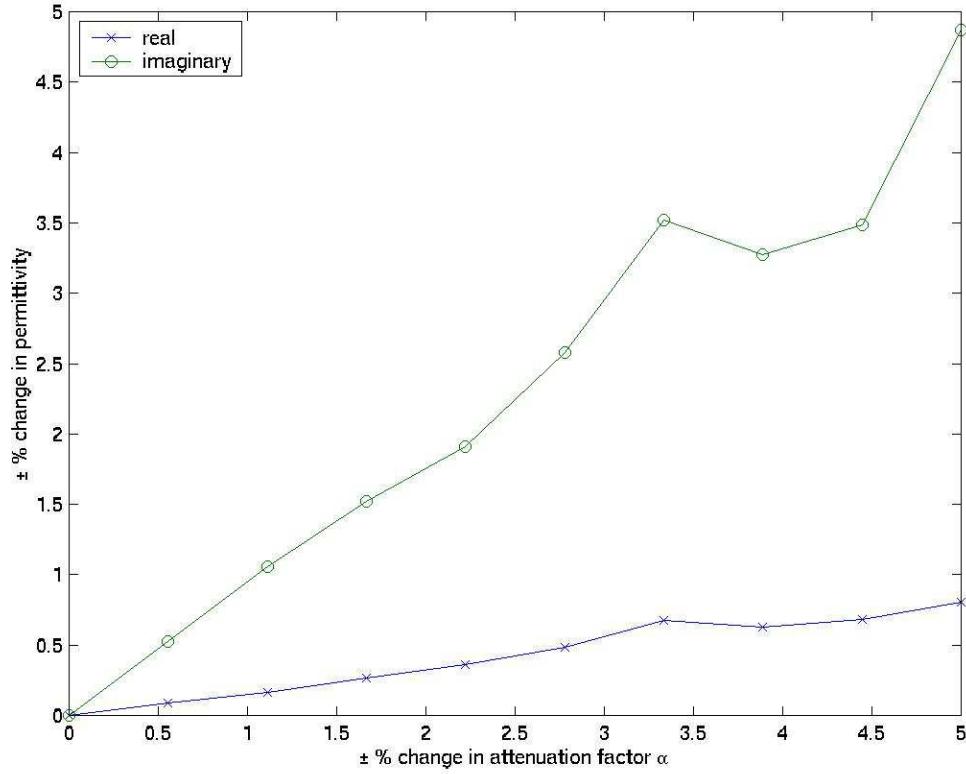


Figure 5.7: Change in complex permittivity due to change in attenuation factor  $\alpha$  ( $\epsilon' = 40.62$ ,  $\epsilon'' = 19.00$ )

$$UMF_a = \frac{\partial |E|^2}{\partial a} \frac{a}{|E|^2} \quad (5.10)$$

$$UMF_{\epsilon'} = \frac{\partial |E|^2}{\partial \epsilon'} \frac{\epsilon'}{|E|^2} \quad (5.11)$$

$$UMF_{\epsilon''} = \frac{\partial |E|^2}{\partial \epsilon''} \frac{\epsilon''}{|E|^2} \quad (5.12)$$

Evaluating the partial derivatives leads to

$$\frac{\partial |E|^2}{\partial w} \frac{w}{|E|^2} = -\frac{\pi^2 \beta + zw\mu_0\sigma (a^2 w^2 \mu_0 \epsilon_0 \epsilon' - 2\pi^2)}{a^2 \beta^3} \quad (5.13)$$

$$\frac{\partial |E|^2}{\partial a} \frac{a}{|E|^2} = w^2 \mu_0 \epsilon_0 a^2 \frac{-w^2 \mu_0 \epsilon_0 a^2 \epsilon'^2 + \pi^2 (\epsilon' + \epsilon'' z \beta)}{(a\beta)^4} \quad (5.14)$$

$$\frac{\partial |E|^2}{\partial \epsilon'} \frac{\epsilon'}{|E|^2} = \frac{1}{2} w^2 \mu_0 \epsilon_0 a^2 \epsilon' \frac{-w^2 \mu_0 \epsilon_0 a^2 \epsilon' + \pi^2 + w\mu_0 a^2 z \sigma \beta}{(a\beta)^4} \quad (5.15)$$

$$\frac{\partial |E|^2}{\partial \epsilon''} \frac{\epsilon''}{|E|^2} = -z \frac{w\mu_0\sigma}{\beta} \quad (5.16)$$

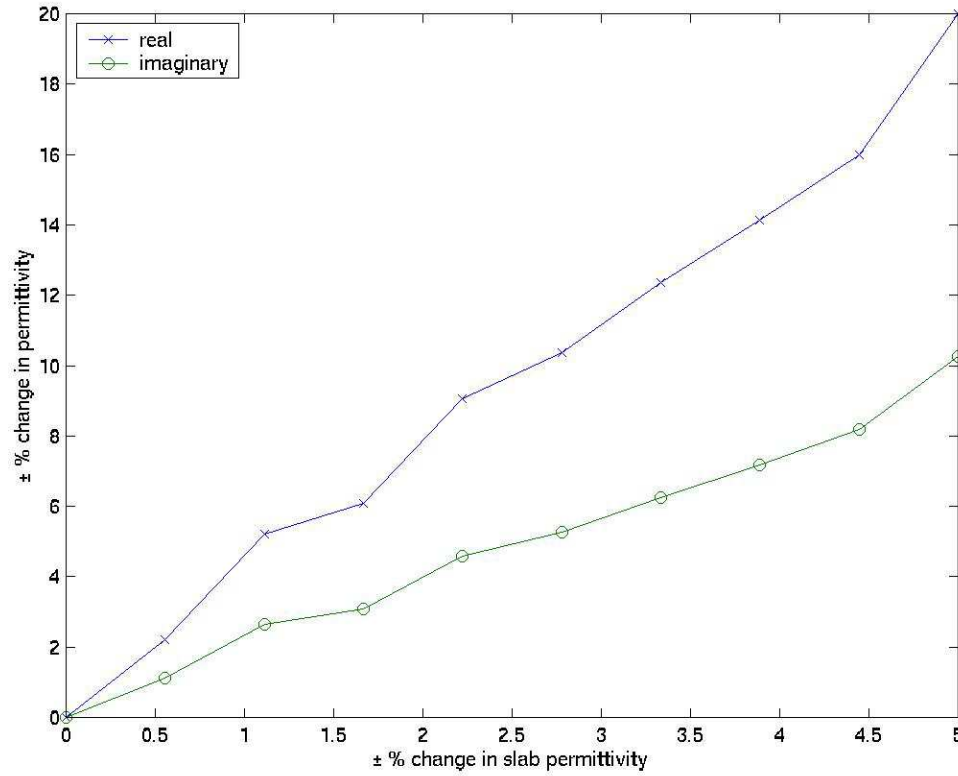


Figure 5.8: Change in complex permittivity due to change in slab permittivity ( $\epsilon' = 40.62$ ,  $\epsilon'' = 19.00$ )

Therefore, the uncertainty in  $|E|^2$  not only depends on the uncertainties in  $w$ ,  $a$ ,  $\epsilon'$ ,  $\epsilon''$ , and slab permittivity, but also on the value of the parameters themselves. Thus, the uncertainties in  $|E|^2$  will vary with operating conditions even if the uncertainties are all constants. The sensitivities at 1800MHz, for  $z = 15mm$ , in tissue-equivalent permittivity to real permittivity  $\epsilon'$ , imaginary permittivity  $\epsilon''$ , angular frequency  $w$ , and waveguide dimension  $a$  are shown in Figures 5.9-5.12.

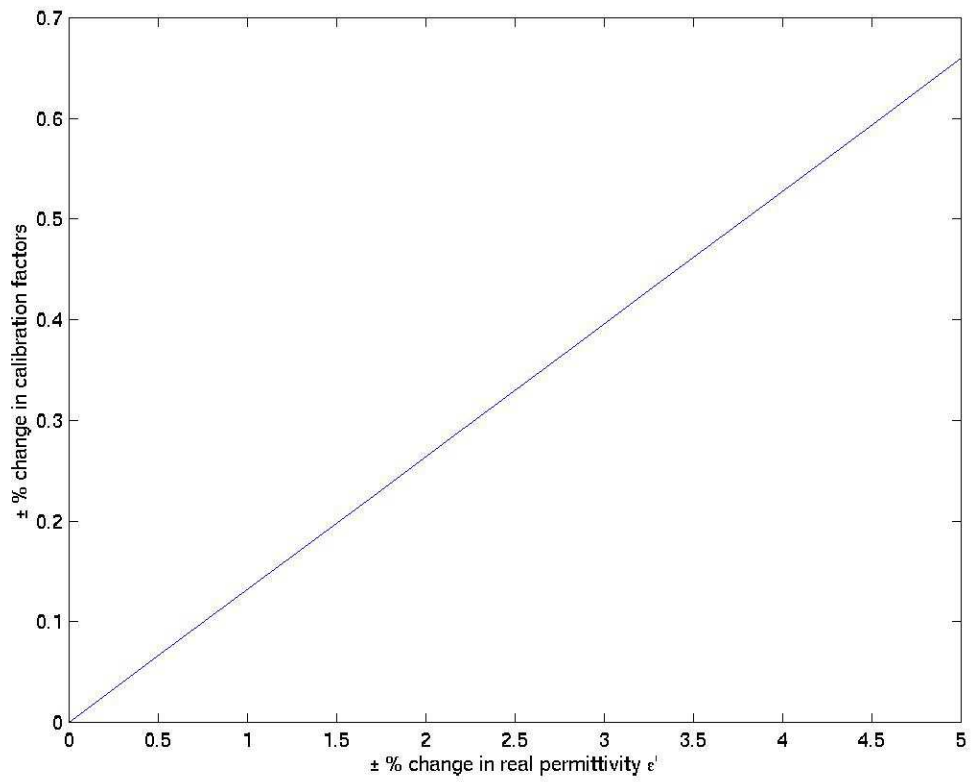


Figure 5.9: Change in calibration factors due to change in real permittivity  $\epsilon'$  ( $\epsilon' = 40.00$   
 $\epsilon'' = 13.98$   $z = 15mm$ )

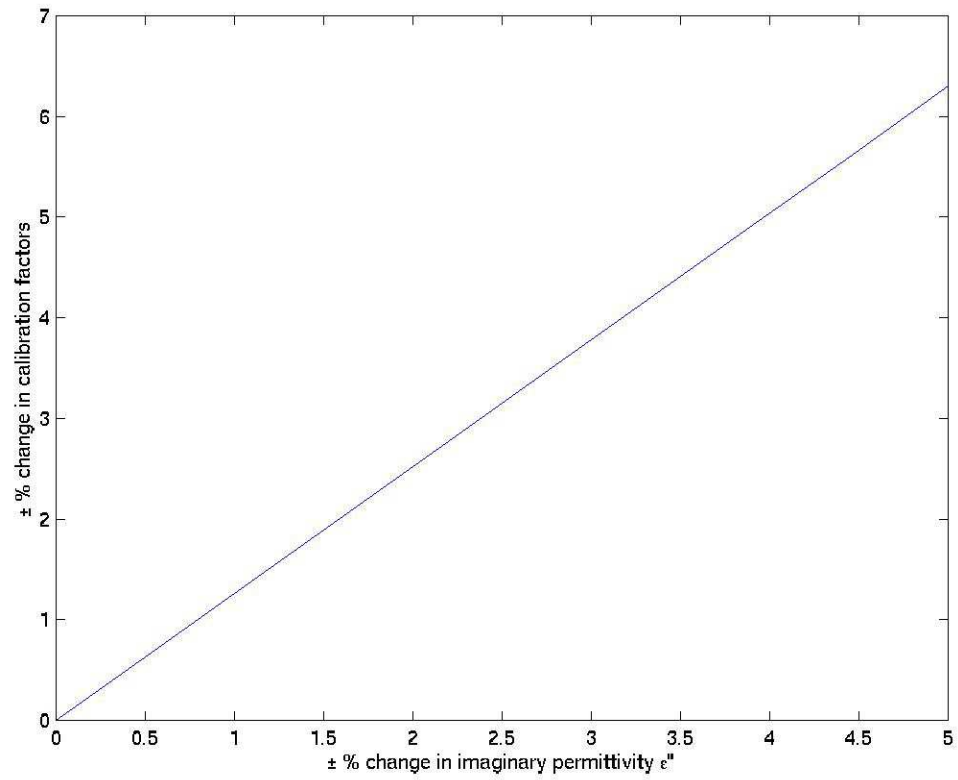


Figure 5.10: Change in calibration factors due to change in imaginary permittivity  $\epsilon''$   
 ( $\epsilon' = 40.00$   $\epsilon'' = 13.98$   $z = 15mm$ )

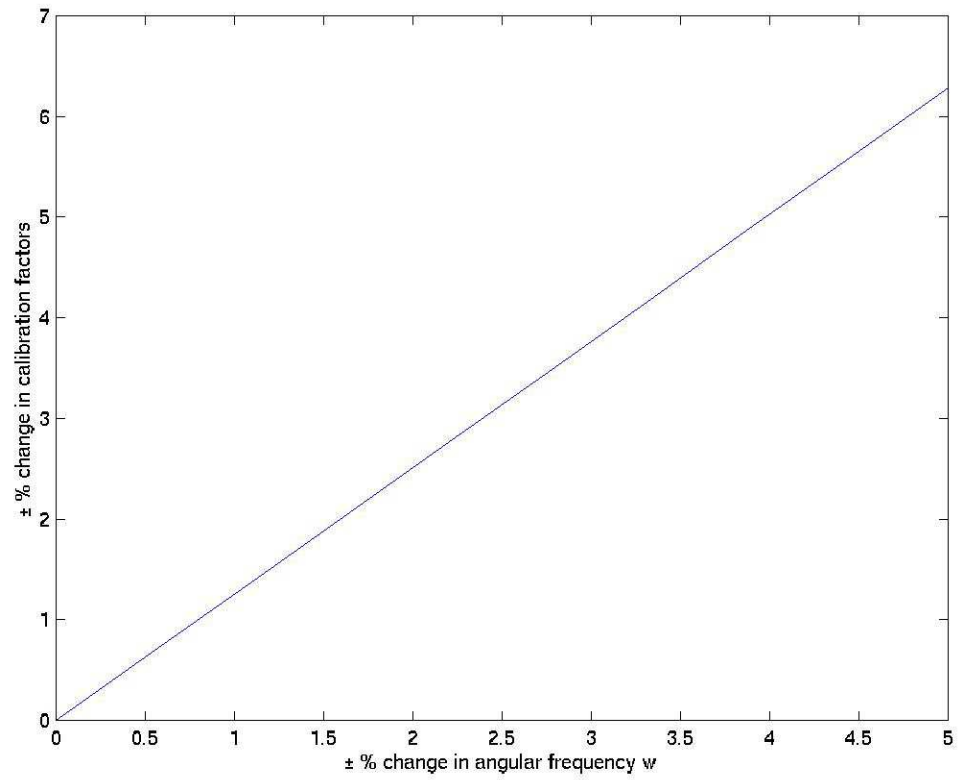


Figure 5.11: Change in calibration factors due to change in angular frequency  $w$  ( $\epsilon' = 40.00$   
 $\epsilon'' = 13.98$   $z = 15mm$ )

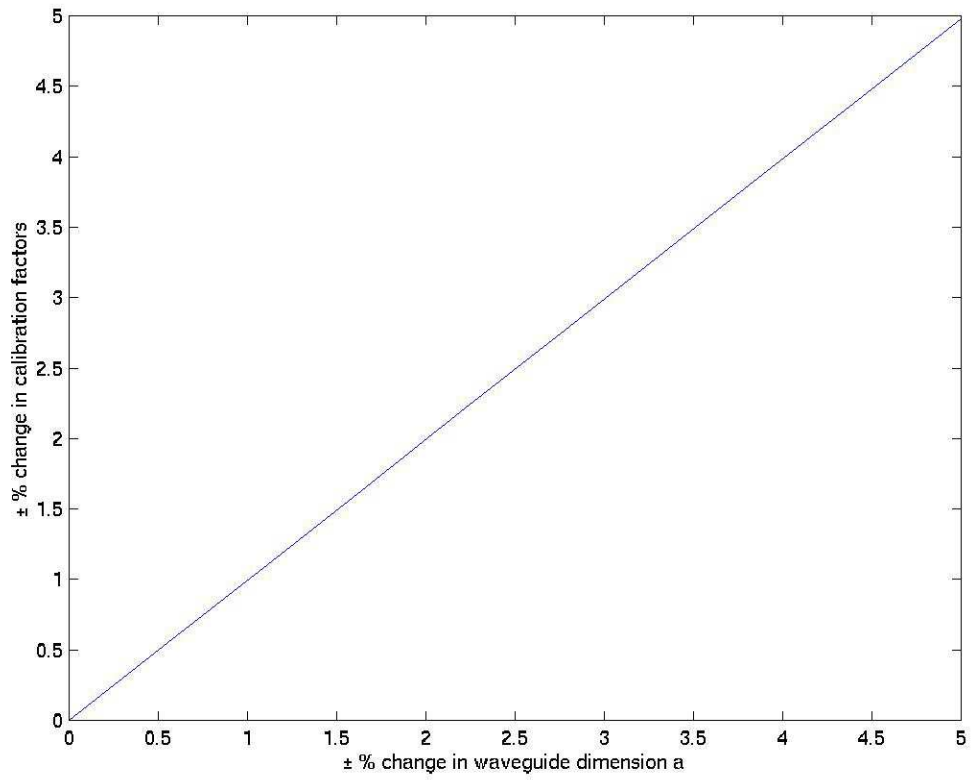


Figure 5.12: Change in calibration factors due to change in waveguide dimension  $a$  ( $\epsilon' = 40.00$   $\epsilon'' = 13.98$   $z = 15mm$ )

## Chapter 6

# Cell Phone Compliance Testing using SAM Phantom

In this chapter, the calculated complex permittivity and measured calibration factors are used for GSM cell phones compliance testing using a SAM phantom.

### 6.1 Introduction

Measurements are made inside a SAM phantom, Figure 3.2, with two different wireless phones placed close to the ear of the phantom to determine the peak spatial SAR averaged over 1-gram and 10-grams of tissue at 900MHz and 1800MHz. These measurements followed the testing procedures in the IEEE 1528 Standard [8], but with limits on the number of frequencies that will be tested. The two phones to be tested are: a Motorola Model V290; and a Nokia Model 6310i. Tests are made in the center of each band - 900MHz and 1800MHz, for both the "cheek", Figure 6.1, and "tilt", Figure 6.2, positions, and for both the left and right ear regions of the SAM phantom, Table 6.1. Tissue-equivalent recipes are found in IEEE standard 1528, Table 2.4.

Table 6.1: Total experiments for compliance testing

	Motorola V290		Nokia 6310i	
	Left	Right	Left	Right
900MHz	Cheek	Cheek	Cheek	Cheek
	Tilt	Tilt	Tilt	Tilt
1800MHz	Cheek	Cheek	Cheek	Cheek
	Tilt	Tilt	Tilt	Tilt

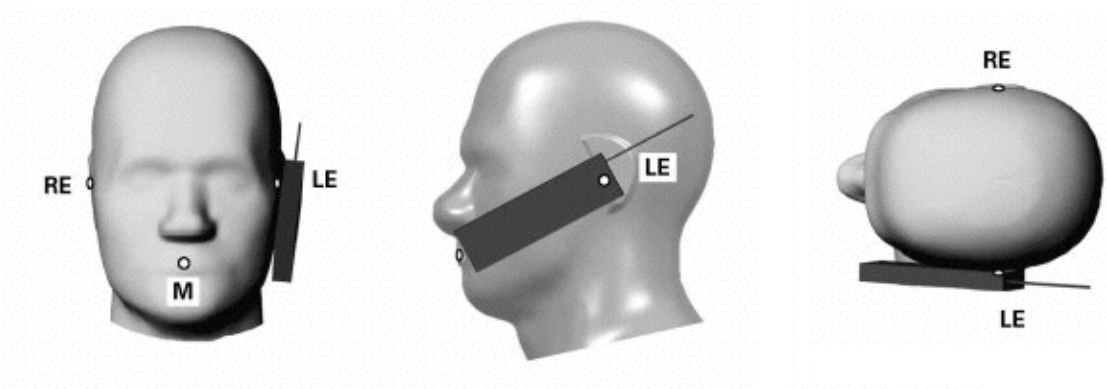


Figure 6.1: Cell-phone cheek position

## 6.2 Test Procedure

Figure 6.3 shows the setup for the compliance testing using the sam phantom (Figure A.7 Appendix A). The test procedure [1] is described in detail in IEEE standard 1528. The following is an overview of the steps followed:

- Read the IEEE 1528 procedure before beginning.
- Fill the SAM phantom with the appropriate tissue-equivalent liquid. Stir the liquid at the beginning of each day of testing. Allow any air bubbles to escape before making any measurements.
- Measure the temperature and humidity of the room. Repeat these measurements at the beginning of each day of testing.
- Measure density, temperature, dielectric constant, and conductivity of the tissue-equivalent liquid. Repeat these measurements at the beginning of each day of testing.

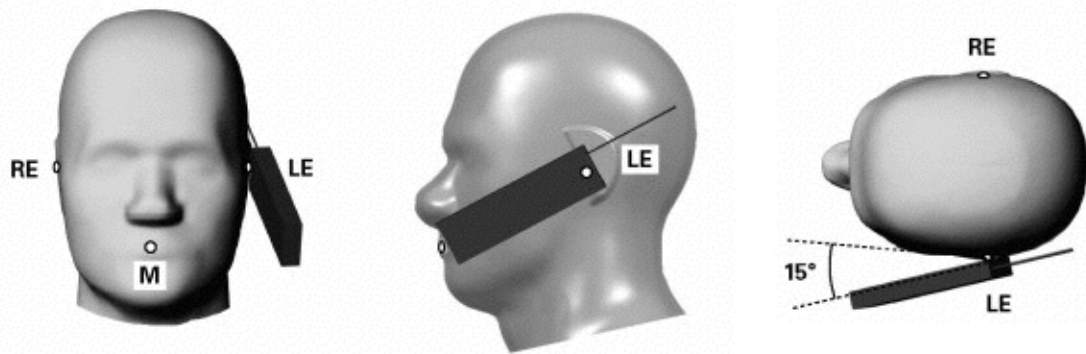


Figure 6.2: Cell-phone tilt position

- Check the temperature of the liquid. It must be within  $\pm 2^{\circ}C$  of the temperature that was recorded at the time the dielectric properties were measured
- Make sure that the phone battery is fully charged at the beginning of each experiment
- Mount the phone to be tested in the "cheek" or "tilt" position in the left or right ear area of the phantom, according to which measurement is to be performed.
- Activate the phone at maximum power in the center of the appropriate band.
- Position the E-field probe at the approximate center of the reference point in the ear area at the inner surface of the phantom, and make a reference measurement using the SAR measurement system. (This measurement will be compared to one made at the same point at the end of the test to characterize the drift of the measurement system.)
- Perform an area scan to determine the approximate location of the peak local SAR. A coarse grid of SAR values should be obtained. The area scan should meet the appropriate requirements for compliance testing.
- Perform a zoom scan (volume scan) to obtain the measurements used to determine the peak spatial SAR averaged over 1 gram and 10 gram cubical volumes. The zoom scan should be centered at the location of the peak local SAR that was determined from the area scan. The zoom scan should meet the appropriate requirements for

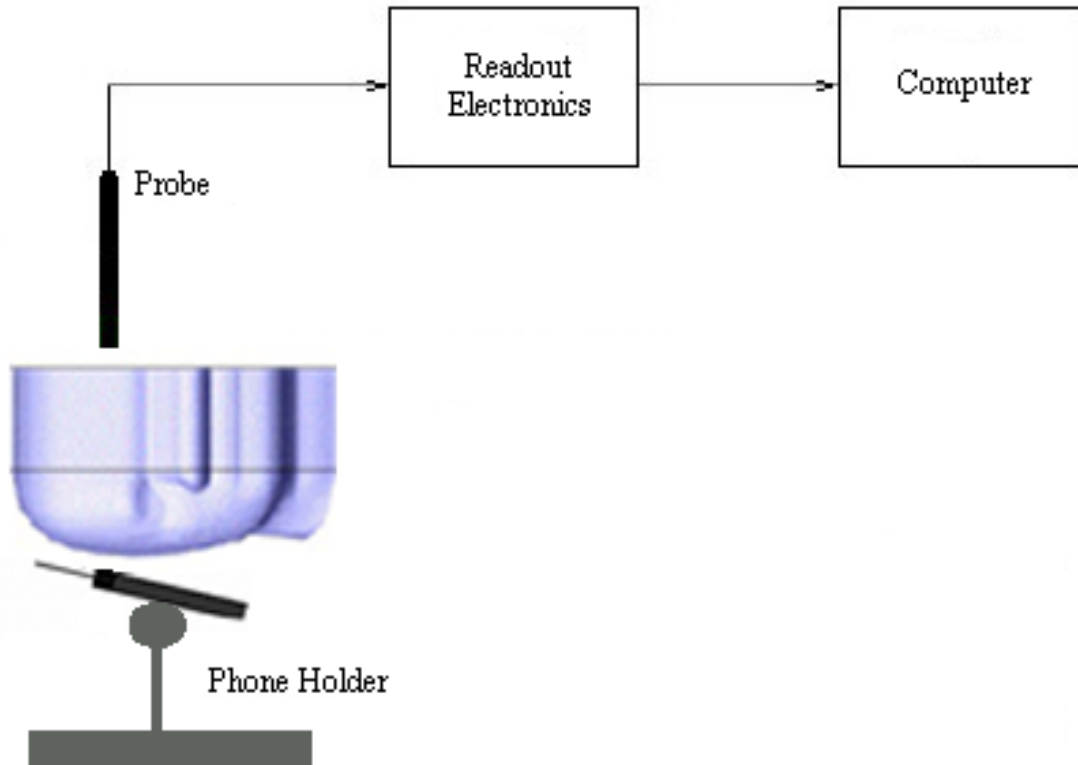


Figure 6.3: Cell-phone compliance testing using the SAM phantom

compliance testing. To obtain the resolution needed for the mass averaging, use the appropriate interpolation and extrapolation procedures that meet the requirements for compliance testing.

- Repeat the zoom scan with the probe rotated 90 degrees around the vertical axis from the previous position.
- Perform the reference measurement again at the same point that was previously used. If the measurement is different, then either the measurements should be repeated, or the appropriate error included in the reporting of the SAR value.
- Turn off the phone.

## 6.3 Results

The results for the cell-phone compliance tests are shown in Table 6.2. For the scans with superscripts 1 and 10; the maximum 1g and 10g volume averaging cubes were found at the edge of the scanned volume. This implies that part of the volume required to find the true maximum was not captured. The reason for the limited scanned volume was that the E-field probe contacted the wall of the SAM phantom close to the nose. Further, the angle between the probe and the surface of the SAM may exceed 30 degrees, as the E-field probe is always vertical in the rectilinear scanning system. The IEEE 1528 Standard specifies that the angle between the SAM surface and the probe should be smaller than 30 degrees. The reported uncertainties for the 1g and 10g averages are calculated using the guidelines in the IEEE 1528 Standard. The target uncertainty should be less than  $\pm 30\%$ .

Table 6.2: Measured 1g and 10g averages for cell-phone compliance tests

Phone	Frequency MHz	Side	Position	1g W/kg	10g W/kg
Motorola <sup>10</sup>	900.00	Left	Cheek	$0.66 \pm 18\%$	$0.45 \pm 18\%$
Motorola <sup>10</sup>	900.00	Left	Tilt	$0.25 \pm 18\%$	$0.18 \pm 18\%$
Motorola <sup>10</sup>	900.00	Right	Cheek	$0.53 \pm 18\%$	$0.37 \pm 18\%$
Motorola <sup>1</sup>	900.00	Right	Tilt	$0.15 \pm 18\%$	$0.11 \pm 18\%$
Motorola	1800.00	Left	Cheek	$0.52 \pm 18\%$	$0.36 \pm 18\%$
Motorola	1800.00	Left	Tilt	$0.11 \pm 18\%$	$0.08 \pm 18\%$
Motorola <sup>1</sup>	1800.00	Right	Cheek	$0.36 \pm 18\%$	$0.24 \pm 18\%$
Motorola	1800.00	Right	Tilt	$0.06 \pm 18\%$	$0.04 \pm 18\%$
Nokia <sup>10</sup>	900.00	Left	Cheek	$0.68 \pm 18\%$	$0.51 \pm 18\%$
Nokia <sup>10</sup>	900.00	Left	Tilt	$0.46 \pm 18\%$	$0.33 \pm 18\%$
Nokia	900.00	Right	Cheek	$0.68 \pm 18\%$	$0.50 \pm 18\%$
Nokia <sup>10</sup>	900.00	Right	Tilt	$0.54 \pm 18\%$	$0.39 \pm 18\%$
Nokia <sup>10</sup>	1800.00	Left	Cheek	$0.50 \pm 18\%$	$0.29 \pm 18\%$
Nokia <sup>10</sup>	1800.00	Left	Tilt	$0.52 \pm 18\%$	$0.29 \pm 18\%$
Nokia <sup>10</sup>	1800.00	Right	Cheek	$0.48 \pm 18\%$	$0.29 \pm 18\%$
Nokia <sup>10</sup>	1800.00	Right	Tilt	$0.40 \pm 18\%$	$0.24 \pm 18\%$

<sup>1</sup> The maximum 1g volume averaging cubes was found at the edge of the scanned volume. This implies that part of the volume required to find the true maximum was not captured.

<sup>10</sup> The maximum 10g volume averaging cubes was found at the edge of the scanned volume. This implies that part of the volume required to find the true maximum was not captured.

Figure 6.4 shows a sample plot for the SAR distribution for the Motorola V290 phone at 900MHz in the right cheek position. Figure 6.5 shows a sample plot for the SAR distribution for the Nokia 6310i phone at 1800MHz in the left tilt position.

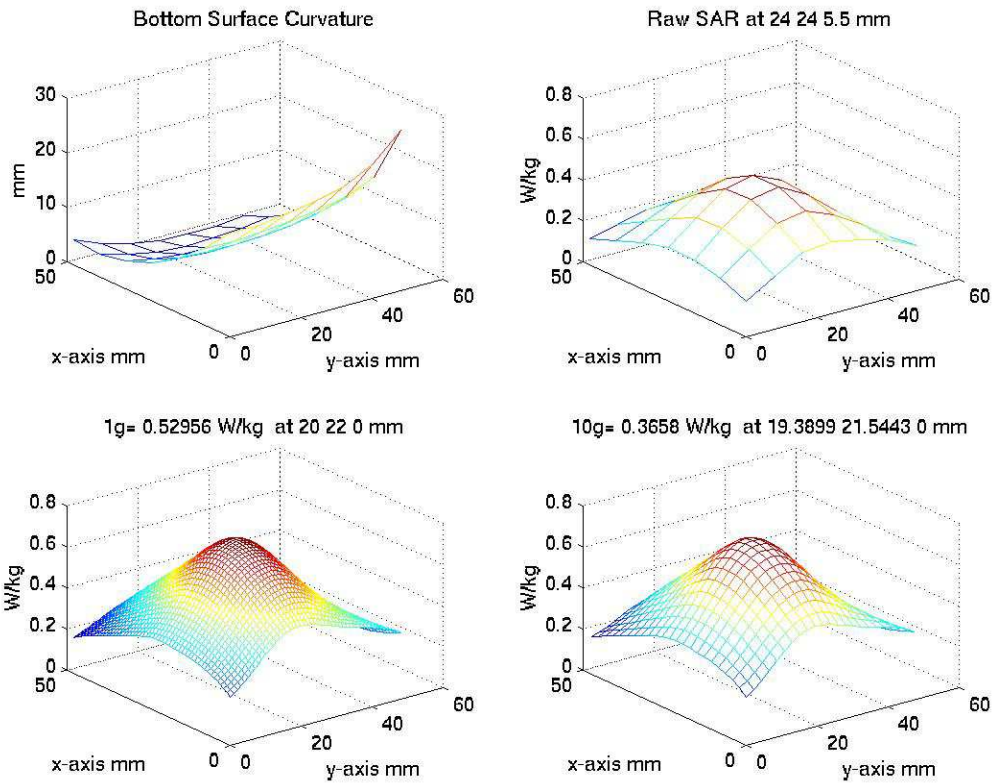


Figure 6.4: Motorola phone at 900MHz in the right cheek position

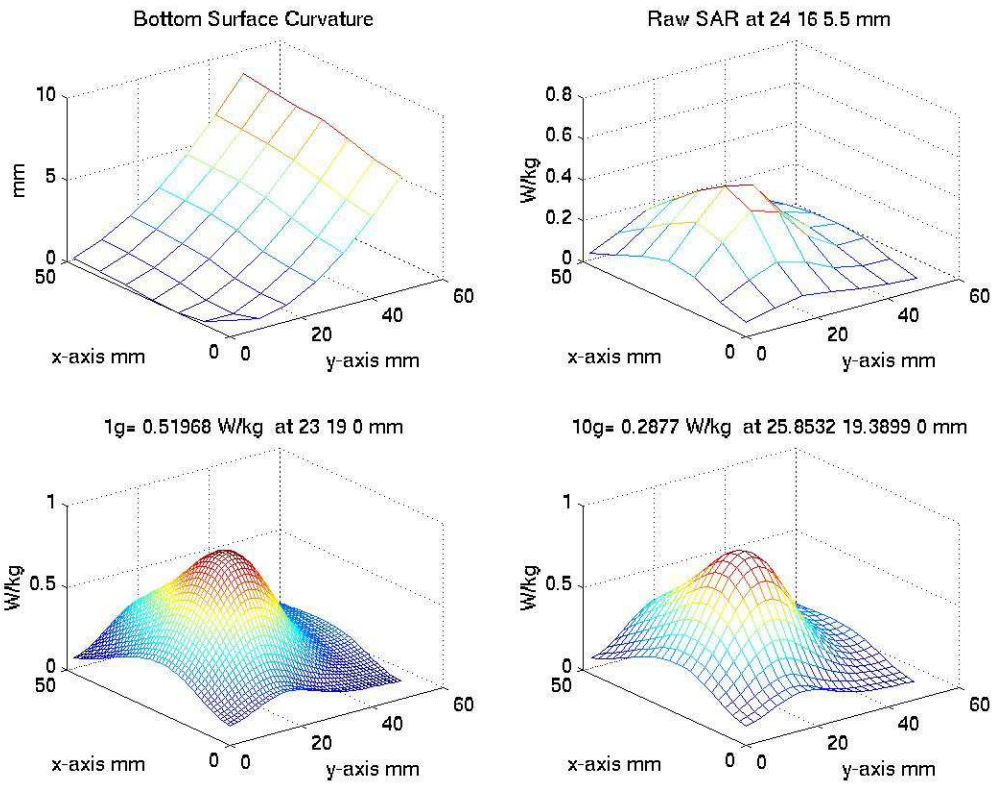


Figure 6.5: Nokia phone at 1800MHz in the left tilt position

# Chapter 7

## Conclusion

Chapter highlights and conclusions are presented. An overall summary of the thesis is also given.

### 7.1 Chapter Highlights

Chapter 1 stated the principle objective of this thesis. An introduction to the central topics of this thesis is presented.

Chapter 2 presented some background information and an overview was given for the standards, limits, and testing procedures for quantifying SAR. In order to measure exposure limits, the dielectric properties of the tissue-equivalent liquid used and the calibration factors for the probe used must be precisely calculated.

In chapter 3, the experimental design and approach for the calibration system was presented. A novel waveguide system is presented for both dielectric measurements and probe calibration.

The procedures used for calculating the dielectric properties, using field attenuation and power reflectance, and measuring the probe calibration factors, using probe isotropy data, are presented in chapter 4.

In chapter 5, the system is validated using standard saline solutions at different concentrations and are, to the best of the authors knowledge, the most accurate yet. Dielectric properties and calibration factors are calculated for tissue-equivalent liquids at 900MHz and 1800MHz. The uncertainties were evaluated for the system.

GSM cell phone compliance testing using a SAM phantom at 900MHz and 1800MHz is presented in chapter 6.

## 7.2 Summary

Wireless devices must meet specific safety radiation limits, and in order to assess the health affects of such devices, standard procedures are used in which standard phantoms, tissue-equivalent liquids, and miniature electric-field probes are used. The accuracy of such measurements depend on the precision in measuring the dielectric properties of the tissue-equivalent liquids and the associated calibrations of the electric-field probes.

A calibration system has been presented that uses a waveguide for precisely calculating tissue-equivalent liquid properties and calibrating miniature electric field probes. The system is robust, and easy to use and implement. Furthermore, using the same waveguide for tissue-equivalent dielectric measurements and calibrating e-field probes in SAR measurements eliminates a source of uncertainty. The calibration system presented, to the best of the authors knowledge, is novel.

The work presented in this thesis is the first complete and accurate assessment of probe calibration, simulant fluid characterization, and actual cell phone SARs made for verifying the validity of specified verification protocols for cell phone certification. These measurements have been carried out independently of any manufacturer of phantoms, cell phones, dielectric measurement probes, or manufacturer supplied probe calibration factors.

# Appendix A

## Components and Setup

Pictures of the components used and system setup are shown:

- Figure A.1: Picture of an E-Field probe
- Figure A.2: Picture of the flat phantom used for system validation
- Figure A.3: Picture of the right and left side SAM phantoms used for compliance testing
- Figure A.4: Picture of 900MHz and 1800MHz waveguides
- Figure A.5: Picture of Waveguide Z-Scan setup
- Figure A.6: Picture of Waveguide Iso-Scan setup
- Figure A.7: Picture of compliance testing setup



Figure A.1: E-Field probe SPEAG 1422

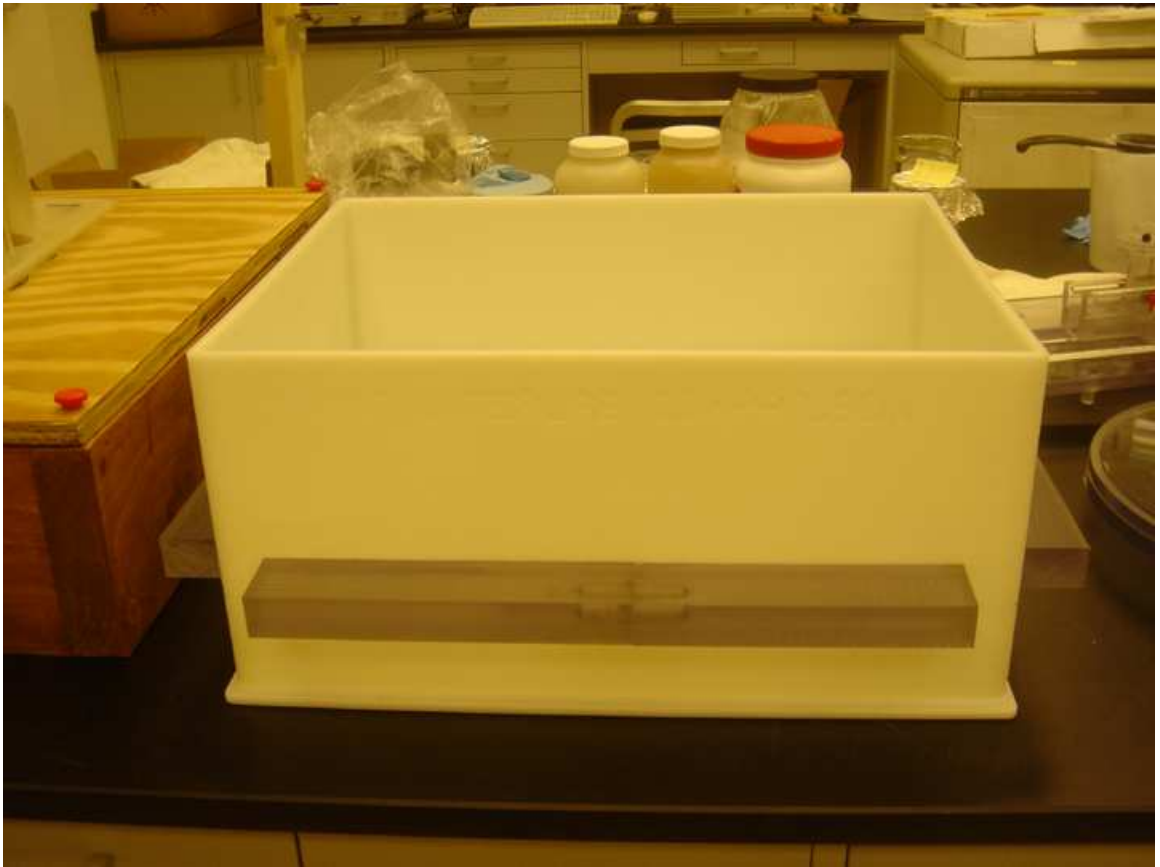


Figure A.2: Flat Phantom for system validation



Figure A.3: Left and Right SAM Phantoms for compliance testing



Figure A.4: 900MHz waveguide (left) 1800MHz waveguide (right)



Figure A.5: Waveguide Z-Scan setup



Figure A.6: Waveguide Iso-Scan

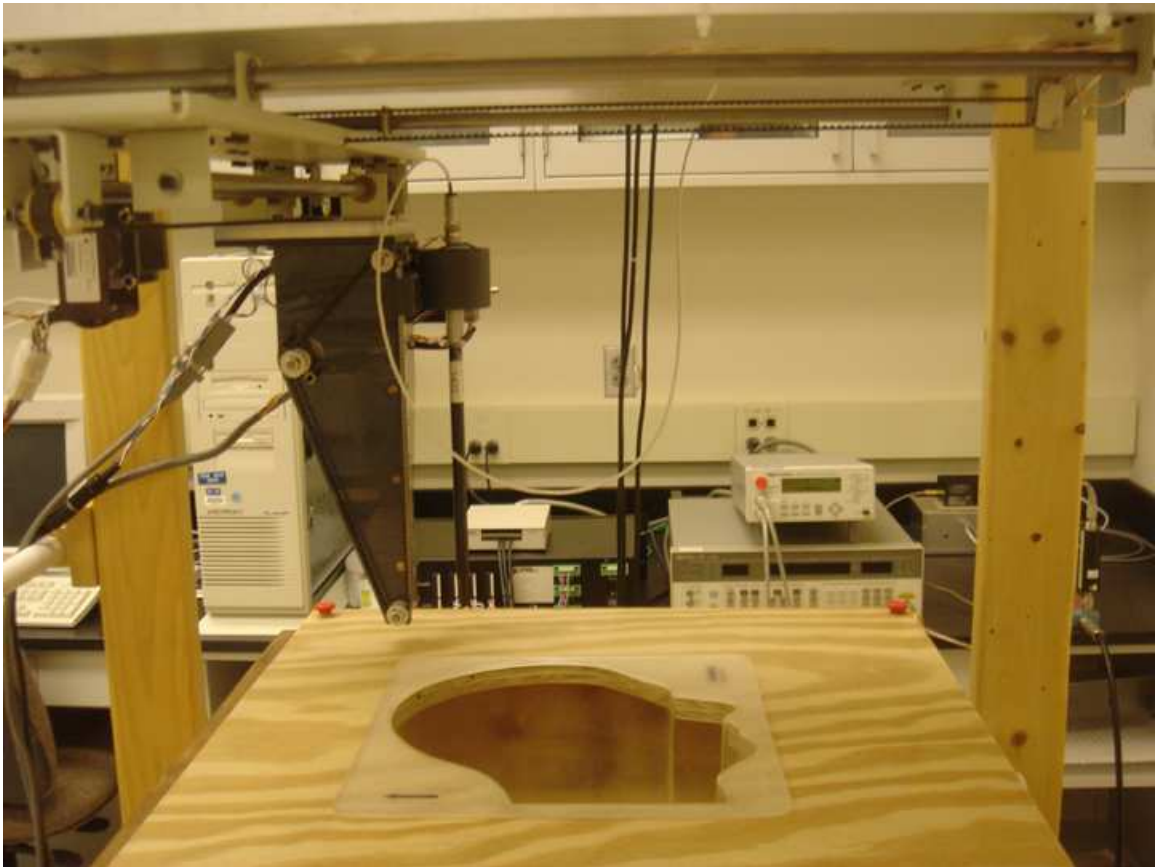


Figure A.7: Compliance testing setup

## Appendix B

# Waveguide Fundamental Mode Equation in Lossy Media

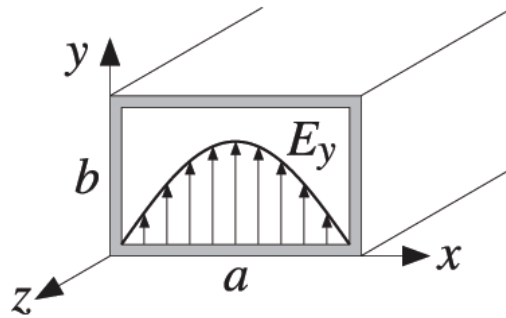


Figure B.1: Rectangular Waveguide

The expressions for the electric and magnetic fields for the waveguide fundamental mode  $TE_{10}$  are given by Equations (B.2-B.5), Figure B.1. For detailed derivation of waveguide modes refer to [27, 28, 29].

$$E_x = E_z = H_y = 0 \quad (\text{B.1})$$

$$E_y = E_0 \sin\left(\frac{\pi}{a}x\right) e^{-jk_z z} \quad (\text{B.2})$$

$$H_x = -\frac{k_z}{\omega\mu_0} E_0 \sin\left(\frac{\pi}{a}x\right) e^{-jk_z z} \quad (\text{B.3})$$

$$H_z = j \frac{\pi}{a} \frac{1}{\omega \mu_0} E_0 \sin\left(\frac{\pi x}{a}\right) e^{-jk_z z} \quad (\text{B.4})$$

$$k_z = \sqrt{\omega^2 \mu_0 \epsilon_0 \epsilon - \left(\frac{\pi}{a}\right)^2} \quad (\text{B.5})$$

where  $k_z$  is the transverse propagation constant.

Substituting the complex permittivity, and the expression for the conductivity

$$\epsilon = \epsilon' - j\epsilon'' \quad (\text{B.6})$$

$$\sigma = \omega \epsilon_0 \epsilon'' \quad (\text{B.7})$$

the transverse propagation constant becomes

$$k_z = \sqrt{\beta^2 - j\alpha} \quad (\text{B.8})$$

where

$$\beta = \sqrt{\omega^2 \mu_0 \epsilon_0 \epsilon' - \left(\frac{\pi}{a}\right)^2} \quad (\text{B.9})$$

$$\alpha = \frac{\omega \mu_0 \sigma}{a\beta} \quad (\text{B.10})$$

Applying the two term Taylor expansion

$$\sqrt{a^2 - x^2} \sim a - \frac{1}{2} \frac{x^2}{a} \quad (\text{B.11})$$

yields the following expression for the transverse propagation constant

$$k_z = \beta - j\alpha \quad (\text{B.12})$$

Substituting Equation (B.12) in Equations (B.2-B.5) gives

$$E_y = E_0 \sin\left(\frac{\pi x}{a}\right) e^{-j\beta z} e^{\alpha z} \quad (\text{B.13})$$

$$H_x = \frac{1}{\omega\mu_0} (-\beta + j\alpha) E_0 \sin\left(\frac{\pi}{a}x\right) e^{-j\beta z} e^{\alpha z} \quad (\text{B.14})$$

$$H_z = j\frac{\pi}{a} \frac{1}{\omega\mu_0} E_0 \sin\left(\frac{\pi}{a}x\right) e^{-j\beta z} e^{\alpha z} \quad (\text{B.15})$$

The total power  $P_T$  carried by the fields along the waveguide is obtained by integrating the  $z$  component of the Poynting vector  $S_z$  over the cross-sectional area of the waveguide

$$P_T = -\frac{1}{2} \int_0^b \int_0^a S_z dx dy = -\frac{1}{2} \int_0^b \int_0^a \text{Re} \{E_y \times H_x^*\} dx dy = \frac{ab\beta}{4\omega\mu_0} |E_0|^2 \quad (\text{B.16})$$

The RMS magnitude of the electric field inside the waveguide is then

$$|E| = \sqrt{\frac{4P\omega\mu_0}{ab2\beta}} \sin\left(\frac{\pi}{a}x\right) e^{\frac{-z\omega\mu_0\sigma}{2\beta}} \quad (\text{B.17})$$

## Appendix C

# Waveguide Power Reflectance

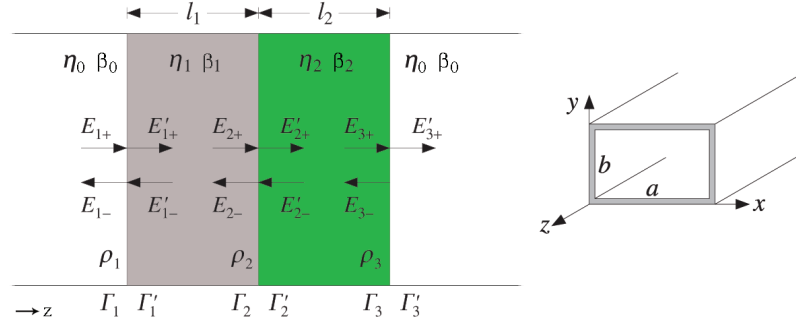


Figure C.1: Power reflectance for Two Layers inside a Waveguide

Figure C.1 shows a three-interface rectangular waveguide with dielectric layers  $\eta_1$  and  $\eta_2$ .

Media impedances and propagation constants are given by

$$\eta_0 = \frac{j\omega\mu_0}{\beta_0} \quad (\text{C.1})$$

$$\eta_1 = \frac{j\omega\mu_0}{\beta_1} \quad (\text{C.2})$$

$$\eta_2 = \frac{j\omega\mu_0}{\beta_2} \quad (\text{C.3})$$

$$\beta_0 = \sqrt{\left(\frac{\pi}{a}\right)^2 - \omega^2\mu_0\epsilon_0} \quad (\text{C.4})$$

$$\beta_1 = \sqrt{\left(\frac{\pi}{a}\right)^2 - \omega^2\mu_0\epsilon_1} \quad (\text{C.5})$$

$$\beta_2 = \sqrt{\left(\frac{\pi}{a}\right)^2 - \omega^2\mu_0\epsilon_2} \quad (\text{C.6})$$

Let  $\rho_1$ ,  $\rho_2$ , and  $\rho_3$  be the elementary reflection coefficients from the left side of the three interfaces

$$\rho_1 = \frac{\eta_1 - \eta_0}{\eta_1 + \eta_0} \quad (\text{C.7})$$

$$\rho_2 = \frac{\eta_2 - \eta_1}{\eta_2 + \eta_1} \quad (\text{C.8})$$

$$\rho_3 = \frac{z_0 - z_s}{z_0 + z_s} \quad (\text{C.9})$$

Assuming that the incident field is from the left-most media, and thus, in the right-most media there is only a forward-traveling wave. From the impedance matching conditions at an interface  $Z = Z'$  the reflection coefficient at the left side of an interface can be related to that on the right side by  $\Gamma'$

$$\Gamma = \frac{\rho + \Gamma'}{1 + \rho\Gamma'} \quad (\text{C.10})$$

From the forward and backward waves, the reflection coefficients are related by

$$\Gamma_1 = \frac{E_{1-}}{E_{1+}} = \frac{E_{2-}e^{-j\beta l}}{E_{2+}e^{j\beta l}} \Rightarrow \Gamma_1 = \Gamma_2 e^{-2j\beta l} \quad (\text{C.11})$$

where  $l$  is the media thickness.

To determine the reflection coefficient  $\Gamma_1$ , apply Equation (C.10) to relate  $\Gamma_1$  to the reflection coefficient  $\Gamma'_1$  at the right side of the first interface

$$\Gamma_1 = \frac{\rho_1 + \Gamma'_1}{1 + \rho_1\Gamma'_1} \quad (\text{C.12})$$

Then propagate  $\Gamma'_1$  to the left of the second interface by applying Equation (C.11) to yield

$$\Gamma_1 = \frac{\rho_1 + \Gamma_2 e^{-2j\beta_1 l_1}}{1 + \rho_1\Gamma_2 e^{-2j\beta_1 l_1}} \quad (\text{C.13})$$

At the second interface, apply Equation (C.10) and Equation (C.11) again to get an expression for  $\Gamma_2$

$$\Gamma_2 = \frac{\rho_2 + \Gamma_3 e^{-2j\beta_2 l_2}}{1 + \rho_2\Gamma_3 e^{-2j\beta_2 l_2}} \quad (\text{C.14})$$

Since there is no backward-traveling wave in the right-most media, then  $\Gamma'_3 = 0$ , which implies  $\Gamma_3 = \rho_3$ . Substituting for  $\Gamma_2$  into  $\Gamma_1$  yields the following expression for the reflection coefficient  $\Gamma_1$  at the left side of the first interface

$$\Gamma_1 = \frac{\rho_1 + \rho_2 e^{-2\beta_1 l_1} + \rho_1 \rho_2 \rho_3 e^{-2\beta_2 l_2} + \rho_3 e^{-2\beta_1 l_1} e^{-2\beta_2 l_2}}{1 + \rho_1 \rho_2 e^{-2\beta_1 l_1} + \rho_2 \rho_3 e^{-2\beta_2 l_2} + \rho_1 \rho_3 e^{-2\beta_1 l_1} e^{-2\beta_2 l_2}} \quad (\text{C.15})$$

## Appendix D

# CalPer: LabVIEW Program

CalPer is a Labview program that controls a three dimensional scanner for positioning an E-field Probe for Electric field measurements in a Waveguide, Flat Phantom, or a SAM Phantom. The program interfaces with MATLAB for postprocessing.

The main menu is shown in Figure D.1. There are eight possible function to execute. But the last three functions can only be executed when the very first function is executed "Initilize/Home scanner". A description for each function is presented here.

### D.1 Initilize/Home scanner

This function moves the probe to the origin of the scanner regardless of the current position. When the function is operating the "Busy" turns green and turns off when initializing is complete. This also applies for all other function.

### D.2 Read Iso-Scan File

The Iso-Scan files are generated when the "Waveguide Iso Scan" function is executed. A window acquiring for the file to be read is shown in Figure D.2. After the file is read, the calibration factors and the uncertainties are produces, Figure D.3.

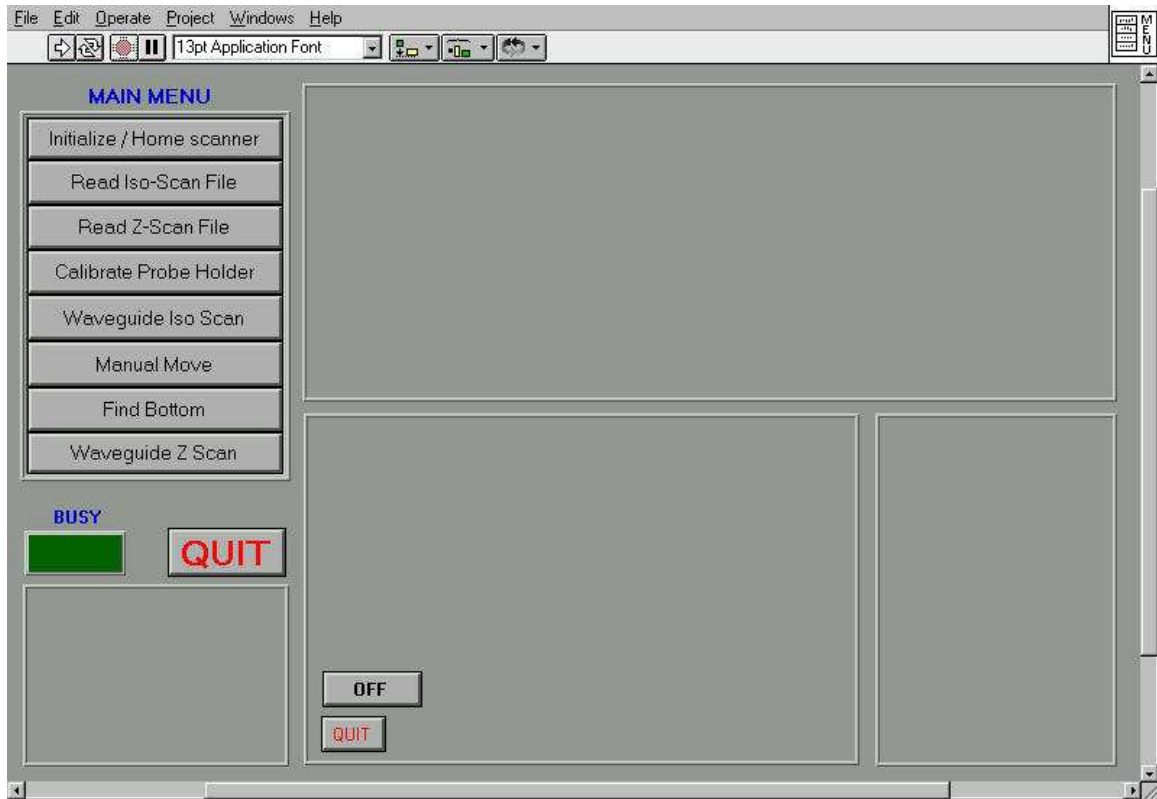


Figure D.1: Main Menu Window

### D.3 Read Z-Scan File

The Z-Scan files are generated when the "Waveguide Z Scan" function is executed. A window acquiring for the file to be read is shown in Figure D.2. After the file is read, the dielectric parameters and the uncertainties are produced, Figure D.4.

### D.4 Calibrate Probe Holder

The probe holder is equipped with three sensors at  $120^\circ$  from each other. The sensors are used to detect and stops the scanner from allowing the probe to go down along the  $z$ -axis when something is obstructing the probes movement. The sensors also detect and stop movement when the probe is tilted too much. Figure D.5 shows when all the sensors are within limits.

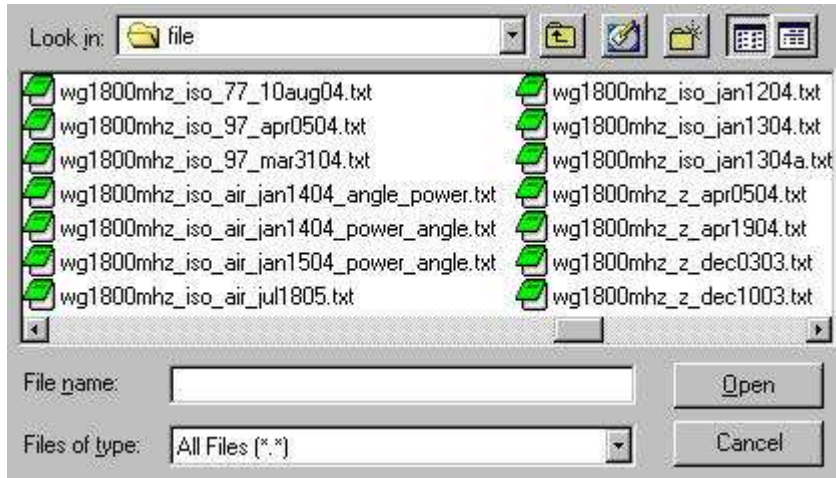


Figure D.2: File dialog window

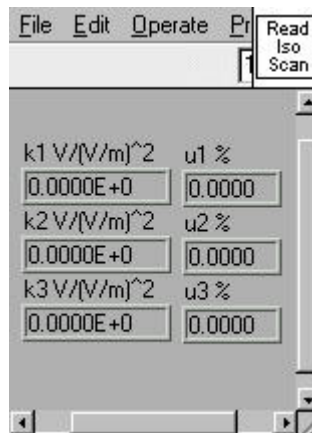


Figure D.3: Iso-Scan Results Window

The sensors can be made more or less sensitive by tightening or relaxing a screw for each sensor. To check the sensitivity of a sensor the probe is moved by hand towards the sensor. Figure D.6 shows when sensor 1 has reached the limit.

## D.5 Waveguide Iso Scan

When this function is invoked, a file dialog windows will prompts the user for the file name to store the data in Figure D.2. The user then enters the scan parameters Figure D.7.

The iso-scan menu then prompts the user to rotate the probe to the specified angle. When the probe is rotated, the user then clicks on the power scan button. The power is then

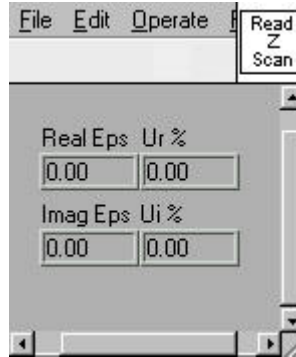


Figure D.4: Z-Scan Results Window

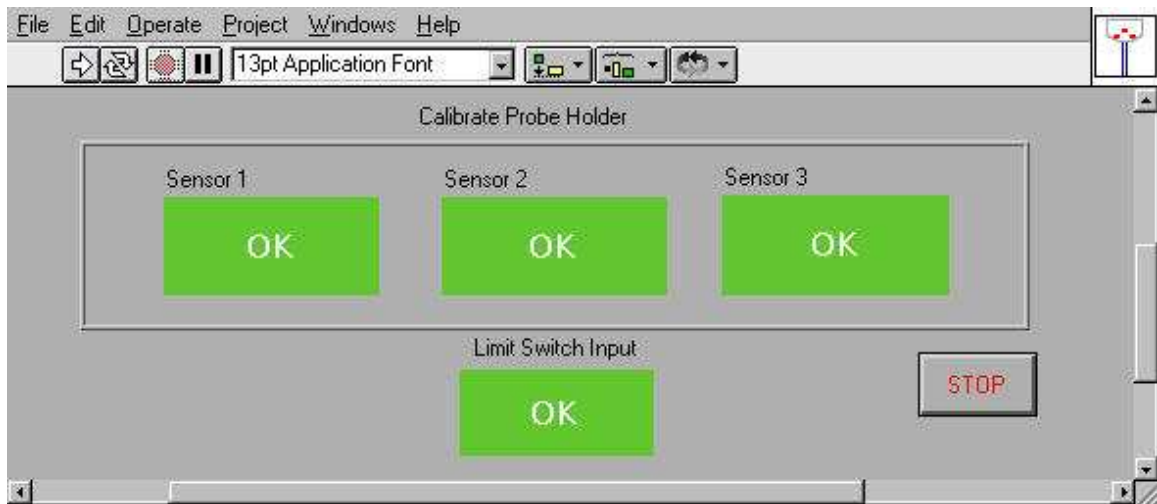


Figure D.5: Probe Holder Calibration

swept through all the specified power levels. When the scan is done, the results window reports the calibration factors and associated uncertainties, Figure D.3. The elapsed time is also reported, Figure D.13.

## D.6 Manual Move

This function allows the user to move the probe to any position within the limits, Figure D.9. The values entered are steps in either  $x$ ,  $y$ , or  $z$  direction.

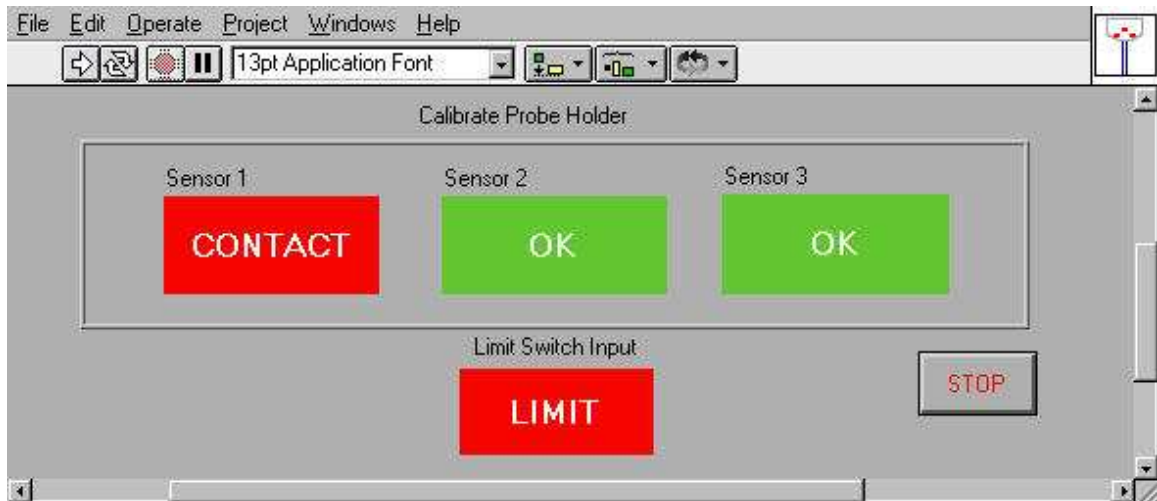


Figure D.6: Probe Holder with contact in Sensor 1

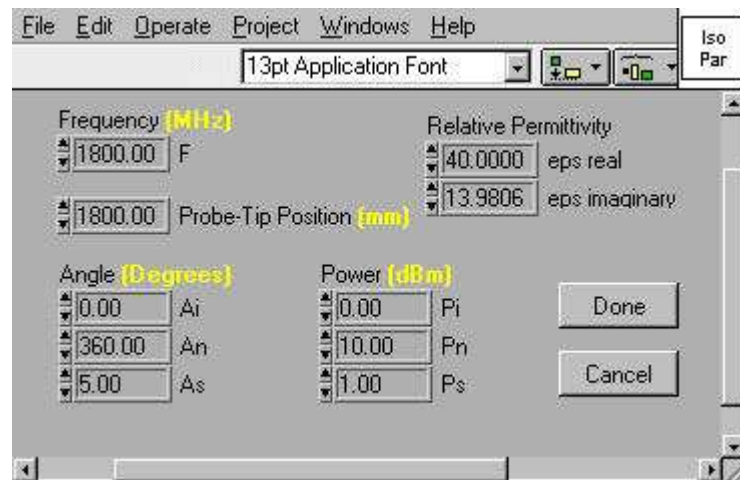


Figure D.7: Iso-Scan Parameter Window

## D.7 Find Bottom

This function is used to search for the bottom. The probe is moved downward along the  $z$ -axis very slowly until contact is made, and the position is shown. Figure D.10

## D.8 Waveguide Z Scan

When this function is invoked, a file dialog windows will prompts the user for the file name to store the data in Figure D.2. The user then enters the scan parameters Figure D.11.

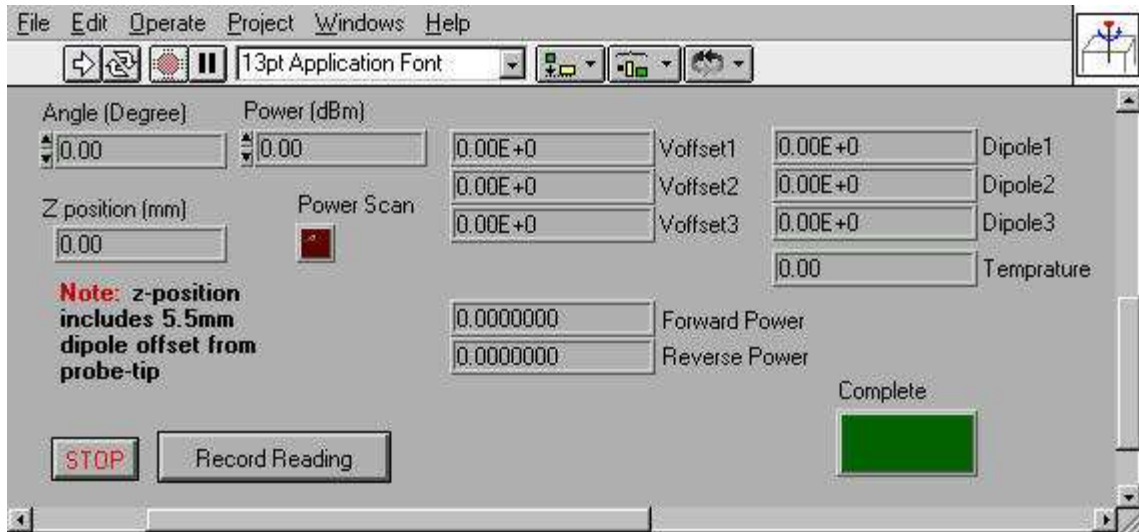


Figure D.8: Iso-Scan Window

The program starts the z-scan and the probe voltage, power readings are reported, along with the probe position and completed points percentages, Figure D.12. When the scan is done, the results window reports the real and imaginary permittivity and associated uncertainties, Figure D.4. The elapsed time is also reported, Figure D.13.

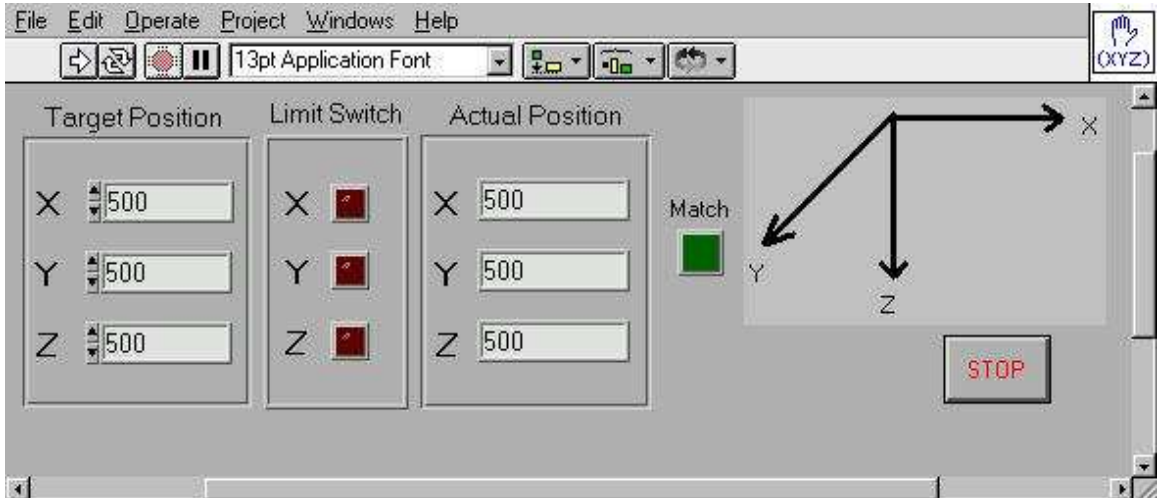


Figure D.9: Manual Move Window

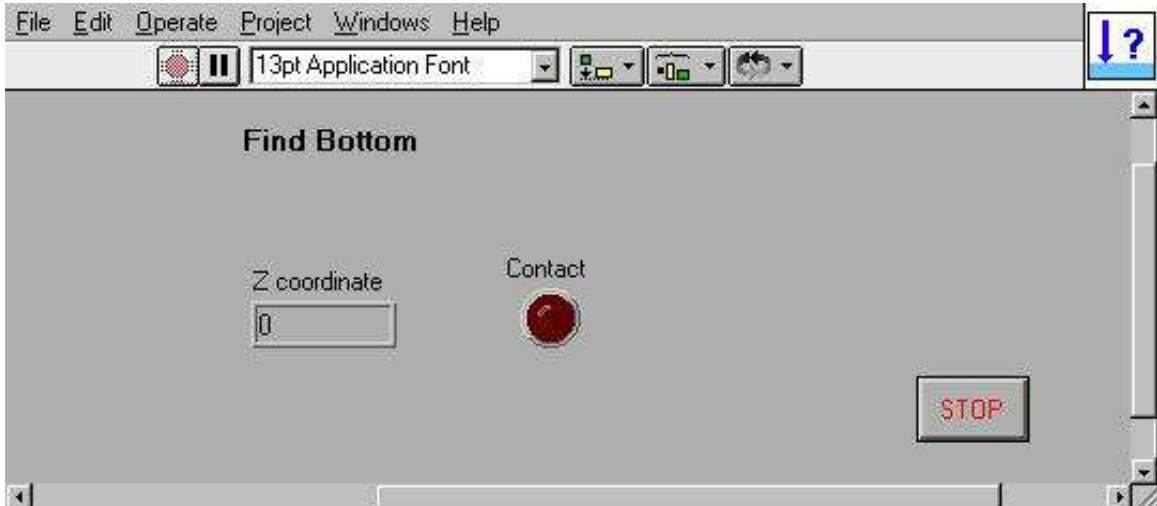


Figure D.10: Find Bottom Window

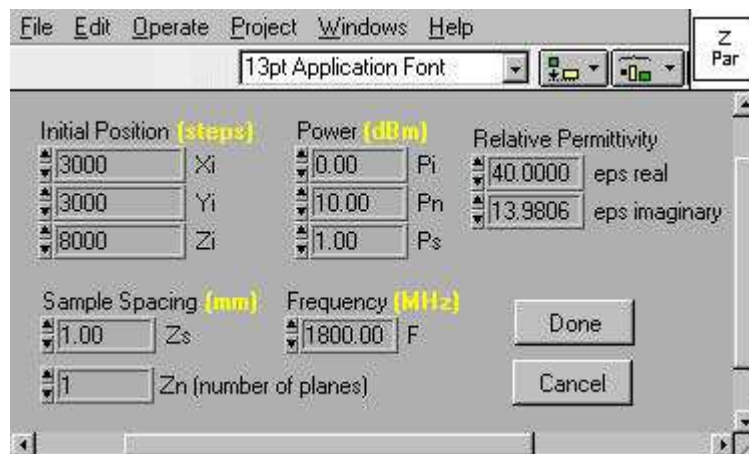


Figure D.11: Z-Scan Parameter Window

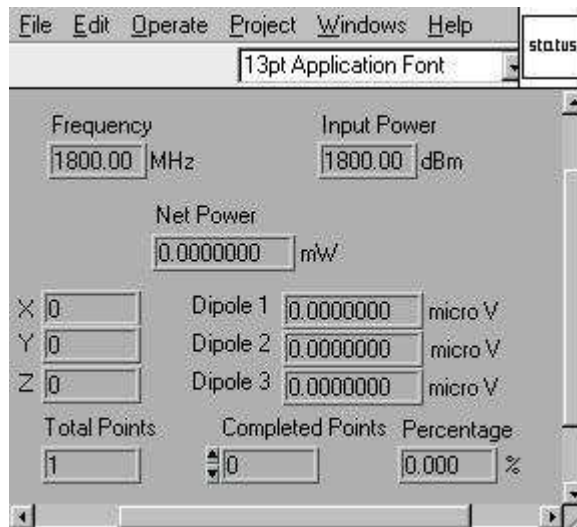


Figure D.12: Status Window

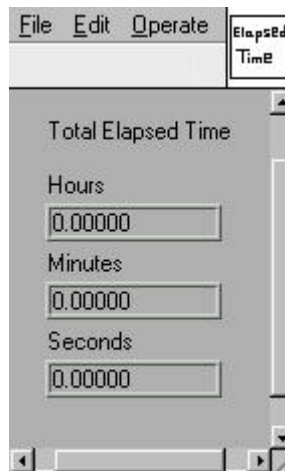


Figure D.13: Elapsed Time Window

# Appendix E

## Program Listing

### E.1 wgz.m

```
% Calculate complex permittivity using nonlinear least-square fit from data
% obtained from labview of a vaveguide z-scan
%
% The Labview file is organized as follows:
% Column 1 2 3 4 5 6 7 8 9 10 11 12 13 14
%      X Y Z V1 V2 V3 Temp Voff1 Voff2 Voff3 Pfor Prev Freq Pin
%      15      16
%      Eps real Eps imaginary
%
% X, Y and Z in Steps
% Temp in Degrees Celcius
% V1, Voff1, V2, Voff2, V3, and Voff3 in Volts
% Pfor and Prev in Watts
% Pin in dBm

clear; % clear variables and functions from memory
```

```

clc;    % clear command window

% z-scan file
fprintf('waveguide z scan file name');
fp=input(': ', 's');

% load file into variable and get size in rows and columns
file=load(fp);
[r,c]=size(file);

% scan parameters from file
zn=size(find((file(:,14)-file(1,14))==0),1); % number of z planes
pn=r/zn; % number of power sweep points
p=file(1:zn:r,14); % power sweep
epsr=file(1,15); % real permittivity
epsi=file(1,16); % imaginary permittivity

% get z range in steps
z=reshape(file(:,3),zn,r/zn);
z=flipud(mean(z'))';

% calculate z in meters
z=z-z(1);
z=z/98.2;
z=round(z)*1e-3+10e-3;

% load measured values
d1=file(:,4); % raw dipole 1 voltage
d2=file(:,5); % raw dipole 2 voltage
d3=file(:,6); % raw dipole 3 voltage

```

```

temp=file(:,7); % ambient temprature
vo1=file(:,8); % dipole 1 offset voltage
vo2=file(:,9); % dipole 2 offset voltage
vo3=file(:,10); % dipole 3 offset voltage
pf=file(:,11); % forward power
pr=file(:,12); % reverse power
fq=file(1,13); % operating frequency

% compute actual probe voltages and cooresponding e-field
[v1,v2,v3]=vcorrect(d1,d2,d3,vo1,vo2,vo3);
e1=sqrt(v1); e2=sqrt(v2); e3=sqrt(v3);
em=sqrt(e1.^2+e2.^2+e3.^2); % measured electric-field magnitude
em2=em.^2; % measured electric-field magnitude squared

% correct for coupler losses
% and compute net propagating power in waveguide
[pfw,prv]=pcorrect(pf,pr,fq);
pnet=pfw-prv;

% caculate normalized electric-field magnitude squared
em2n=em2./pnet;

% rearrange em2n vector so that:
% z points in rows
% power sweep in columns
em2n=reshape(em2n,zn,pn);

% take average about power sweep points
em2na=mean(em2n,2);

```

```

% nonlinear fit
x0=[1 1]';
[x,xiter,ste]=gn(x0,'funz',z,em2na);
d=x(2);

% calculate uncertainty from asymptotic standard error for x
n=length(z);          % number of data points
xpar=length(x);      % number of parameters
xt=qt(0.975,n-xpar); % t-dis at alpha=0.05 [two-tail p=1-0.05/2=0.975]
u=ste*xt;             % +/- uncertainty
up=u./x*100;         % percent uncertainty

% calculate reflectance form power measurements
gam=reshape(prv./pfw,zn,pn);
gam=mean(mean(gam,2));

% calculate real and imaginary permittivity of
% tissue-equivalent liquid
opt=optimset('display','off');
if fq==900e6
ear=2.2;
elseif fq==1.8e9
ear=1.6;
end
er=fminbnd('funesr',0,100,opt,ear,d,gam,fq);
ei=fminbnd('funesi',0,100,opt,ear,d,gam,fq);

% apply monte calro simulation to calculate uncertainty
% waveguide cross section a x b
if fq==1.8e9

```

```

        a=109.22e-3; b=a/2;
elseif fq==900e6
        a=247.65e-3; b=a/2;
end
se=std_ee([ear 1],[d 1],[gam 1.7],[fq 0.01],[a 0.01],100);

% output section

% real and imaginary permittivity and conductivity
fprintf('\n Tissue-Equivalent liquid at %2.2e Hz \n',fq);

fprintf('\n VNA: \n');
fprintf('\t er=%2.2f \t ur=%1.2f %% \n',epsr,5);
fprintf('\t ei=%2.2f \t ui=%1.2f %% \n',epsi,5);
fprintf('\t sg=%2.2f \t us=%1.2f %% \n',2*pi*fq*8.8542e-12*epsi,5);

fprintf('\n Waveguide using alpha and gamma: \n');
fprintf('\t er=%2.2f \t ur=%1.2f %% \n',er,se(1));
fprintf('\t ei=%2.2f \t ui=%1.2f %% \n',ei,se(2));
fprintf('\t sg=%2.2f \t us=%1.2f %% \n',2*pi*fq*8.8542e-12*ei,se(2));

fprintf('\n Waveguide using gamma: \n');
fprintf('\t er=%2.2f \t ur=%1.2f %% \n',xx(1),se(1));
fprintf('\t ei=%2.2f \t ui=%1.2f %% \n',xx(2),se(2));
fprintf('\t sg=%2.2f \t us=%1.2f %% \n',2*pi*fq*8.8542e-12*xx(2),se(2));

% plot section

% plot alpha
figure; plot(z*1e3,funz(x,z));

```

```

xlabel('z-axis (mm)');
ylabel('|E|^2');
title(['\alpha' '=' num2str(d)]);

% plot gamma
pp=reshape(pnet,zn,pn)';
pp=pp(:,1)*1e3;
gm=mean(reshape(prv./pfw,zn,pn))';
figure; plot(pp,gm);
axis([min(pp) max(pp) 0 1]);
xlabel('net power (mW)');
ylabel('\Gamma^2');
title(['\Gamma^2' '=' num2str(gam)]);

```

## E.2 wgis0.m

```

% Calculate E-Field probe calibration factors
% for each dipole
%
% The Labview file is organized as follows:
% Column 1 2 3 4 5 6 7 8 9 10 11 12 13 14
% X Y Z V1 V2 V3 Temp Voff1 Voff2 Voff3 Pfor Prev Freq Pin
% 15 16 17
% Eps real Eps imaginary Angle
%
% X, Y and Z in Steps; Temp in Degrees Celcius
% Vi and Voffi are in Volts; Pfor and Prev in Watts
% Pin in dBm; Angle in degrees

```

```

clear; % clear variables and functions from memory
clc; % clear command window

% iso-scan file
fprintf('waveguide isotropy scan file name');
fp=input(': ','s');

% load file into variable and get size in rows and columns
file=load(fp);
[r,c]=size(file);

% scan parameters from file
pn=size(find(file(1,17)==file(:,17)),1); % number of power sweep points
an=r/pn; % number of angle steps
a=file(1:pn:r,17); % angle steps in degrees
rd=a*pi/180; % angle steps in radians
p=file(1:pn,14); % power sweep
z=file(1,3)*1e-3; % z location in meters
f=file(1,13); % frequency in Hz
er=file(1,15); % real permittivity
ei=file(1,16); % imaginary permittivity

% load measured values
d1=file(:,4); % raw dipole 1 voltage
d2=file(:,5); % raw dipole 2 voltage
d3=file(:,6); % raw dipole 3 voltage
temp=file(:,7); % ambient temprature
vo1=file(:,8); % dipole 1 offset voltage
vo2=file(:,9); % dipole 2 offset voltage
vo3=file(:,10); % dipole 3 offset voltage

```

```

pf=file(:,11); % forward power
pr=file(:,12); % reverse power

% compute actual probe voltages and cooresponding e-field
[v1,v2,v3]=vcorrect(d1,d2,d3,vo1,vo2,vo3);
e1=sqrt(v1); e2=sqrt(v2); e3=sqrt(v3);
em=sqrt(e1.^2+e2.^2+e3.^2); % measured electric-field magnitude
em2=em.^2; % measured electric-field magnitude squared

% correct for oupler losses
% and compute net propagating power in waveguide
[pfw,prv]=pcorrect(pf,pr,f);
pnet=pfw-prv;

% caculate normalized electric-field magnitude squared
em2n=em2./pnet;

% rearrange em2n vector so that:
% angle points in rows
% power sweep in columns
em2n=reshape(em2n,pn,an)';

% take average about power sweep points
em2na=mean(em2n,2);

% calculate total probe e-field magnitude
ep=eprobe(v1,v2,v3,f);
ep=reshape(ep,pn,an)';
epa=mean(ep,2);

```

```

% calculate total theoretical e-field magnitude (TE01; fundamental mode)
et=etheory(er,ei,z,pnet,f);
et=reshape(et,pn,an)';
eta=mean(et,2);

% calculate e-field value from pokovic paper (TE01; fundamental mode)
ev=epokovic(er,ei,z,pnet,f);
ev=reshape(ev,pn,an)';
eva=mean(ev,2);

% calculate calibration factors using linear fit
v1=reshape(v1,pn,an)';
v2=reshape(v2,pn,an)';
v3=reshape(v3,pn,an)';
e2=et.^2;
k=factors(v1,v2,v3,e2);

% calculate calibration factors using nonlinear fit
pnet=reshape(pnet,pn,an)';
vv=[mean(v1./pnet,2) mean(v2./pnet,2) mean(v3./pnet,2)];
ee=mean(et.^2./pnet,2);
x0=[1e-6 1e-6 1e-6]'; % initial guess
[x,xiter,ste]=gn(x0,'funcal',vv,ee);

% calculate uncertainty from asymptotic standard error
n=length(a); % number of data points
par=length(x); % number of parameters
t=qt(0.975,n-par); % t-dis at alpha=0.05 [two-tail p=1-0.05/2=0.975]
u=ste*t; % +/- uncertainty
up=u./x*100; % percent uncertainty

```

```

% apply monte calro simulation to calculate uncertainty
% in calibration factors
n=100; % simulation steps
%[ur,ui]=calmc(n,alp,u,gam,frq);
if f==1.8e9
    aa=109.22e-3; b=aa/2;
elseif f==900e6
    aa=247.65e-3; b=aa/2;
end

pfr=reshape(pfw,pn,an)'; prv=reshape(prv,pn,an)';
epsri=[er 1.5 ei 0.4]; zz=[z 0.01];
ff=[f 0.01]; aaa=[aa 0.01];
ss=std_cal(pfr,prv,1.2,epsri,zz,ff,aaa,v1,v2,v3,n);

%yy=[];
%for i=1:n
% pnet=reshape((pfw+(2*rand-1)*pfw*1.2/100)- ...
%             (prv+(2*rand-1)*prv*1.2/100),pn,an)';
% vv=[mean(v1./pnet,2) mean(v2./pnet,2) mean(v3./pnet,2)];
% er=er+(2*rand-1)*er*1.2/100;
% ei=ei+(2*rand-1)*ei*0.4/100;
% z=z+(2*rand-1)*z*0.01/100;
% f=f+(2*rand-1)*f*0.01/100;
% aa=aa+(2*rand-1)*aa*0.01/100;
% et=mc_theory(er,ei,z,pnet,f,aa);
% ee=mean(et.^2./pnet,2);
% x0=[1e-6 1e-6 1e-6]'; % initial guess
% [xx,xiter,ste]=gn(x0,'funcal',vv,ee);

```

```

% yy=[yy;xx'];
%end
%yys=sort(yy);
%yym=mean(yy)';
%yyd=std(yy)';
%se=yyd/sqrt(n)*1.96./yym*100;

% output section

% calibratoion factors and uncertainties
fprintf('\n Calibration factors: \n');
fprintf('\n \t er=%2.2f and ei=%2.2f at f=%1.2e Hz \n',er,ei,f);
fprintf('\n \t k1=%2.2e \t u1=%1.2f %% \n',x(1),up(1));
fprintf('\t k2=%2.2e \t u2=%1.2f %% \n',x(2),up(2));
fprintf('\t k3=%2.2e \t u3=%1.2f %% \n',x(3),up(3));

% plot section

% interpolate between points
rdi=linspace(rd(1),rd(an),100)';
vvi=interp1(rd,vv,rdi,'spline');
eei=interp1(rd,ee,rdi,'spline');
eci=vvi*(1./x);
vc1=vvi(:,1)*(1/x(1));
vc2=vvi(:,2)*(1/x(2));
vc3=vvi(:,3)*(1/x(3));

% polar plots
polar(rdi,eei,'k');
hold on;

```

```

polar(rdi,eci,'x');
polar(rdi,vc1,'b');
polar(rdi,vc2,'r');
polar(rdi,vc3,'g');
legend('Theoretical','Calibrated','Dipole 1','Dipole 1','Dipole 3');
title(['k_1' '=' num2str(x(1)) ' ' ...
      'k_2' '=' num2str(x(2)) ' ' ...
      'k_3' '=' num2str(x(3))]);

```

### E.3 vcorrect.m

```

function [v1,v2,v3]=vcorrect(u1,u2,u3,vo1,vo2,vo3)

% correct voltage read from each channel in the e-field probe
% dipole sensors

% Labview removes the gain of the DAQ card in the reported voltage
% so the only "unaccounted" gain is the instrumentation amplifiers.
% Probe_voltage(n) = [Amplified_V(n) - Offset_V(n)] / Gain(n)
% where [Amplified_V(n) - Offset_V(n)] >= 0

% Compute actual probe voltages
v1=max((u1-vo1),0)/96.87;
v2=max((u2-vo2),0)/97.02;
v3=max((u3-vo3),0)/97.38;

```

### E.4 pcorrect.m

```

function [pfw,prv]=pcorrect(pf,pr,f)

```

```

% correct for coupler and cable losses

% load cable loss matrix
cbl=load('cable_a.txt');

% load coupler loss matrix
if find(f==900e6)
    cpl=load('coupler_hp.txt');
elseif find(f==1.8e9)
    cpl=load('coupler_narda.txt');
end

% get forward, reverse, insertion, and cable
% losses at each frequency
n=length(f);
for i=1:n
    j=find(f(i)==cpl(:,1));
    fr(i,1)=cpl(j,2); % coupler forward loss
    rv(i,1)=cpl(j,3); % coupler reverse loss
    in(i,1)=cpl(j,4); % coupler insertion loss
    j=find(f(i)==cbl(:,1));
    cb(i,1)=cbl(j,2); % cable loss
end

% compensate for losses
pfw=pf.*10.^(-fr/10).*10.^(in/10).*10.^(cb/10);
prv=pr.*10.^(-rv/10).*10.^(-cb/10);

```

## E.5 eprobe.m

```
function emag=eprobe(v1,v2,v3,f)

% calculate electric field magnitude from measured probe voltages
% and apply probe conversion factors

% Probe ET3DV6R SN:1422
% Tip to sensor center = 2.7mm

% Constants required for conversion
CF = 1.414;          % Crest Factor = (peak_power / average_power), unitless
                    % 1.414 for continuous wave
DCP = 100000;       % Diode Compression Point (100mV) in microvolts
Norm1 = 1.94;       % sensitivity of probe channel 1 in microvolts/(V/m)^2
Norm2 = 1.95;       % sensitivity of probe channel 2 in microvolts/(V/m)^2
Norm3 = 1.99;       % sensitivity of probe channel 3 in microvolts/(V/m)^2
if f==900e6
    ConvF = 6.01;    % enhancement factor in liquid (1 in air)
elseif f==1800e6
    ConvF = 5.17;    % enhancement factor in liquid (1 in air)
end

% convert voltages to micro-volts
u1=v1*1e6;
u2=v2*1e6;
u3=v3*1e6;

% compute actual probe voltages
```

```

e1=sqrt((u1+(CF*u1.^2)/DCP)/(Norm1*ConvF));
e2=sqrt((u2+(CF*u2.^2)/DCP)/(Norm2*ConvF));
e3=sqrt((u3+(CF*u3.^2)/DCP)/(Norm3*ConvF));

% compute total field magnitude
emag=sqrt(e1.^2+e2.^2+e3.^2);

```

## E.6 etheory.m

```

function emag=etheory(er,ei,z,p,f)

% calculate electric field magnitude from measured propagating power

% free space constants
eps0=8.8542e-12;    % free space permittivity
mu0=4*pi*1e-7;     % free space permeability

% waveguide constants
switch f
    case 900e6
        a=247.65e-3; b=a/2;
    case 1800e6
        a=109.22e-3; b=a/2;
end

% calculate parameters
w=2*pi*f;          % frequency in radians
s=w*eps0*ei;       % simulant conductivity
e=eps0*er;         % simulant permittivity

```

```

m=mu0;          % simulant permeability
beta=sqrt(w^2*m*(e-i*s/w)-(pi/a)^2);    % complex propadation constant

% calculate e-field magnitude
emag=sqrt(4*w*m*p/a/b/real(beta))*sin(pi/2).*exp(real(-i*beta)*z);
emag=emag/sqrt(2);

```

## E.7 factors.m

```

function k=factors(v1,v2,v3,e)

% calculate propotionality constants for e-field probe calibration at each
% orthogonal dipole
%
% inputs:   v1      first dipole voltage
%          v2      second dipole voltage
%          v3      third dipole voltage
%          e       total e-field magnitude squared
%
% output:   k       propotionality constant matrix
%
% solve the following linear system equation:
% [v1i v2i v3i][k]=[e]
%
% solution:
% [k]=[v1i v2i v3i]\[ei]

% get number of rows and columns
[r,c]=size(e); % v1, v2, and v3 must have the same dimensions

```

```

% solve for linear system
for i=1:c
    k(:,i)=[v1(:,i) v2(:,i) v3(:,i)]\[e(:,i)];
end

```

## E.8 gn.m

```

function [x,iter,u]=gn(x0,fun,par,dat)

% guess-newton iterative nonlinear least square method

% set parameters
iter=[];
k=0;
e1=1e-10;
kmax=1000;

% gauss-newton iterations
dxnorm=1.0;
x=x0;
while dxnorm>e1 & k<kmax
    k=k+1;
    [f,J]=feval(fun,x,par); f=f-dat;
    dx=-J\f; x=x+dx;
    %dx=-pinv(J)*f; x=x+dx;
    dxnorm=norm(dx);
    iter=[iter;k x' norm(f) norm(dx)];
end

```

```

% final sum-of-squares and variance
[f,J]=feval(fun,x,par); f=f-dat;
ss=f'*f;          % sum-of-squares
n=length(f);     % number of data points
p=length(x);     % number of parameters
var=ss/(n-p);    % variance

% variance-covariance matrix
vcm=(J'*J)^-1;

% parameters asymptotic standard error
u=sqrt(var*diag(vcm));

```

## E.9 funz.m

```

function [f,J]=funz(x,p)

% calculate fit function and it's jacobian

% function
A=x(1);
B=x(2);
f=A*exp(-p*B);

% jacobian
J1=exp(-p*B);
J2=-p.*A.*exp(-p*B);
J=[J1 J2];

```

## E.10 funesr.m

```
function f=funesr(esr,ear,alp,gam,frq)

% reflectance error bewtween measured and theoritical
% as a function of the simulant real permittivity
%
% inputs:
%     esr     simulant real permittivity
% ear acrylic real permittivity
%     alp     measured attenuation factor
%     gam     measured reflectance
%     frq     fequency of operation
%
% outputs:
%     f       reflection coefficient

% free space and waveguide constants
eps0=8.8542e-12;      % pemittivity
mu0=4*pi*1e-7;      % permeability
c=1/sqrt(eps0*mu0);  % speed of light

% radian frequency
w=2*pi*frq;

% waveguide cross section a x b
if frq==1.8e9
    a=109.22e-3; b=a/2;
elseif frq==900e6
    a=247.65e-3; b=a/2;
```

```

end

% calculate imaginary permittivity as a function of
% real permittivity
esi=alp*sqrt(w.^2.*mu0*eps0.*esr-(pi/a)^2)/w.^2/mu0/eps0;

% calculate reflectance
ref=reflect(esr,esi,ear,0,frq);

% error function
f=1/2*(ref-gam).^2;

```

## E.11 funesi.m

```

function f=funesi(esi,ear,alp,gam,frq)

% reflectance error bewtween measured and theoritical
% as a function of the simulant imaginary permittivity
%
% inputs:
%     esi     simulant imaginary permittivity
%     ear     acrylic real permittivity
%     alp     measured attenuation factor
%     gam     measured reflectance
%     frq     fequency of operation
%
% outputs:
%     f       reflection coefficient

```

```

% free space and waveguide constants
eps0=8.8542e-12;      % permittivity
mu0=4*pi*1e-7;      % permeability
c=1/sqrt(eps0*mu0);  % speed of light

% radian frequency
w=2*pi*frq;

% waveguide cross section a x b
if frq==1.8e9
    a=109.22e-3; b=a/2;
elseif frq==900e6
    a=247.65e-3; b=a/2;
end

% calculate real permittivity as a function of
% imaginary permittivity
esr=(w.^4*mu0^2*eps0^2*esi.^2+alp^2*(pi/a)^2)/alp^2/w.^2/mu0/eps0;

% calculate reflectance
ref=reflect(esr,esi,ear,0,frq);

% error function
f=1/2*(ref-gam).^2;

```

## E.12 reflect.m

```
function g=reflect(esr,esi,ear,eai,f)
```

```

% calculates the reflection coefficient at the air-acrylic interface
% inside the waveguide in the frequency domain
%
% inputs:
% f frequency
% esr simulant real permittivity
% esi simulant imaginary permittivity
% ear acrylic real permittivity
% eai acrylic imaginary permittivity
%
% outputs:
% g power reflectance at the air-acrylic interface

% free space constants
eps0=8.8542e-12; % pemittivity
mu0=4*pi*1e-7; % permeability
c=1/sqrt(eps0*mu0); % speed of light

% waveguide cross section a x b
if ~isempty(find(f==1.8e9))
    a=109.22e-3; b=a/2;
elseif ~isempty(find(f==900e6))
    a=247.65e-3; b=a/2;
end

w=2*pi*f; % radial frequency

% air, acrylic and simulant:
% permittivity eps0 epsa epss
% propagation constant beta0 betaa betas

```

```

% impedance          z0    za    zs
epsa=ear-j*eai;
epss=esr-j*esi;
beta0=sqrt((pi/a)^2-w.^2*mu0*eps0);
betaa=sqrt((pi/a)^2-w.^2*mu0*eps0.*epsa);
betas=sqrt((pi/a)^2-w.^2*mu0*eps0.*epss);
z0=j*w*mu0./beta0;
za=j*w*mu0./betaa;
zs=j*w*mu0./betas;

% two-way time delay travel in:
% acrylic      expa
% simulant     exps
da=22.465161e-3; % acrylic thickness in meters
ds=165.1e-3;    % simulant thickness in meters
expa=exp(-2*betaa*da);
exps=exp(-2*betas*ds);

% elementary reflection coefficients:
% interface 1: air-acrylic
% interface 2: acrylic-simulant
% interface 3: simulant-air
r1=(za-z0)/(za+z0);
r2=(zs-za)/(zs+za);
r3=(z0-zs)/(z0+zs);

% reflection coefficients for two layers
gama3=r3;
gama2=(r2+gama3.*exps)/(1+r2.*gama3.*exps);
gama1=(r1+gama2.*expa)/(1+r1.*gama2.*expa);

```

```
g=abs(gama1).^2;
```

## E.13 alpha.m

```
function g=alpha(esr,esi,f)

% calculates the attenuation factor of tissue-equivalent liquid
% inside the waveguide in the frequency domain
%
% inputs:
% f frequency
% esr simulant real permittivity
% esi simulant imaginary permittivity
%
% outputs:
% g attenuation factor of tissue-equivalent liquid

% free space constants
eps0=8.8542e-12;      % permittivity
mu0=4*pi*1e-7;      % permeability
c=1/sqrt(eps0*mu0);  % speed of light

% waveguide cross section a x b
if ~isempty(find(f==1.8e9))
    a=109.22e-3; b=a/2;
elseif ~isempty(find(f==900e6))
    a=247.65e-3; b=a/2;
end
```

```

% radian frequency
w=2*pi*f;

% attenuation factor
g=w.^2.*mu0*eps0.*esi./sqrt(w.^2.*mu0*eps0.*esr-(pi/a)^2);

```

## E.14 stdee.m

```

function ste=std_ee(ee,tt,gg,ff,aa,n)

```

```

f=ff(1); pf=ff(2);
t=tt(1); pt=tt(2);
g=gg(1); pg=gg(2);
e=ee(1); pe=ee(2);
a=aa(1); pa=aa(2);

opt=optimset('display','off');

yy=[];

for i=1:n
%yf=f+(2*rand-1)*f*pf/100;
yf=f+randn*f*pf/100/1.96;
%yt=t+(2*rand-1)*t*pt/100;
yt=t+randn*t*pt/100/1.96;
%yg=g+(2*rand-1)*g*pg/100;
yg=g+randn*g*pg/100/1.96;
%ye=e+(2*rand-1)*e*pe/100;

```

```

ye=e+randn*e*pe/100/1.96;
%ya=a+(2*rand-1)*a*pa/100;
ya=a+randn*a*pa/100/1.96;
er=fminbnd('funer',0,100,opt,ye,yt,yg,yf,ya);
ei=fminbnd('funei',0,100,opt,ye,yt,yg,yf,ya);
yy=[yy [er ei]'];
end

yy=yy';
yys=sort(yy);
yym=mean(yy);
yyd=std(yy);

low=ceil(2.5/100*n);
high=floor(97.5/100*n);
ste=(yys(high,:)-yys(low,:))./mean(yys(low:high,:))*100/2;

```

## E.15 changeee.m

```

n=1000;

per=linspace(0,5,10);

yyg=[];

for i=1:10
ssg=std_ee([ear 0],[d 0],[gam per(i)],[fq 0],[a 0],n);
yyg=[yyg;ssg];
end

```

```

figure; plot(per,yyg);
xlabel('\pm % change in power reflectance');
ylabel('\pm % change in permittivity');
legend('real','imaginary');

yyf=[];

for i=1:10
ssf=std_ee([ear 0],[d 0],[gam 0],[fq per(i)],[a 0],n);
yyf=[yyf;ssf];
end

figure; plot(per,yyf);
xlabel('\pm % change in frequency');
ylabel('\pm % change in permittivity');
legend('real','imaginary');

yya=[];

for i=1:10
ssa=std_ee([ear 0],[d 0],[gam 0],[fq 0],[a per(i)],n);
yya=[yya;ssa];
end

figure; plot(per,yya);
xlabel('\pm % change in waveguide dimension a');
ylabel('\pm % change in permittivity');
legend('real','imaginary');

```

```

yyr=[];

for i=1:10
ssr=std_ee([ear per(i)], [d 0], [gam 0], [fq 0], [a 0], n);
yyr=[yyr;ssr];
end

figure; plot(per,yyr);
xlabel('\pm % change in slab permittivity');
ylabel('\pm % change in permittivity');
legend('real', 'imaginary');

yyd=[];

for i=1:10
ssd=std_ee([ear 0], [d per(i)], [gam 0], [fq 0], [a 0], n);
yyd=[yyd;ssd];
end

figure; plot(per,yyd);
xlabel('\pm % change in attenuation factor');
ylabel('\pm % change in permittivity');
legend('real', 'imaginary');

```

## E.16 calunc.m

```

function cal_unc(f,z)

% calculate and plot uncertainties in calibration factors

```

```

eps0=8.8542e-12;
mu0=4*pi*1e-7;

w=2*pi*f;

if f==900e6
a=247.65e-3; b=a/2;
er=41.5; sig=0.97;
elseif f==1.8e9
a=109.22e-3; b=a/2;
er=40.0; sig=1.4;
end

ei=sig/w/eps0;
beta=sqrt(w^2*mu0*eps0*er-(pi/a)^2);

per=linspace(0,5,10)';

% imaginary permittivity
uei=-z*w*mu0*sig/beta;
yei=abs(uei)*per;
figure;
plot(per,yei);
ylabel('\pm % change in calibration factors');
xlabel('\pm % change in imaginary permittivity');

% real permittivity
uer=1/2*w^2*mu0*eps0*a^2*er* ...
(-w^2*mu0*eps0*a^2*er+pi^2+w*mu0*a^2*z*sig*beta)/(a*beta)^4;

```

```

yer=abs(uer)*per;
figure;
plot(per,yer);
ylabel('\pm % change in calibration factors');
xlabel('\pm % change in real permittivity');

% waveguide dimension
ua=w^2*mu0*eps0*a^2* ...
    (-w^2*mu0*eps0*a^2*er^2+pi^2*(er+ei*z*beta))/(a*beta)^4;
ya=abs(ua)*per;
figure;
plot(per,ya);
ylabel('\pm % change in calibration factors');
xlabel('\pm % change in waveguide dimension a');

% operating frequency
uf=-(pi^2*beta+z*w*mu0*sig*(a^2*w^2*mu0*eps0*er-2*pi^2))/a^2/beta^3;
yf=abs(uf)*per;
figure;
plot(per,yf);
ylabel('\pm % change in calibration factors');
xlabel('\pm % change in frequency');

```

## E.17 ref.m

```

function g=reflect(es,ea,fa,gam)

% calculates the reflection coefficient error using measured value
% at the air-acrylic interface inside the waveguide in the

```

```

% frequency domain
%
% inputs:
% f frequency
% esr simulant real permittivity
% esi simulant imaginary permittivity
% ear acrylic real permittivity
% eai acrylic imaginary permittivity
%
% outputs:
% g power reflectance at the air-acrylic interface

esr=es(1); esi=es(2);
ear=ea(1); eai=ea(2);
f=fa(1); a=fa(2);

% free space constants
eps0=8.8542e-12; % pemittivity
mu0=4*pi*1e-7; % permeability
c=1/sqrt(eps0*mu0); % speed of light

% waveguide cross section a x b
%if f==1.8e9
% a=109.22e-3; b=a/2;
%elseif f==900e6
% a=247.65e-3; b=a/2;
%end

w=2*pi*f; % radial frequency

```

```

% air, acrylic and simulant:
%   permittivity          eps0  epsa  epss
%   propagation constant  beta0  betaa  betas
%   impedance             z0    za    zs

epsa=ear-j*eai;
epss=esr-j*esi;
beta0=sqrt((pi/a)^2-w.^2*mu0*eps0);
betaa=sqrt((pi/a)^2-w.^2*mu0*eps0.*epsa);
betas=sqrt((pi/a)^2-w.^2*mu0*eps0.*epss);
z0=j*w*mu0./beta0;
za=j*w*mu0./betaa;
zs=j*w*mu0./betas;

% two-way time delay travel in:
%   acrylic      expa
%   simulant     exps

da=3e8/f/4/sqrt(3.44);    % acrylic thickness in meters
ds=165.1e-3;             % simulant thickness in meters

expa=exp(-2*betaa*da);
exps=exp(-2*betas*ds);

% elementary reflection coefficients:
%   interface 1: air-acrylic
%   interface 2: acrylic-simulant
%   interface 3: simulant-air

r1=(za-z0)/(za+z0);
r2=(zs-za)/(zs+za);
r3=(z0-zs)/(z0+zs);

% reflection coefficients for two layers

```

```

gama3=r3;
gama2=(r2+gama3.*exps)./(1+r2.*gama3.*exps);
gama1=(r1+gama2.*expa)./(1+r1.*gama2.*expa);

g=abs(gama1).^2;
g=1/2*(g-gam).^2;

```

## E.18 volsamfun.m

```

function vol_sam_fun(fp)

% Calculate 1g and 10g averages from volume scan files
%
% The Labview file is organized as follows:
% Column 1 2 3 4 5 6 7 8 9 10 11
%          X Y Z V1 V2 V3 Temp Voff1 Voff2 Voff3 Freq
%          12      13
%          Eps real Eps imaginary
%
% X, Y and Z in Steps
% Temp in Degrees Celcius
% V1, Voff1, V2, Voff2, V3, and Voff3 in Volts

% load file into variable and get size in rows and columns
file=load(fp);
[xyz,c]=size(file);

% get scan parameters
yz=length(find((file(:,1)-file(1,1))==0)); % yz points

```

```

xn=xyz/yz; % x points
zn=length(find((file(1:yz,2)-file(1,2))==0)); % z points
yn=xyz/xn/zn; % z points

% get x y z steps
x=file(1:yz:xyz,1);
y=file(1:zn:yz,2);
z=permute(reshape(file(:,3),zn,yn,xn),[3 2 1]);
xm=round((x-x(1))/98.2);
ym=round((y-y(1))/98.2);
for i=1:zn
zm(i,1)=round(mean(mean(z(:,:,1)-z(:,:,i))))/98.2+5.5;
end
zmm=abs(z-max(max(max(z))))/98.2;
fig=figure;
subplot(2,2,1);
mesh(ym,xm,flipud(zmm(:,:,1)));
xlabel('y-axis mm');
ylabel('x-axis mm');
zlabel('mm');
title('Bottom Surface Curvature');

% load measured values
d1=file(:,4); % raw dipole 1 voltage
d2=file(:,5); % raw dipole 2 voltage
d3=file(:,6); % raw dipole 3 voltage
temp=file(:,7); % ambient temprature
vo1=file(:,8); % dipole 1 offset voltage
vo2=file(:,9); % dipole 2 offset voltage
vo3=file(:,10); % dipole 3 offset voltage

```

```

f=file(1,11); % operating frequency
epsr=file(1,12); % real permittivity
epsi=file(1,13); % imaginary permittivity

% compute actual probe voltages and cooresponding e-field
[v1,v2,v3]=vcorrect(d1,d2,d3,vo1,vo2,vo3);
e1=sqrt(v1); e2=sqrt(v2); e3=sqrt(v3);
er=sqrt(e1.^2+e2.^2+e3.^2); % measured electric-field magnitude

% calculate e-probe magnitude
ep=eprobe(v1,v2,v3,f);

% calculate calibrated e-field magnitude
ec=calibrate(v1,v2,v3,f);

% calculate sar
sig=2*pi*f*8.8542e-12*epsi;
rho=1000;
sar=sig*ec.^2/rho;
sar=permute(reshape(sar,zn,yn,xn),[3 2 1]);
[mx,my,mz]=find(sar==max(max(max(sar))));
subplot(2,2,2);
mesh(ym,xm,sar(:,:,1));
xlabel('y-axis mm');
ylabel('x-axis mm');
zlabel('W/kg');
title(['Raw SAR at ' ...
       num2str(xm(mx)) ' ' num2str(ym(my)) ' ' num2str(zm(mz)) ' mm']);

% build array for 1g average

```

```

l=(1000)^(1/3); % 1g cube side length
ss=l/10; % side length partition
dx=ss; dy=ss; dz=ss; % incremental length x, y, and z
xi=[0:dx:max(xm)]';
yi=[0:dy:max(ym)]';
zi=[0:dz:max(zm)]';
int1g=interp3(ym,xm,zm,sar,yi',xi',zi,'spline');

% find max sar location and calculate 1g average
[xx,yy,zz]=find(int1g==max(max(max(int1g))));
sx=l/dx/2; sy=l/dy/2; sz=l/dz;

sar1g=0;
for i=sx+1:length(xi)-sx
for j=sy+1:length(yi)-sy
trap1g=int1g(i-sx:i+sx,j-sy:j+sy,zz:zz+sz);
tmp=trapz(trapz(trapz(trap1g)))*dx*dy*dz/1000;;
if tmp>sar1g
sar1g=tmp;
x1g=i; y1g=j;
end
end
end

fprintf('%s \t 1g =%1.5f',fp(1:6),sar1g);
fprintf('\t at x=%2.3f mm y=%2.3f mm z=%2.f mm \n', ...
        xi(x1g),yi(y1g),zi(zz));
subplot(2,2,3);
mesh(yi,xi,int1g(:,:,1));
xlabel('y-axis mm');
ylabel('x-axis mm');

```

```

xlabel('W/kg');
title(['1g= ' num2str(sar1g) ' W/kg ' ' at ' ...
      num2str(xi(x1g)) ' ' num2str(yi(y1g)) ' ' num2str(zi(zz)) ' mm']);

if xx<=sx | yy<=sy | (xx+sx)>length(xi) | (yy+sy)>length(yi)
fprintf('1g out of range \n');
end

% build array for 10g average
L=(10000)^(1/3); % 10g cube side length
SS=L/10; % side length partition
Dx=SS; Dy=SS; Dz=SS; % incremental length x, y, and z
X=[0:Dx:max(xm)]';
Y=[0:Dy:max(ym)]';
Z=[0:Dz:max(zm)]';
int10g=interp3(ym,xm,zm,sar,Y',X',Z,'spline');

% find max sar location and calculate 1g average
[XX,YY,ZZ]=find(int10g==max(max(max(int10g))));
Sx=L/Dx/2; Sy=L/Dy/2; Sz=L/Dz;

sar10g=0;
for i=Sx+1:length(X)-Sx
    for j=Sy+1:length(Y)-Sy
        trap10g=int10g(i-Sx:i+Sx,j-Sy:j+Sy,ZZ:ZZ+Sz);
        Tmp=trapz(trapz(trapz(trap10g)))*Dx*Dy*Dz/10000;
        if Tmp>sar10g
            sar10g=Tmp;
            x10g=i; y10g=j;
        end
    end
end

```

```

        end

end

fprintf('%s \t 10g=%1.5f',fp(1:6),sar10g);
fprintf('\t at x=%2.3f mm y=%2.3f mm z=%2.f mm \n', ...
        X(x10g),Y(y10g),Z(ZZ));
subplot(2,2,4);
mesh(Y,X,int10g(:,:,1));
xlabel('y-axis mm');
ylabel('x-axis mm');
zlabel('W/kg');
title(['10g= ' num2str(sar10g) ' W/kg ' ' at ' ...
        num2str(X(x10g)) ' ' num2str(Y(y10g)) ' ' num2str(Z(ZZ)) ' mm']);

if XX>Sx & YY>Sy & (XX+Sx)<=length(X) & (YY+Sy)<=length(Y)
fprintf('10g out of range \n');
end

```

## E.19 calstd.m

```

function uk=cal_std(z,f,p)

% calculate uncertainties in calibration factors
%
% input:
% z probe depth in mm
% f operating frequency Hz
% p percent change
% p(1) change in imaginary epsilon
% p(2) change in real epsilon

```

```

% p(3) change in waveguide dimension a
% p(4) change in frequency f
% output:
% uk uncertainty in calibration factors

eps0=8.8542e-12;
mu0=4*pi*1e-7;

w=2*pi*f;

if f==900e6
a=247.65e-3; b=a/2;
er=41.5; sig=0.97;
elseif f==1.8e9
a=109.22e-3; b=a/2;
er=40.0; sig=1.4;
end

%sig=w*eps0*ei;
ei=sig/w/eps0;
beta=sqrt(w^2*mu0*eps0*er-(pi/a)^2);

% imaginary permittivity
uei=-z*w*mu0*sig/beta;

% real permittivity
uer=1/2*w^2*mu0*eps0*a^2*er* ...
    (-w^2*mu0*eps0*a^2*er+pi^2+w*mu0*a^2*z*sig*beta)/(a*beta)^4;

% waveguide dimension

```

```

ua=w^2*mu0*eps0*a^2* ...
    (-w^2*mu0*eps0*a^2*er^2+pi^2*(er+ei*z*beta))/(a*beta)^4;

% operating frequency
uf=-(pi^2*beta+z*w*mu0*sig*(a^2*w^2*mu0*eps0*er-2*pi^2))/a^2/beta^3;

pei=p(1);
per=p(2);
pa=p(3);
pf=p(4);

uk=sqrt((uei*pei/100).^2+(uer*per/100).^2+(ua*pa/100).^2+(uf*pf/100).^2)*100;

```

## E.20 calunc.m

```

function cal_unc(f,z)

% calculate and plot uncertainties in calibration factors
%
% input:
% z probe depth in mm
% f operating frequency Hz
%
% output:
% plot uncertainties in:
% real epsilon
% imaginary epsilon
% waveguide dimension a
% operating frequency f

```

```

eps0=8.8542e-12;
mu0=4*pi*1e-7;

w=2*pi*f;

if f==900e6
a=247.65e-3; b=a/2;
er=41.5; sig=0.97;
elseif f==1.8e9
a=109.22e-3; b=a/2;
er=40.0; sig=1.4;
end

%sig=w*eps0*ei;
ei=sig/w/eps0;
beta=sqrt(w^2*mu0*eps0*er-(pi/a)^2);

per=linspace(0,5,10)';

% imaginary permittivity
uei=-z*w*mu0*sig/beta;
yei=abs(uei)*per;
figure;
plot(per,yei);
ylabel('\pm % change in calibration factors');
xlabel('\pm % change in imaginary permittivity \epsilon"');

% real permittivity
uer=1/2*w^2*mu0*eps0*a^2*er* ...

```

```

        (-w^2*mu0*eps0*a^2*er+pi^2+w*mu0*a^2*z*sig*beta)/(a*beta)^4;
yer=abs(uer)*per;
figure;
plot(per,yer);
ylabel('\pm % change in calibration factors');
xlabel('\pm % change in real permittivity \epsilon''');

% waveguide dimension
ua=w^2*mu0*eps0*a^2* ...
    (-w^2*mu0*eps0*a^2*er^2+pi^2*(er+ei*z*beta))/(a*beta)^4;
ya=abs(ua)*per;
figure;
plot(per,ya);
ylabel('\pm % change in calibration factors');
xlabel('\pm % change in waveguide dimension a');

% operating frequency
uf=-(pi^2*beta+z*w*mu0*sig*(a^2*w^2*mu0*eps0*er-2*pi^2))/a^2/beta^3;
yf=abs(uf)*per;
figure;
plot(per,yf);
ylabel('\pm % change in calibration factors');
xlabel('\pm % change in angular frequency w');

```

## E.21 calibrate.m

```

function emag=calibrate(v1,v2,v3,f)

% calculate calibrated e-filed magnitude

```

```

%
% inputs:  v1      first dipole voltage
%          v2      second dipole voltage
%          v3      third dipole volatge
%          f       operating frequency

% set calibration factors
switch f
case 900e6
k1=8.77e-6;
k2=8.49e-6;
k3=9.11e-6;
case 1.8e9
k1=9.20e-6;
k2=8.92e-6;
k3=9.61e-6;
end

% multiply by calibration factors to get e-mag squared
emag2=[v1 v2 v3]*[1/k1 1/k2 1/k3]';

% calculate emag and rearrange
emag=sqrt(emag2);

```

## E.22 calse.m

```

function [avg,eps,sig]=calse(e,ee,f)

% calculate average for three measurment of real and imaginary permitivity

```

```

% then calculate real permitivity and conductivity

% constants
eps0=8.8542e-12;    % free space permitivity
eps900=41.5;       % targer permitivity at 900mhz
sigma900=0.97;     % targer conductivity at 900mhz
eps1800=40;        % targer permitivity at 1800mhz
sigma1800=1.4;     % targer conductivity at 1800mhz

%calculate average permitivity
avg(1)=mean(e);
avg(2)=mean(ee);
eps(1)=avg(1);

%calculate conductivity
sigma=avg(2)*eps0*2*pi*f;
sig(1)=sigma;

% calculate error
switch f
    case 900e6
        eps(2)=(eps(1)-eps900)/eps900*100;
        sig(2)=(sig(1)-sigma900)/sigma900*100;
    case 1800e6
        eps(2)=(eps(1)-eps1800)/eps1800*100;
        sig(2)=(sig(1)-sigma1800)/sigma1800*100;
end

```

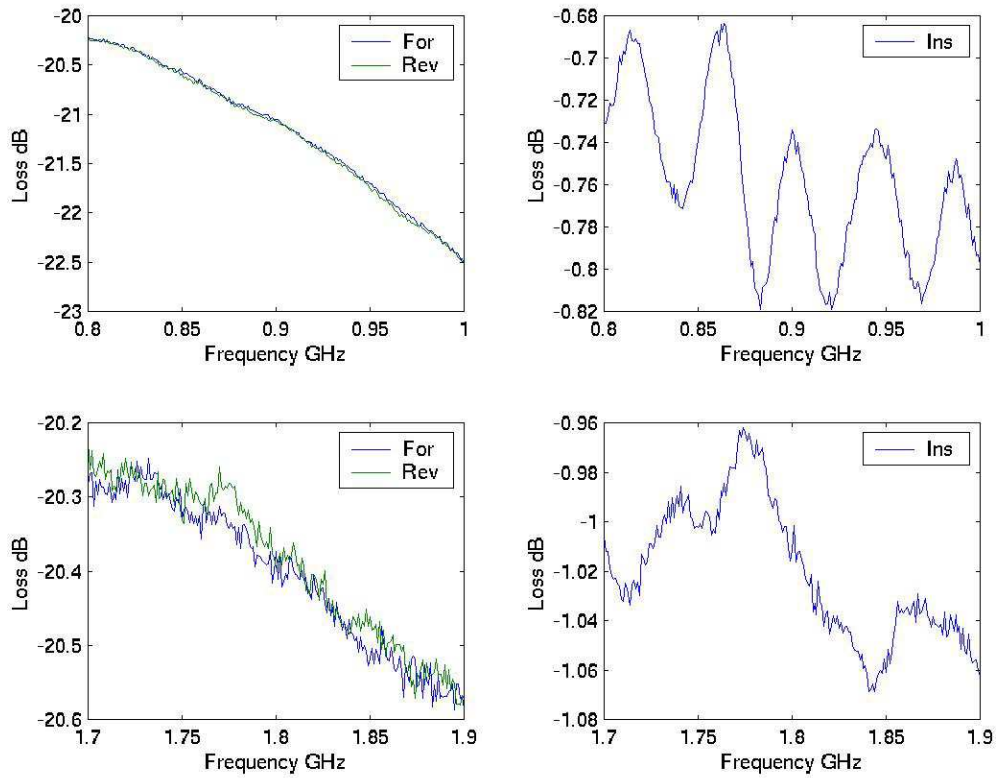


Figure E.1: Forward (For), Reverse (Rev), and Insertion (Ins) Coupler Loss versus Frequency

### E.23 Measured Coupler Loss

Figure E.1 shows the measured forward, reverse, and insertion loss.

### E.24 Measured Cable Loss

Figure E.2 shows the measured cable insertion loss.

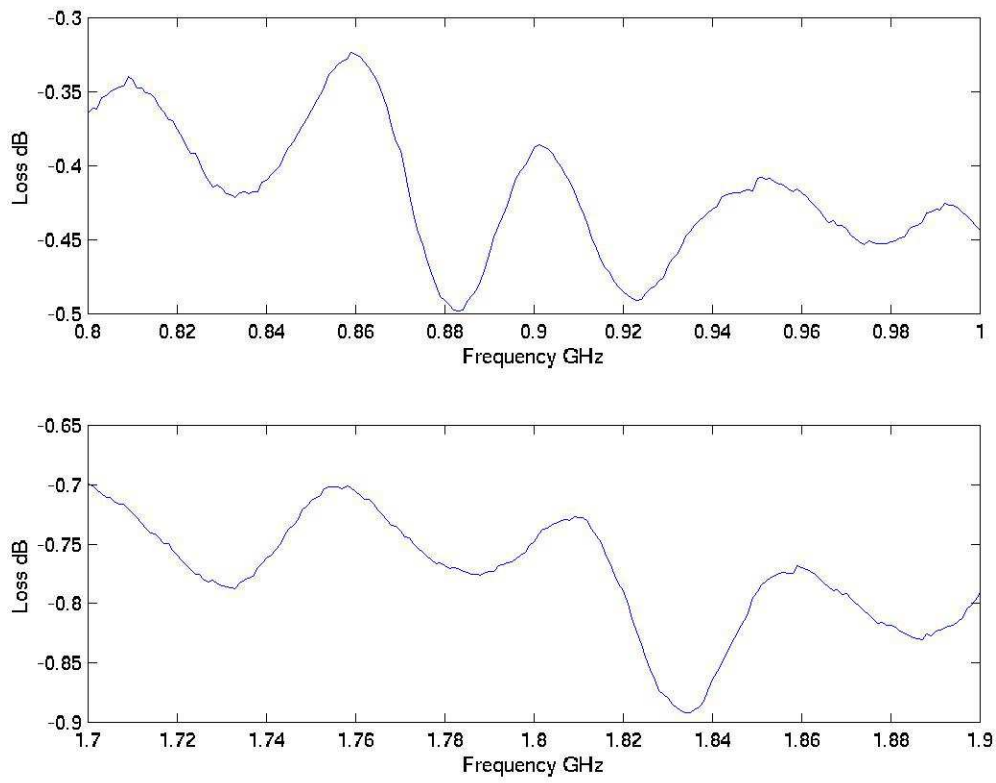


Figure E.2: Cable Insertion Loss versus Frequency

# Bibliography

- [1] C. C. Davis, “Measurement instructions and format for data,” *Phase II Wireless Phone SAR International Intercomparison*, 2005.
- [2] ICNIRP, *Guidelines for Limiting Exposure to Time-Varying Electric, Magnetic, and Electromagnetic Fields (up to 300 GHz)*, 1998.
- [3] O. P. Gandhi, H. Bassen, and T. Babij, *Biological effects and medical Applications of Electromagnetic energy*. Prentice-Hall, 1990. Chapter 7: Experimental Techniques and Instrumentation.
- [4] IEEE Standard C95.3, *Guidelines for Limiting Exposure to Time-Varying Electric, Magnetic, and Electromagnetic Fields (up to 300 GHz)*, 2002.
- [5] Q. Balzano, C. K. Chou, A. Faraone, and R. Y. Tay, “An efficient rf exposure system with precise whole body average sar determination for vivo animal studies at 900 mhz,” *IEEE Transactions On Microwave Theory and Techniques*, vol. 48, no. 11, pp. 2040–2049, November 2000.
- [6] H. I. Bassen, “Electric field probes for cellular phone dosimetry,” *IEEE Proceedings 19th international Conference*, pp. 2492–2495, November 1997.
- [7] H. I. Bassen and G. S. Smith, “Electric field probes-a review,” *IEEE Transactions on Antenna Propagation*, vol. 31, no. 5, pp. 710–718, September 1983.
- [8] IEEE Standard 1528, *IEEE Recommended Practice for Determining the Peak Spatial-Average Specific Absorption Rate (SAR) in the Human Head from Wireless Communications Devices - Measurement Techniques*, 2003.

- [9] K. Fukunaga, S. Watanabe, and Y. Yamanaka, "Dielectric properties of tissue-equivalent liquids and their effects on electromagnetic power absorption," *IEEE 2002 Annual Report Conference on Electrical Insulation and Dielectric Phenomena*, pp. 75–78, 2002.
- [10] A. Drossos, V. Santomaa, and N. Kuster, "The dependence of electromagnetic energy absorption upon human head tissue composition in the frequency range of 3003000 mhz," *IEEE Transactions on Microwave Theory and Techniques*, vol. 48, no. 11, pp. 1988–1995, November 2000.
- [11] V. Monebhurrun, C. Dale, J. C. Bolomey, and J. Wiart, "A numerical approach for the determination of the tissue equivalent liquid used during sar assessments," *IEEE Transactions on Magnetism*, vol. 38, no. 2, pp. 745–748, March 2002.
- [12] G. Lazzi, O. P. Gandhi, and D. Sullivan, "Fast and efficient fdtd simulations of personal wireless devices for sar compliance testing and antenna design," *IEEE Transactions on Antennas and Propagation*, vol. 22, pp. 1088–1091, July 2002.
- [13] Q. Yu, O. P. Gandhi, M. Aronsson, and D. Wu, "An automated sar measurement system for compliance testing of personal wireless devices," *IEEE Transactions on Electromagnetic Compatibility*, vol. 41, no. 3, pp. 234–245, August 1999.
- [14] O. P. Gandhi, H. Bassen, and T. Babij, *Biological effects and medical Applications of Electromagnetic energy*. Prentice-Hall, 1990. Chapter 6: Numerical Methods for Specific Absorption Rate Calculation.
- [15] IEEE Standard 1529, *Recommended Practice for Determining the Spatial-Peak Specific Absorption Rate (SAR) Associated with the Use of Wireless Handsets Computational Techniques*. Institute of Electrical and Electronics Engineers, New York, draft standard., New York, Draft Standard.
- [16] FCC, *Evaluating Compliance with FCC Guidelines for Human Exposure to Radiofrequency Electromagnetic Fields*, 1997.

- [17] K. S. Yee, "Numerical solution of initial boundary value problem involving maxwells equation in isotropic media," *IEEE Transactions on Antenna Propagation*, vol. 14, pp. 302–307, May 1966.
- [18] K. S. Kunz and R. J. Luebbers, *The Finite Difference Time Domain for Electromagnetics*. CRC Press, 1993.
- [19] B. M. Hakim, "FDTD analysis of microwave components," Master's thesis, The Pennsylvania State University, 2000.
- [20] K. Pokovic, "Robust setup for precise calibration of e-field probes in tissue simulating liquids at mobile communication frequencies," *ICECOM*, pp. 15–17, 1997.
- [21] K. Pokovic, T. Schmid, and N. Kuster, "Millimeter-resolution e-field probe for isotropic measurement in lossy media between 100 mhz and 20 ghz," *IEEE Transactions on Instrumentation and Measurement*, vol. 49, no. 4, pp. 873–878, August 2000.
- [22] H. W. Coleman and W. G. Steele, *Experimentation and Uncertainty Analysis for Engineers*. Wiley-Interscience, second edition ed., January 25, 1999.
- [23] M. Bittera, R. Martansky, and K. Kovac, "One way to provision of hf e-field sensor isotropy," *Measurement Science Review*, vol. 1, no. 1, pp. 73–76, November 2001.
- [24] K. Pokovic, T. Schmid, J. Frohlich, and N. Kuster, "Novel probes and evaluation procedures to assess field magnitude and polarization," *IEEE Transactions on Electromagnetic Compatibility*, vol. 42, no. 2, pp. 240–244, May 2000.
- [25] A. Stogryn, "Equations foe calculating the dielectric constant of saline water," *IEEE Transactions on Microwave Theory and Techniques*, pp. 733–736, 1978.
- [26] C. C. Davis, "Dielectric properties of saline solutions," *ISR Report number 2001-11*, 2001.
- [27] J. D. Jackson, *Classical Electrodynamics*. John Wiley and Sons, Inc., third edition ed., 1999.

- [28] D. M. Pozar, *Microwave Engineering*. John Wiley and Sons, Inc., second edition ed., 1998.
- [29] S. Ramo, J. R. Whinnery, and T. V. Duzer, *Fields and Waves in Communication Electronics*. John Wiley and Sons, Inc., third edition ed., 1994.